

Simulation Of Room Transfer Functions With Directivity Patterns On The Basis Of Modes

Master Thesis

Andrés
Ureta Staackmann

Assesor: Prof. Robert Höldrich, Dr. Alois Sontacchi
Supervisor: Dr. Franz Zotter

Graz, October 10, 2014



institut für elektronische musik und akustik



Abstract

The study presented here intends to provide ideas and theoretical principles required to simulate room transfer functions with directivities on the basis of modes, via the so-called *Room Modes Method* (RMM). The lossless Helmholtz equation in the Cartesian coordinate system is the starting point for the considerations made here. It provides the transfer function between source and receiver as the infinite sum of room modes and their individual resonant behavior. Simulation to infinity is only possible in theory and must therefore be band limited. It becomes possible to describe the point-to-point transmission by a limited number of room modes.

The well-known *Image Source Method* (ISM) is used as a reference in order to compare the performance achieved and accuracy of the RMM. Both methods deliver the perfect solution when summed over infinitely many room modes and image sources, respectively. A direct comparison between the two methods is for this very reason of great interest.

The main focus of this thesis lies in employing sources and receivers having arbitrary directivity patterns, which yields directional room transfer functions. This can be done by weighting the Green's function with the spherical harmonics for the ISM or by employing the multipole characteristics in the RMM. The first ones can be directly evaluated and applied, while the multipole characteristics imply directional derivatives on the series representation of the Green's function. Ultimately both variants are compared in the spherical harmonic domain, by conversion from multipole to spherical harmonic far-field directivity patterns.

General directivity patterns are created by a linear combination of multipoles or spherical harmonics. Finally, simulations of directional room transfer functions are carried out for both methods and are made available for a comparison and evaluation of their performance. The accuracy of both methods is likely to stand in direct relationship to their truncation in space or the modal domain, respectively. The influence of this truncation constitutes the main problem studied in this work.

Zusammenfassung

Diese Arbeit beschäftigt sich mit der Simulation von Raumübertragungsfunktionen unter Anwendung von Raummoden in Räumen mit schallharten und parallelen Wänden. Ausgangspunkt ist die verlustlose Helmholtz-Gleichung im kartesischen Koordinatensystem, welche die Raumübertragungsfunktion von Quellpunkt zu Empfangpunkt durch eine unendliche Summe frequenzabhängiger Raummoden liefert. Eine solche Berechnung ist nur theoretisch denkbar und muss in der Umsetzung bandbegrenzt werden. Mit einer begrenzten Anzahl von Raummoden ist es nun möglich die Punkt-zu-Punkt-Übertragung zu beschreiben.

Die gängige Spiegelquellen-Methode ist als Referenz eingesetzt worden. Sie stellt einen Referenzpunkt dar, um die erreichte Leistung und Genauigkeit der moden-basierten Simulationen mit Richtwirkung zu beurteilen. Beide Methoden liefern, wenn summiert über unendlich viele Raummoden bzw. Spiegelquellen, die perfekte Lösung. Ein direkter Vergleich ist aus diesem Grund von großem Interesse.

Der Schwerpunkt liegt bei der Anwendung von Richtcharakteristiken, welche Simulationen von Raumimpulsantworten mit Richtwirkung ermöglicht. Diese Winkelabhängigkeit kann für die Spiegelquellen-Methode durch eine Gewichtung der Green'schen Funktion mit Kugelflächenfunktionen, die nach Evaluierung direkt einsetzbar sind, realisiert werden.

Im Gegensatz dazu werden Multipole-Richtcharakteristiken bei der Raummoden-Methode eingesetzt. Dabei wird die Green'sche Funktion in ihrer Reihendarstellung örtlich abgeleitet. Letztendlich sind beide Varianten mit einer sphärischen harmonischen Analyse verglichen. Die Überführung von Multipol- in Kugelflächenfunktionen-Richtcharakteristiken wurde für die Fernfeld-Näherung dieser Funktionen durchgeführt.

Im Prinzip können Richtcharakteristiken durch eine Linearkombination von Multipolen oder Kugelflächenfunktionen beliebig gewählt werden. Schließlich werden Raumimpulsantworten mit Richtwirkung simuliert. Die Genauigkeit beider Methoden hängt von der Abschneidung, sowohl im Raum als auch im modalen Bereich, ab und ist gegenübergestellt. Der Einfluss dieser Abschneidung stellt die zu untersuchende Problematik dieser Arbeit dar.

Contents

1	Introduction	6
1.1	Topic	6
1.2	The Importance Of Directivity Patterns	9
1.2.1	Directivity Pattern Representations	10
1.2.2	Truncation Of The Infinite Sums	12
1.3	Structure	15
2	Sources Under Free-Field Conditions	16
2.1	Helmholtz Equation In \mathbb{R}^3	16
2.1.1	Homogeneous Solution	17
2.2	Green's Function Of The Free-Field	17
2.2.1	Green's function in 1-D	18
2.2.2	Free-Field Green's Function in 3-D	18
2.3	Describing Directivities	20
2.3.1	Multipoles	20
2.3.2	Angular Dependent Solutions To The 3-D Wave Equation In Spherical Coordinates	22
2.3.3	Matrix / Vector Notation Of The Spherical Harmonics And Multipoles	25
2.3.4	Conversion Between Spherical Harmonics And Multipoles	26
2.3.5	Conversion Matrix	26
3	Shoobox Shaped Room With Rigid Walls	30
3.1	The Room Modes Method	30
3.1.1	Homogeneous Solution	30
3.1.2	Non-Homogeneous Solution	31
3.1.3	Filters	36
3.2	Analogy Between The RMM And ISM	38
3.3	The Image Source Method	42

<i>Ureta Staackmann: Room Transfer Functions On The Basis Of Modes</i>	5
3.3.1 ISM In Its Time Domain Representation	46
3.4 Sparse Model Of A Room Response	47
3.4.1 Directivity Patterns For Source And Receiver	48
3.4.2 Directional Room Responses	49
3.5 Arbitrary Directivities	50
3.5.1 Spherical Harmonic Characteristics Employed For The ISM	50
3.5.2 Spherical Harmonics In The Far-Field	51
3.5.3 Multipole Characteristics For The RMM	52
3.5.4 Far-Field Normalization Of The Multipole Characteristics	54
3.5.5 Matrix Notation Of The RMM With Multipole Characteristics	57
4 Room Response Simulations With Directivities And Comparison	59
4.1 Absorbing Walls	59
4.1.1 Reflection Coefficient	59
4.1.2 Auralization Of Room Modifications	61
4.2 Room Impulse Responses And Room Transfer Functions	64
4.2.1 Simulations With The ISM	64
4.2.2 Simulations With The RMM	66
4.2.3 Direct Comparison Between The RMM And The ISM	69
4.3 Analysis Of The RIR In The SH-Domain	71
4.3.1 Energy Histogram	72
5 Resume And Outlook	78
Appendices	81
A Green's Function Of A Point Source In Free Field	81
B Jacobian Matrix	84
C Energy Histogram	85

1 Introduction

1.1 Topic

The analytical computation of room impulse responses (RIR) for omni-directional sources and receivers has been subject of research in numerous publications such as [ASV06, MBS⁺08, SSS11, TPKL13] and more generally in [Kut09]. These solutions are valid for simple geometrical shapes such as rectangular rooms with parallel walls. In extension of these works, the goal here is to study room transfer functions. In particular, the results of the *Room Modes Method* (RMM) for sources and receivers of arbitrary directivity are compared with those of the well-known and widely used *Image Source Method* (ISM). Both methods are realized by truncating their infinite sums across either the room modes or image sources.

A truncation in time will determine the number of mirrored sources taken into consideration and thus the accuracy of the computed room response computed with the ISM. For this method the original source is mirrored in space with respect to every coordinate simulating the wall reflections of the sound field in an enclosed space. The room responses computed with the ISM provide a good reference for the ones computed with the RMM. In this method the so-called room modes are used in order to compute the room transfer function. Here the band limitation occurs in the frequency domain in form of a cut-off frequency up to which the room modes are calculated. It is important to point out the fact that both methods deliver a perfect solution when summed to infinity for enclosed spaces with totally reflecting surfaces and for point sources and receivers. An expansion with directivities remains the focus of this work.

Room Responses Of Sources And Receivers Of Arbitrary Directivities

The result of applying directivity patterns is an enhancement of the 1-D RIR. The latter notion refers to a room response measured at the receiver position with an omni-directional microphone for input signals in the form of an impulse. The whole idea of computing the acoustical impulse response, as it happens in signal processing, aims at describing a room via its impulse response $h(t)$. The analogy lies within the fact that rooms are considered to be linear and time-invariant systems defined by their impulse responses.

Once the room impulse response is known, it can be used for convolution with any finite input signal $x(t)$ to obtain the corresponding system response. The next step is thus to expand the last idea for sources and receivers of arbitrary directivity. Directivities are exemplarily shown in Fig. 1 in their polar diagram form. As seen in Fig. 9, this representation can be expanded for the 3-D case by considering the zenith angle too. Consequently, two angular variables ϑ and φ are needed in order to describe the directivity pattern of sources and receivers in 3-D space.

The RIR $h(t)$ becomes a directional function $h(\boldsymbol{\theta}_R, t, \boldsymbol{\theta}_S)$ depending on spherical angles, where the subscript R and S of the angular vectors $\boldsymbol{\theta}$ refer to the receiver and source. The concept of *directional room impulse response* and not of room impulse response is from now on valid given the introduction of directional characteristics of the source as well as the receiver's sensitivity. This fact constitutes an important enhancement and is one of the primary topics to be studied within the frame of the work presented here. The compact notation of the angles used above is defined by the unit length vectors $\boldsymbol{\theta}^T = [\cos \varphi \sin \vartheta, \sin \varphi \sin \vartheta, \cos \vartheta]^T$ and reflects the relationship between the Cartesian and spherical coordinate systems.

A spatial window like the one illustrated in the left-hand side of Fig. 1 could be used for describing the source's radiation pattern. In this particular case the source would radiate sound in one direction mostly. Whether or not sound is radiated in a focused way depends amongst others on the source's geometry and signal's frequencies. Higher frequencies will not propagate uniformly in space as soon as the wavelength λ becomes smaller than the source's dimensions. The polar angle 0° in Fig. 1 represents the orientation of the source and main energy focus. Likewise, the sensitivity of the source can be determined with a polar function like the one depicted in the right-hand of Fig. 1.¹ A receiver with such a characteristic picks up sound from its orientation angle mostly, in this case from the polar angle 180° .

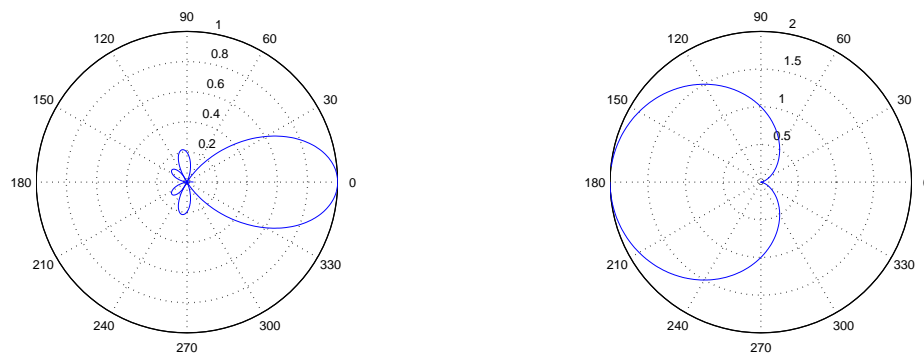


Figure 1: Typical directivities in polar coordinates.

The room responses computed in Section 4 do not include the frequency dependent radiation pattern of both sources and receivers as it happens in reality. This would have to consider the wavelength of the measuring signal, source's and receiver's dimensions as well as the resulting frequency dependent radiation pattern and sensitivity. This aspect

1. The directivity pattern of the cardioid is a conventional microphone characteristic. It is defined as $D(\varphi) = \frac{1}{1-\cos \varphi}$ in its polar representation.

would represent a major increase of the simulation's complexity and lies outside the focus of the work presented here. This one remains to study room response simulation with directivity on the basis of multipoles and spherical harmonics and not to reproduce the process of sound radiation and reception of real sources and receivers. The outcome can be understood to be the room response simulation between sources and receivers with a frequency-independent radiation pattern and sensitivity.

The computation and storage of room responses in the form of $h(\boldsymbol{\theta}_R, t, \boldsymbol{\theta}_S)$ offers not only flexibility for their superposition but provides also, as seen in Section 3.4.1, a good method for analysing the energy contributions of a source of arbitrary directivity at the receiver's position with arbitrary sensitivity. The orthonormality property of the spherical harmonic functions together with a sampling method for the sphere constitute a great advantage for this task. The sampling strategies employed are treated in Section 2.3.5, where the benefit of a spherical-harmonic-based description becomes evident.

The room response of a source and receiver of arbitrary directivities becomes possible by means of superposition of directional room responses with different radiation patterns and sensitivities. Zotter describes in [Zot14a] a compact form for the computation of room responses in this form. The exact notation and computation procedure is described in Section 3.5.3 as well as the conversion between multipole and spherical-harmonic based directivities.

Furthermore, the absorbing nature of wall materials is included in order to produce more realistic results. This can be done for the ISM by applying to each of the delimiting surfaces of the room. In this process each individual source contribution receives a weight depending on the relative position between the mirrored source and the receiver.

While it is relatively simple to consider absorption in the ISM by applying a reflection coefficient², the RMM is based on the assumption of massive and rigid walls.³ For a simple inclusion of absorption, the computed room transfer function is multiplied by an exponential attenuation in its time-domain representation (RIR). The main idea for simulating absorbing walls is taken from [PSJ13] and is treated in Section 4.1. Also, the reverberation time T_{60} can be influenced by applying different reflection coefficients the way it is shown in Section 4.1.2.

As mentioned before, the room response is to be computed in enclosed spaces with boundary conditions. These are determined by the geometry of the room itself, which will typically have a ratio of the so-called *shoebox shaped room* illustrated in Fig. 2. Such a room has typically these proportions $L_x > L_y > L_z$, where the subscript refers to the coordinate direction.

2. Real-valued coefficient used to describe the amplitude and phase of a reflected wave relative to an incident wave.

3. Rigid walls do not exist in reality, these would have to be infinitely heavy and stiff.

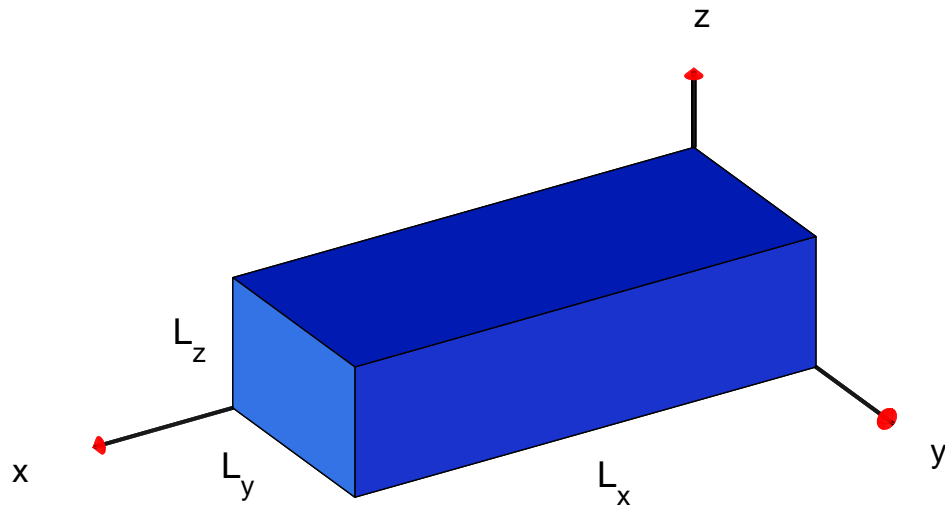


Figure 2: Shoebox shaped room with parallel walls.

1.2 The Importance Of Directivity Patterns

The truncated room transfer function in its natural form and using one of both methods, describes an omnidirectional sound source placed at \mathbf{r}_s in space being received by an omnidirectional receiver placed at \mathbf{r}_r . Here, \mathbf{r} is a vector that describes a discrete point $\mathbf{r}^T = [x, y, z]^T$ in 3-D space. Thus the room responses are valid for point sources and receivers only. This kind of acoustic bodies have a perfectly omnidirectional characteristic that corresponds to the acoustic monopole. An acoustic monopole in form of a source radiates sound in the same manner in all directions, meaning no angle is favoured with respect to another. Analogously, an acoustic monopole receiver picks up sound equally good independently of the wave's incident angle. However, natural sound sources will radiate sound differently depending very much on their geometry and size with respect to the wavelength λ and hence to the frequency being radiated given that $c = f \cdot \lambda$. The speed of sound c in air is $343,15 \frac{m}{s}$ under standard conditions.⁴

In the same way, natural acoustical receivers like a microphone or the human ear⁵ feature a direction-dependent pickup pattern. This means that the waves are picked up differently depending on their angle of incidence with respect to the receiver's orientation and

4. Standard conditions for temperature and heat capacity ratio in air are defined to be $T = 293,15K$ and $\kappa = 1,402$.

5. The directivity pattern of the human ear is described by the frequency dependent head-related transfer functions (HRTF). For a detailed description of the HRTF and the nature of the human ear refer to [Goe06] et al.

position. The wavelength is again an important factor that together with the receiver's size determine its frequency response characteristic. The latter are presented in form of polar diagrams like the one found to the right-hand side of Fig. 1 corresponding to the cardioid microphone. A detailed report concerning the directivity patterns of conventional microphones can be found in [Goe06] et al.

1.2.1 Directivity Pattern Representations

The objective of this work is to simulate room responses for sources and receivers of arbitrary directivities using both methods mentioned so far, i.e. the RMM and ISM, respectively. This angle dependency of the wave propagation in space can also be described by means of polynomials. The representation enables the creation of arbitrary directivity patterns by superposition of the polynomials themselves, offering a flexible configuration of the function's spatial distribution in space. Hence simulations where both sources and receivers feature an angle dependent radiation and reception of sound become possible.

With this in mind, an enhancement of the omni-directional radiation pattern becomes thinkable for the ISM by mirroring the chosen directivity together with the image source. The image sources are assumed to have an omni-directional characteristic and are described, when placed under free-field conditions, by the Green's function $G = \frac{e^{-ikr}}{4\pi r}$.⁶ Essentially this is done for every image source by evaluating the mirrored function describing the spatial distribution of G at their set of spherical angles. These are the zenith ϑ and azimuth φ angles as used in the spherical coordinate system in order to describe, together with the radius r , a point in 3-D space. For this purpose the spherical harmonic functions are chosen, amongst others because of the diversity they offer when superimposed but also because of their completeness property they feature given the fact they form an orthonormal set of functions. The expansion of a point source is done by multiplying the Green's function by an angle-dependent function as $G \cdot f_a(\boldsymbol{\theta})$. How directivities are incorporated through spherical harmonic functions is treated in Section 3.5.1, where their many advantages over other sets of functions become evident.

At this point the spherical harmonics up to the 3rd order are introduced in Fig. 3. The maximal order N_{SH} determines the number $(N_{SH} + 1)^2$ of spherical harmonics that exist up to that very order as well as the maximal achievable spatial resolution. The latter will be more precise the higher the order is. Two indices (n, m) determine the spherical harmonic function under consideration. The order n takes values between 0 and N_{SH} while the degree ranges for a given order from $-n \leq m \leq n$. Thus the directivity patterns are implemented by multiplying the Green's function by the spherical harmonics. The far-field approximation as implemented for the simulations in Section 4

6. These functions are named after the British mathematician George Green who first developed the concept in the 1830's. They are used to solve non-homogeneous differential equations subject to initial or boundary conditions.

read as:

$$\lim_{r \rightarrow \infty} G(r) = \frac{e^{-ikr}}{4\pi r} \cdot Y_n^m(\boldsymbol{\theta}). \quad (1)$$

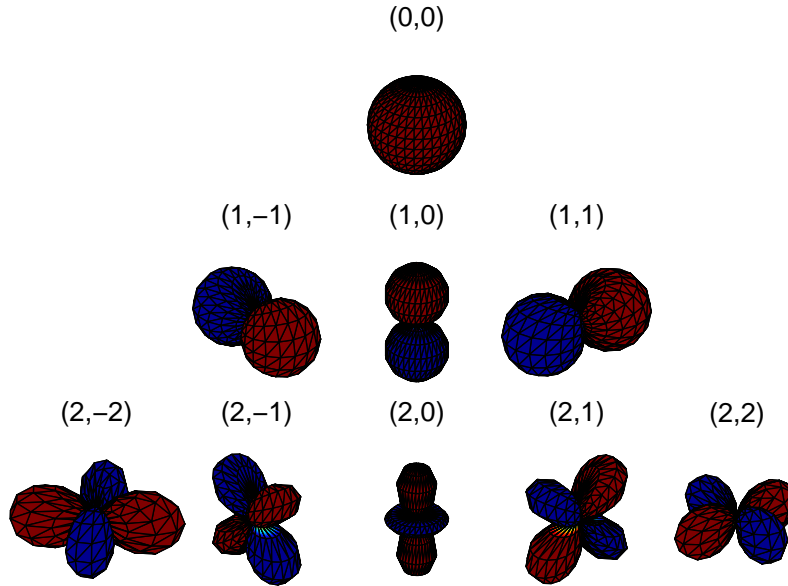


Figure 3: Spherical harmonics up to the 3rd order.

For the RMM on the other hand, a different method of generating directivity patterns is approached. This choice is supported given the solution's form to the problem as seen in Eq. 15. In this method the sound pressure is described via point sources in free-field and their corresponding Green's function, which stands in direct relationship to the sound field of a monopole source. This fact is of extreme importance because of the well-known relationship between the monopole and higher order multipoles. The idea is to derive higher order multipoles out of the monopole characteristic and apply them to the general solution, i.e. the point-to-point transmission between source and receiver, obtained with the RMM. How higher order multipoles are generated by multiple derivations of the monopole with respect to the coordinate axes is treated in Section 2.3.1. For now the raw formulation of directivity patterns by means of multipole characteristics is given by:

$$\lim_{r \rightarrow \infty} G(r) = \frac{e^{-ikr}}{4\pi r} \cdot \left(\frac{x}{r}\right)^l \left(\frac{y}{r}\right)^m \left(\frac{z}{r}\right)^n. \quad (2)$$

Here the derivatives are carried out by simple multiplications with respect to the derivative orders (l, m, n) . The precise procedure done for the far-field⁷ is shown in Section 3.5.3.

A disadvantage of multipole characteristics is the fact that these functions form an over-determined basis. This means that more functions are needed when describing a certain order of multipoles characteristics than, e.g. for spherical harmonics of that same order. This leans on the fact that $\frac{(N_{MP} + 1)(N_{MP} + 2)(N_{MP} + 3)}{6}$ multipoles exist up to the maximal multipole order N_{MP} . The consequence is already noticeable for 2nd and remarkable for 3rd order spherical harmonic functions and multipoles. For the latter four more functions are needed for fully describing the same order.

Nevertheless, arbitrary directivities can be generated by superposition of higher order multipoles. As seen in Fig. 4, the 1st order multipoles, also called dipoles, feature a directed beam of the function's distribution in one of the three Cartesian coordinates. The directivity pattern of the cardioid microphone, shown in the right-hand side of Fig. 1, can be generated in this way too. The acoustic beam will be oriented in one of the three coordinates depending on the dipole chosen for its superposition with the monopole characteristic. For an extensive derivation of the dipoles, quadrupoles and higher order multipole characteristics refer to [RTB98, Wil99].

The monopole, also known as the 0th moment or $(0, 0, 0)$ multipole, features no angle dependency as the spherical harmonic $(0, 0)$ does. As of multipoles of higher orders, they all hold an angle dependent distribution in space. The advantage of a spherical-harmonic-based description of directivity patterns next to a multipole-based one is treated in Section 2.3.4 and concerns the number of functions needed as well as the orthonormality property the spherical harmonic functions benefit from.

Adding directivity patterns to both sources and receivers lies in the emphasis of this work. Both methods are to be studied by means of computer simulations enabling a detailed comparison of their performance when truncated, the one in time while the other in frequency. The conversion of multipole- to spherical-harmonic-based directivity patterns and vice versa represents an important aspect offering a valuable enhancement of room transfer function simulations.

1.2.2 Truncation Of The Infinite Sums

The last subject open to consideration can be approached once the simulation of room responses with arbitrary directivities is possible. It consists in studying the band limita-

7. The far-field is most commonly defined as the distance $r_{far} \approx 2 \cdot \lambda_{far}$. It depends directly on the signals wavelength λ and thus from its frequency f .

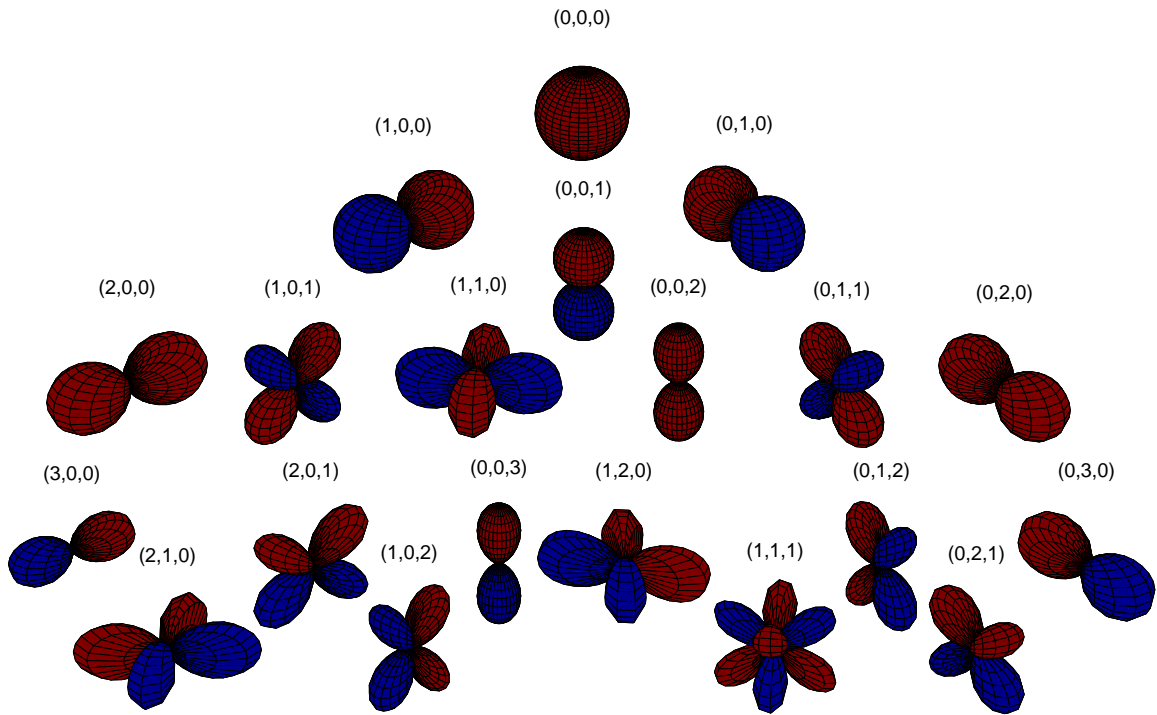


Figure 4: Multipoles up to the 3rd order. The indices (l, m, n) give the number of derivations in (x, y, z) .

tion applied to both methods, the one in time and the other in frequency, by means of computer simulations. The influence of a truncation in time on the simulation's accuracy in the frequency domain and vice versa is to be studied. A comparison of both methods when truncated should facilitate clear and comprehensive results concerning the number of room modes or image sources needed in order to achieve a certain simulation accurateness.

The relationship between the RMM and the ISM is known from early publications. In [AB78] the ISM is specified for the first time and most notably, its equivalence to the RMM is discussed. The conclusion drawn is the fact that both methods should deliver the perfect solution when summed to infinity. Are both methods equal when applying directivity patterns to sources and receivers? Also, the resolution aggravation introduced by the band limitation's choice is to be studied. How accurate are room responses computed with, e.g. 2000 or 3000 image sources? Is there a difference at all? Does it matter if the room response was computed using the first 1000 or 2000 room modes? These are all questions that will be answered within the frame of this work, where the emphasis lies in the results obtained for room responses of arbitrary directivities.

At present, the modes that emerge in a 2-D plane and their possible combinations for $l_{max} = 2$ are exemplarily illustrated in Fig. 5, where l_{max} is the maximal integer value the indices l_x and l_y can take and D is the dimensionality variable. As a result a total of

$(l_{max} + 1)^D$ mode combinations are possible. The fundamental frequency of the room is given by f_0 from which the ratio to higher order modes is given.

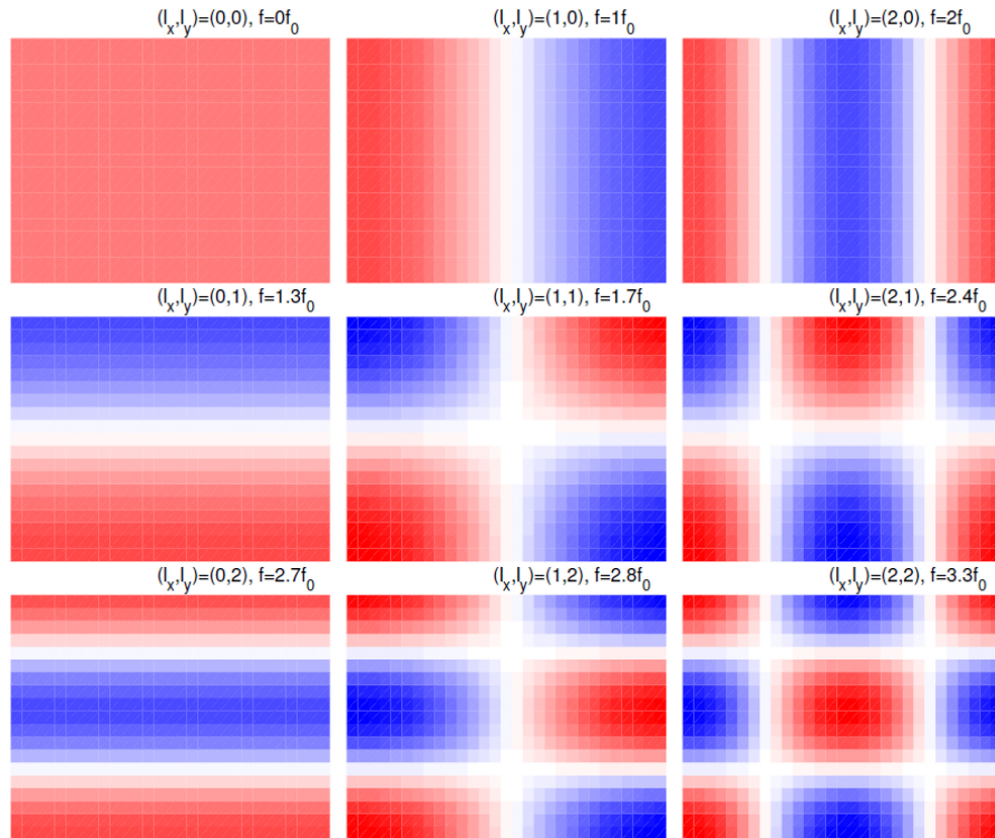


Figure 5: Modes for the rectangular room with totally reflecting walls in the 2-D case for $l_{max} = 2$ taken from [Zot14b].

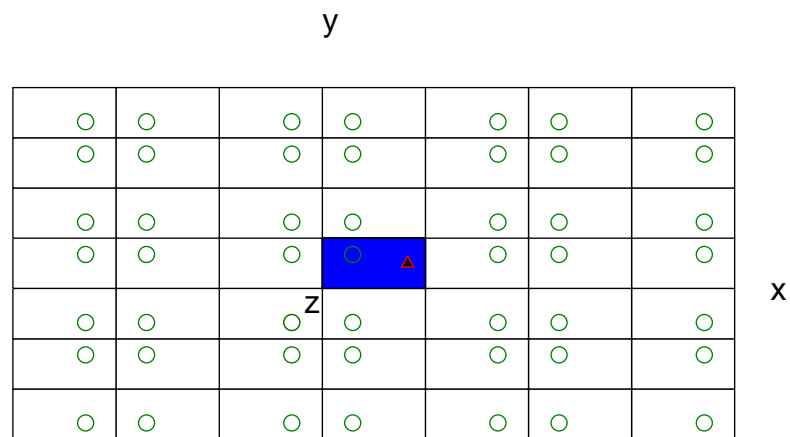


Figure 6: 2-D plane with the image sources (green circles) and receiver (red triangle).

The same is done for the ISM, where the number of image sources is limited in order to compute the room response in form of a finite sum of impulses. Fig. 6 illustrates how image sources are placed in the 2-D free-field around the room in blue. How the truncation looks for the ISM is discussed in Section 3.3.

1.3 Structure

This work is divided in sections. An introduction to both sets of functions used to describe directivity patterns and their mathematical principles is given in Section 2. The translation between them as well as the foundation for describing wave propagation is also treated in this section.

With this covered the simulation of room transfer functions in rectangular rooms with parallel walls and main problem is approached. How room responses are computed with both methods and most importantly how arbitrary directivities are implemented is explained in Section 3. Also, the far-field approximation of both multipole and spherical harmonic functions is shortly discussed.

What concerns the actual simulation of room responses and its realization by means of computer simulations is discussed in Section 4 as well as the theory needed in order to obtain results valid for absorptive wall materials by means of reflection coefficients and exponential attenuations. The obtained results and different evaluation methods are also presented in this section. Finally, the conclusions as well as possible future work are discussed and summarised in Section 5.

2 Sources Under Free-Field Conditions

2.1 Helmholtz Equation In \mathbb{R}^3

The starting point of the considerations made in this work is the Helmholtz equation in the Cartesian coordinate system. Any sound wave can be fully described by the sound pressure p and the particle displacement velocity v . Together they describe the instantaneous displacement the medium particles undergo through sound wave propagation. An extensive description of this phenomenon can be found in [Wil99, Kut09, Goe06] et al. The relationship between the time dependent sound pressure and local velocity is given in Eq. 3. It states that an increase of sound pressure equals a decrease of all three local velocities

$$\dot{p} = -K \left[\frac{\partial}{\partial x} v_x + \frac{\partial}{\partial y} v_y + \frac{\partial}{\partial z} v_z \right] = -K \nabla \mathbf{v}, \quad (3)$$

with the *Nabla* operator defined in the 3-D Cartesian coordinate system as $\nabla = (\frac{\partial}{\partial x}, \frac{\partial}{\partial y}, \frac{\partial}{\partial z})$. The particle displacement in a differential volume holds three independent directional components and is written in a mathematical way via the Euler equation

$$\nabla p = -\rho \cdot \dot{\mathbf{v}}, \quad (4)$$

where $\dot{\mathbf{v}}$ stands for the derivative of the particle velocity with respect to time and is defined as $\dot{\mathbf{v}} = \frac{\partial \mathbf{v}}{\partial t}$. Inserting Eq. 3 in Eq. 4 yields the Helmholtz equation in its time-independent form as follows:

$$(\Delta + k^2) p = 0. \quad (5)$$

Eq. 5 describes the law that governs wave propagation in any medium, where the wavenumber⁸ is defined as $k = \frac{\omega}{c}$. It stands in direct relationship to the propagation speed c and the angular frequency $\omega = 2\pi f$. The *Laplacian* operator Δ is defined as

$$\begin{aligned} \Delta &= \nabla^T \cdot \nabla \\ &= \frac{\partial^2}{\partial x^2} + \frac{\partial^2}{\partial y^2} + \frac{\partial^2}{\partial z^2}. \end{aligned}$$

8. This quantity relates the propagation speed of a wave to its oscillation frequency and has a unit of m^{-1} . It gives the number of oscillations that fit in the unity length of 2π .

2.1.1 Homogeneous Solution

The homogeneous solution of the Helmholtz equation for plane waves can be solved through an exponential approach of the form

$$\begin{aligned} p_h(\mathbf{r}) &= e^{-ik_x x} \cdot e^{-ik_y y} \cdot e^{-ik_z z} \\ &= p(x) \cdot p(y) \cdot p(z). \end{aligned} \quad (6)$$

The solution as presented in Eq. 6 is separated into terms that depend each on only one of the space variables. Together they form the solution $p_h(\mathbf{r})$ to the homogeneous problem given by

$$\left(\frac{\partial^2}{\partial x^2} + \frac{\partial^2}{\partial y^2} + \frac{\partial^2}{\partial z^2} + k^2 \right) p_h = 0. \quad (7)$$

Inserting the product from Eq. 6 in Eq. 7 delivers the characteristic equation

$$k^2 = k_x^2 + k_y^2 + k_z^2, \quad (8)$$

where (k_x, k_y, k_z) denote the wave numbers in each of the coordinate directions and are summarized within the *wave vector* $\mathbf{k}^T = [k_x, k_y, k_z]^T$. All homogeneous solutions, for which Eq. 8 is fulfilled, are written in a compact form as

$$p_h(\mathbf{r}) = e^{-i\mathbf{k}^T \mathbf{r}} \cdot \delta(\mathbf{k}^T \mathbf{k} - k^2). \quad (9)$$

The solutions for both the 1-D and 2-D problems can be found, amongst others in [Wil99, KFCS00], where additional information concerning the $\mathbf{k} - space$ ⁹ is also available.

2.2 Green's Function Of The Free-Field

No real source generates the field described by Eq. 5, which is why a different approach is necessary in order to describe other kind of fields. The RIR is obtained in the majority of cases by measuring at the receiver position the field generated by a source radiating an impulse. It is precisely this kind of fields that constitute the foundation for the ISM, where all mirrored sources radiate the same impulse at the same time at their corresponding positions. As shown in Section 3.3, the RIR for point sources and receivers can be computed by superposition of L impulses. These are radiated by L identical sources placed free field. The analogy between the ISM and the RMM is treated in Section 3.2.

9. 2-D or 3-D *Fourier* transform of any function $a(\mathbf{k})$ defined in space.

2.2.1 Green's function in 1-D

An inhomogeneity is introduced under free-field conditions in form of an impulse at a certain time in space. This is described in a mathematical way by equalising the homogeneous wave equation to a non-zero term. The latter describes the inhomogeneity itself, where G stands for the Green's function and is responsible for triggering the elementary non-homogeneous problem given by Eq. 11. The δ distributions represent an impulse being radiated at a time t and place x in space.¹⁰

The next considerations are done for the 1-D problem in favour of a simple notation. In general, the Green's function $G(x, s)$ of a linear differential operator $L = L(x, t)$ acting on distributions over a subset of the Euclidean space \mathbb{R}^n at a point x in space, is any solution of

$$L G(x, t) = \delta(x)\delta(t), \quad (10)$$

where G is the fundamental solution associated to L . The linear differential operator is defined for the 1-D wave equation as $L = \frac{1}{c^2} \frac{\partial^2}{\partial t^2} - \Delta$ and when applied to Eq. 10 it yields

$$\begin{aligned} \left[\frac{1}{c^2} \frac{\partial^2}{\partial t^2} - \Delta \right] G(x, t) &= \delta(x)\delta(t) \\ \frac{1}{c^2} \frac{\partial^2 G(x, t)}{\partial t^2} - \frac{\partial^2 G(x, t)}{\partial x^2} &= \delta(x)\delta(t). \end{aligned} \quad (11)$$

The non-homogeneous wave equation is a differential equation of the form

$$L u(x, t) = f(x, t). \quad (12)$$

More general information concerning the solution of second-order time-dependent partial differential equations and boundary value problems can be found in [WW96, AW05, MF53, Heu13] et al. For a detailed study concerning the Green's function of the wave equation refer to [Som92].

2.2.2 Free-Field Green's Function in 3-D

The non-homogeneous problem in free-field can be solved by finding the Green's function $G_{3D}(r)$ of Eq. 13. The Green's function in its time-independent form for a point source

10. The *Dirac* delta is a generalized function or rather distribution that equals zero everywhere except at zero on the real number line. It is defined as $\delta(t) = \begin{cases} 1 & \text{if } t = 0, \\ 0 & \text{else.} \end{cases}$

place at $r = \sqrt{x^2 + y^2 + z^2}$ is found by solving the following equation:

$$\begin{aligned} (\Delta + k^2) G_{3D}(r) &= -\delta_{3D}(r) \\ \left[\frac{1}{r^2} \frac{\partial}{\partial r} \left(r^2 \frac{\partial}{\partial r} \right) + k^2 \right] G_{3D}(r) &= -\delta_{3D}(r), \end{aligned} \quad (13)$$

where the linear differential operator L is given by $\Delta + k^2$. The Laplacian is obtained in the general manner as $\Delta = \frac{1}{r^{D-1}} \frac{\partial}{\partial r} \left(r^{D-1} \frac{\partial}{\partial r} \right)$. A detailed derivation of the last result can be found in [Zot14b]. The following approach: $G = \alpha \frac{e^{\gamma r}}{r}$ yields for the 3-D case:

$$\begin{aligned} \frac{1}{r^2} \frac{\partial}{\partial r} \left(r^2 \frac{\partial}{\partial r} \right) G_{3D}(r) &= \frac{1}{r^2} \frac{\partial}{\partial r} \left[r^2 \left(\gamma - \frac{1}{r} \right) G_{3D}(r) \right] \\ &= \frac{1}{r^2} \frac{\partial}{\partial r} \left[(r^2 \gamma - r) G_{3D}(r) \right] \\ &= \left(\frac{2\gamma}{r} - \frac{1}{r^2} \right) G_{3D}(r) + \left(\gamma - \frac{1}{r} \right)^2 G_{3D}(r) \\ &= \left(\frac{2\gamma}{r} - \frac{1}{r^2} + \gamma^2 - \frac{2\gamma}{r} + \frac{1}{r^2} \right) G_{3D}(r) \end{aligned}$$

and thus for the non-homogeneous problem

$$(\gamma^2 + k^2) G_{3D}(r) = -\delta_{3D}(r). \quad (14)$$

γ is found with the last equation, which must be valid for $r > 0$ as well as for $r \rightarrow 0$. If $r > 0$ then $\delta_{3D}(r > 0) = 0$ and therefore $\gamma \pm ik$. By using the divergence theorem¹¹ one arrives to the well-known solution for the Green's function of a point source under free-field conditions:

$$G_{3D}(kr) = \frac{e^{-ikr}}{4\pi r}. \quad (15)$$

More to the derivation of the Green's function for a point source under free-field conditions can be found in [Zot14b] et al. For now Eq. 15 constitutes the correlation between multipoles, concretely the multipole (0,0,0) or monopole and the Green's function for point sources as used in Section 3.1.2 with the RMM.

¹¹ Integral used to compute the strength of a source in vector-based fields as: $Q_s = \oint_{\partial V} \mathbf{a}(\mathbf{r})^T d\mathbf{S}(\mathbf{r}) = \int_V \delta^T \mathbf{a}(\mathbf{r}) dV(\mathbf{r})$.

2.3 Describing Directivities

2.3.1 Multipoles

It is precisely the last result from Section 2.2.2 which constitutes the direct relationship between the Green's function, i.e. the solution to the non-homogeneous problem, and the radiation pattern of an acoustical multipoles used to describe room transfer functions for sources and receivers of arbitrary directivity with the RMM.

Multipoles are basically constructed from distributions of point sources infinitesimally close to each other. These have equal amplitudes but opposite phases resulting, as visible in Fig. 4, in positive and negative interferences. The simplest multipole or monopole radiates sound with an omni-directional characteristic, meaning there is no angular dependency of the sound pressure in space, see Eq. 14.

Many publications [RTB98, Wil99] et al. have studied the relationship between higher order multipoles and the monopole. The latter is equivalent to $G_{3D}(kr)$. Higher order multipoles are obtained by deriving the Green's function with respect to the coordinate system. A multipole $\tilde{M}_{lmn}(kr)$ of the order $l + m + n$ is given by:

$$\tilde{M}_{lmn}(kr) = \frac{\partial^l}{\partial x^l} \frac{\partial^m}{\partial y^m} \frac{\partial^n}{\partial z^n} G_{3D}(kr).$$

In addition, a linear combination of these derivatives can be used to represent directivity patterns for both sources and receivers. Some of the theory concerning multipoles is treated extensively in [Wil99] whereas the proposed method for creating multipoles of higher order via derivatives has been studied recently in [PDV13]. Pollow used the *Boundary Element Method* (BEM) in order to compare the room responses obtained by means of the proposed analytical calculation. The results match each other and show potential to complement the current research of RIR measurement of source and receiver of arbitrary directivity. However, Pollow noticed some unwanted frequency-response behaviour of the RMM that deserves more attention in later sections.

The free-field sound radiation of a 2-D monopole and dipole are exemplarily illustrated in Fig. 7. Both sources were placed at $\mathbf{r}'^T = [x, y]^T = [3, 2.5]^T$ in a 2-D plane of 9m x 5m. The dipole sound field arises via a derivation of Green's function with respect to the y-axis and is therefore oriented in the same direction. Eq. 16 describes the dipole's sound field, which differs to the monopole's sound field by a multiplication of the dipole distance d ¹² and by replacing $G_{3D}(kr)$ by its derivative. The angle dependency of the dipole's field is evident, as most of the source's energy is directed in the y-coordinate

12. Distance between two point sources of opposite phase that form the dipole. It is assumed to be vanishingly small.

while almost no wave propagation takes place in the x direction. A gray scale was used here in order to display the source's energy, white represents a high energy value while black is the opposite.

$$\tilde{M}_{010}(kr) = \frac{1}{-ik} \frac{\partial}{\partial y} G_{3D}(kr) \quad (16)$$

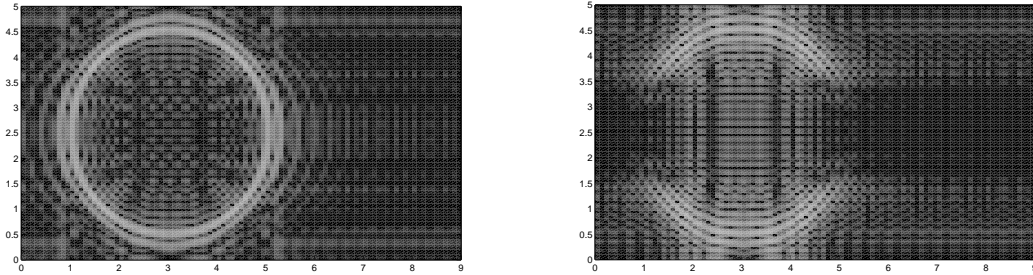


Figure 7: Sound field of a monopole (left) and of a dipole (right) in the 2-D case.

Creating directivity patterns in this manner has both advantages and disadvantages. The advantages are the straightforward relationship between the multipoles and the derivatives of $G_{3D}(kr)$. On the other hand, the computational complexity will increase drastically as soon as multipoles of higher orders are computed. This leans on the fact that a multipole of the N^{th} order requires $N = l + m + n$ derivatives of the monopole. Thereby is l the number of derivatives of the Green's function with respect to the x -coordinate, m with respect to the y - and n with respect to z -, respectively. Consequently, $\frac{(N_{MP} + 1)(N_{MP} + 2)(N_{MP} + 3)}{6} \propto N_{MP}^3$ derivatives are necessary in order to describe all existing multipoles up to the N_{MP}^{th} order.¹³

How room impulse responses are computed with the RMM is treated in Section 3.1 while their expansion into room responses of arbitrary directivities on the basis of multipoles is presented in Section 3.5.3. There the advantage offered by the direct relationship of higher order multipoles and the Green's function used for the RMM is evident. The latter is described by trigonometrical functions whose derivatives are straightforward to compute. The solution in this form enables an easy computation of higher order multipole characteristics that can be converted into their spherical harmonic equivalent and subsequently be used for the design of arbitrary directivities. The conversion between spherical harmonics and multipole characteristics is treated in Section 2.3.4.

13. This result follows from applying the constant and linear Gaussian summation formulas to the number $M = \sum_{l=0}^M \sum_{m=0}^{M-l} \sum_{n=0}^{M-l-m} 1$ of derivatives needed.

2.3.2 Angular Dependent Solutions To The 3-D Wave Equation In Spherical Coordinates

The spherical harmonic functions are a set of orthonormal functions on the two-dimensional sphere \mathbb{S}^2 , which form a complete and orthonormal base of the Hilbert space $L^2(S^2)$.¹⁴ These angular-dependent functions are defined in 3-D space by two angles, a zenith ϑ and an azimuth φ angle. The spherical coordinate system is favoured given the nature of the variables used. Together with the radius r it becomes possible to define positions in 3-D space as illustrated in Fig. 8. In acoustics the spherical harmonics are the angular dependent part of the solution of the wave equation in the spherical coordinate system and are defined as

$$Y_n^m(\vartheta, \varphi) = \sqrt{\frac{(2n+1)(n-m)!}{4\pi(n+m)!}} P_n^m(\cos \vartheta) e^{im\varphi}. \quad (17)$$

$P_n^m(x)$ represents the associated *Legendre* polynomials of the 1st kind. These polynomials constitute the solution to the Legendre differential equation:

$$(1-x^2)y'' - 2xy' + n(n+1)y = 0. \quad (18)$$

The solution will depend on the order n and degree m and is given by

$$P_n^m(x) = (-1)^m (1-x^2)^{\frac{m}{2}} \frac{d^m}{dx^m} P_n(x), \quad (19)$$

where $P_n(x) = P_n^0(x)$. These polynomials of degree n are used to describe fields that feature no variation in the azimuthal direction given that $m = 0$. They can be written with Rodrigues' Formula as follows:

$$P_n(x) = \frac{1}{2^n n!} \frac{d^n}{dx^n} (x^2 - 1)^n.$$

As seen to the left of Fig. 3, these functions are defined for negative values of m too. Eq. 19 is valid for positive values of n and m only, which is why another definition is necessary once m takes negative values:

$$P_n^{-m}(x) = (-1)^m \frac{(n-m)!}{(n+m)!} P_n^m(x). \quad (20)$$

¹⁴ A Hilbert space is an abstract vector space possessing the structure of an inner product that allows length and angle to be measured.

The complete solution to the 3-D wave equation in the spherical coordinate system including a deeper analysis of the solution to the Legendre differential equation can be found in [Wil99] et al. For now the mathematical principles concerning the spherical harmonic functions have been presented and can be used, as done in Section 3.5.1, for providing sources and receivers with directivities based on spherical harmonic functions.

The relationship between the Cartesian and spherical coordinate systems is given by $\mathbf{r}^T = [x, y, z]^T = [r \cos \varphi \sin \vartheta, r \sin \varphi \sin \vartheta, r \cos \vartheta]^T$. Analogously the spherical coordinates are computed as follows: $[r, \vartheta, \varphi] = \left[\sqrt{x^2 + y^2 + z^2}, \arccos\left(\frac{z}{r}\right), \arctan\left(\frac{x}{y}\right) \right]$ and are defined in $r \in [0, \infty]$, $\vartheta \in [0, \pi]$ and $\varphi \in [0, 2\pi]$.

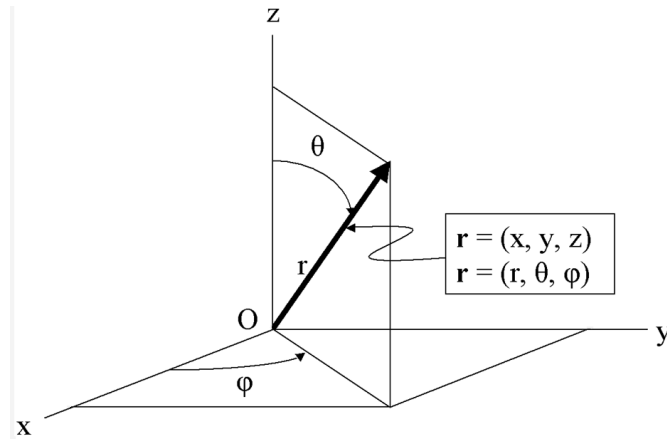


Figure 8: Spherical coordinate system.

Orthonormality And Completeness Properties: As already mentioned before, the spherical harmonics are an orthonormal set of functions. This means that the inner product of any spherical harmonics must equal to one, i.e. $\langle Y_n^m(\vartheta, \varphi), Y_{n'}^{m'}(\vartheta, \varphi)^* \rangle = 1$. The inner product can be written with the continuous support of both angles ϑ and φ as:

$$\int_0^{2\pi} d\varphi \int_0^\pi Y_n^m(\vartheta, \varphi) Y_{n'}^{m'}(\vartheta, \varphi)^* \sin \vartheta d\vartheta = \delta_{n,n'} \delta_{m,m'}. \quad (21)$$

Applying the completeness relation to the spherical harmonic functions yields the important relation

$$\sum_{n=0}^{\infty} \sum_{m=-n}^n Y_n^m(\vartheta, \varphi) Y_n^m(\vartheta', \varphi')^* = \delta(\varphi - \varphi') \delta(\cos \vartheta - \cos \vartheta'). \quad (22)$$

The latter manifests itself in any complete set of orthonormal functions. As a result any arbitrary function on a sphere $a(\vartheta, \varphi)$ can be decomposed as follows:

$$a(\vartheta, \varphi) = \sum_{n=0}^{\infty} \sum_{m=-n}^n A_{nm} Y_n^m(\vartheta, \varphi), \quad (23)$$

where A_{nm} is the so-called spherical wave spectrum consisting of complex constants. It can be found thanks to the orthonormality completeness property from Eq. 21 and Eq. 22 as:

$$A_{nm} = \int d\Omega Y_n^m(\vartheta, \varphi)^* a(\vartheta, \varphi). \quad (24)$$

Thereby are $Y_n^m(\vartheta, \varphi)^*$ the complex conjugated spherical harmonic coefficients of $Y_n^m(\vartheta, \varphi)$ and Ω is the solid angle defined as $\int d\Omega = \int_0^{2\pi} d\varphi \int_0^\pi \sin \vartheta d\vartheta$.

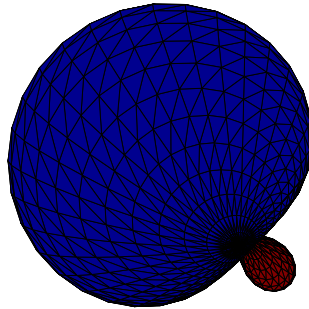


Figure 9: Directivity patterns formed by superposition of the spherical harmonics $(0, 0)$ and $(1, 1)$ from Fig. 3.

In conclusion spherical harmonics offer great flexibility for the design of arbitrary directivities by means of superposition. Illustrated in Fig. 9 is a directivity pattern formed by superposition of a spherical harmonic function of 0^{th} and one of 1^{st} order. As discussed later in Section 4.3.1, these orthonormal set of functions also offer a good method of analysing the room response's early reflections and single energy contributions when directivities are present. These constitute the main advantages over other functions like multipoles or spatial windows amongst others.

2.3.3 Matrix / Vector Notation Of The Spherical Harmonics And Multipoles

At this point it is possible to describe directivity patterns by means of the spherical harmonic functions $Y(\boldsymbol{\theta})$ and the multipoles $M_{lmn}(\boldsymbol{\theta})$ ¹⁵. The latter are used in combination with the RMM given their convenient relationship to the Green's function of a point source in free field. The spherical harmonic decomposition has proven to be a good method for the analysis of the room reflections in space. Therefore the conversion between the directional room responses on the basis of multipole characteristics into their spherical harmonic representation is necessary to facilitate the analysis presented in Section 4.3.

A matrix notation of the spherical harmonics and multipole characteristics has proven to be convenient when computing them for a large number of orders. The result of a matrix notation is a more compact representation of these functions for as many sources as illustrated in Fig. 20, where L defines the number of image sources and thus the number of rows found in $\mathbf{Y}(\boldsymbol{\theta})$. The number of columns is determined by the maximal spherical harmonic order as $(N_{SH} + 1)^2$. The vector storing the sampling points as a function of both spherical angles is given as:

$$\boldsymbol{\theta} = \begin{pmatrix} \boldsymbol{\theta}_1^T \\ \boldsymbol{\theta}_2^T \\ \vdots \\ \boldsymbol{\theta}_L^T \end{pmatrix} = \begin{pmatrix} \vartheta_1 & \varphi_1 \\ \vartheta_2 & \varphi_2 \\ \vdots & \vdots \\ \vartheta_L & \varphi_L \end{pmatrix}. \quad (25)$$

$\mathbf{Y}(\boldsymbol{\theta})$ is computed with the definition of the spherical angles vector as:

$$\mathbf{Y}(\boldsymbol{\theta}) = \begin{bmatrix} Y_0^0(\boldsymbol{\theta}_1) & Y_1^{-1}(\boldsymbol{\theta}_1) & Y_1^0(\boldsymbol{\theta}_1) & Y_1^1(\boldsymbol{\theta}_1) & \dots & Y_{N_{SH}}^{N_{SH}}(\boldsymbol{\theta}_1) \\ Y_0^0(\boldsymbol{\theta}_2) & Y_1^{-1}(\boldsymbol{\theta}_2) & Y_1^0(\boldsymbol{\theta}_2) & Y_1^1(\boldsymbol{\theta}_2) & \dots & Y_{N_{SH}}^{N_{SH}}(\boldsymbol{\theta}_2) \\ \vdots & \vdots & \vdots & \vdots & \ddots & \vdots \\ Y_0^0(\boldsymbol{\theta}_L) & Y_1^{-1}(\boldsymbol{\theta}_L) & Y_1^0(\boldsymbol{\theta}_L) & Y_1^1(\boldsymbol{\theta}_L) & \dots & Y_{N_{SH}}^{N_{SH}}(\boldsymbol{\theta}_L) \end{bmatrix} \quad (26)$$

A similar notation is used when computing $\mathbf{M}(\boldsymbol{\theta})$ containing the multipole coefficients for the chosen points in space and maximal multipole order N_{MP} . This matrix features L number of rows and $\frac{(N_{MP} + 1)(N_{MP} + 2)(N_{MP} + 3)}{6}$ number of columns. As a result this matrix will always feature more columns than $\mathbf{Y}(\boldsymbol{\theta})$ for the same orders $N_{SH} = N_{MP}$.

$$\mathbf{M}(\boldsymbol{\theta}) = \begin{bmatrix} M_{000}(\boldsymbol{\theta}_1) & M_{100}(\boldsymbol{\theta}_1) & M_{010}(\boldsymbol{\theta}_1) & M_{001}(\boldsymbol{\theta}_1) & \dots & M_{00N_{MP}}(\boldsymbol{\theta}_1) \\ M_{000}(\boldsymbol{\theta}_2) & M_{100}(\boldsymbol{\theta}_2) & M_{010}(\boldsymbol{\theta}_2) & M_{001}(\boldsymbol{\theta}_2) & \dots & M_{00N_{MP}}(\boldsymbol{\theta}_2) \\ \vdots & \vdots & \vdots & \vdots & \ddots & \vdots \\ M_{000}(\boldsymbol{\theta}_L) & M_{100}(\boldsymbol{\theta}_L) & M_{010}(\boldsymbol{\theta}_L) & M_{001}(\boldsymbol{\theta}_L) & \dots & M_{00N_{MP}}(\boldsymbol{\theta}_L) \end{bmatrix} \quad (27)$$

15. From now on the tilde is omitted in order to indicate the normalized multipoles $M_{lmn}(\boldsymbol{\theta})$ defined in Section 3.5.4 as used for the computer simulations.

2.3.4 Conversion Between Spherical Harmonics And Multipoles

A transformation matrix is needed in order to transform the results obtained using the RMM with directivity on the basis of multipoles into their spherical harmonic representation. As mentioned in the previous section, the spherical wave spectrum of any arbitrary function $a(\boldsymbol{\theta})$ on a sphere can be found by means of integration. If that function was to be a multipole $M_{lmn}(\boldsymbol{\theta})$ defined on a sphere, then its spherical wave spectrum can be found with Eq. 24 as:

$$M_{n'm'} = \int Y_{n'}^{m'}(\boldsymbol{\theta})^* M_{lmn}(\boldsymbol{\theta}) d\Omega. \quad (28)$$

It is precisely Eq. 28 that gives the relationship between spherical harmonics and multipoles. A distinction of the indices is here necessary because the orders of both functions are independent of each other. On the one hand there are multipoles $M_{lmn}(\boldsymbol{\theta})$ and on the other there are spherical harmonics $Y_{n'}^{m'}(\boldsymbol{\theta})$, where the apostrophe underlines the difference between a spherical harmonic of the n' order and m' degree and multipole derived $l + m + n$ times.

The multipole characteristic $M_{lmn}(\boldsymbol{\theta})$ is henceforth decomposed in its spherical wave spectrum as:

$$M_{lmn}(\boldsymbol{\theta}) = \sum_{n'=0}^{\infty} \sum_{m'=-n'}^{n'} M_{n'm'} Y_{n'}^{m'}(\boldsymbol{\theta}). \quad (29)$$

2.3.5 Conversion Matrix

The last equation cannot be computed for infinitely many orders n' , which is why a truncation of the sum is necessary when calculating the spherical wave spectrum $M_{n'm'}$. As a consequence, the function's spatial resolution is reduced subject to the maximal order n' of the first sum in Eq. 29. The complex coefficients $M_{n'm'}$ can be pre-computed for specific orders. The idea is to compute all possible combinations in order to facilitate a direct transform between room responses of arbitrary directivity on the basis of multipoles into their spherical harmonic equivalent and vice versa.

The problem is the fact that evaluating the spherical harmonics at all support angles ϑ and φ is not an easy task. Thus a more efficient method is required in order to solve Eq.28 for a great number of spherical harmonics and multipoles and at the same time retain a good accuracy of the spherical body. This problem can be solved by sampling the desired spherical body with a pattern defined by a finite set of 3-D points in space. The latter can be defined, as done in Section 2.3.3, with L number of spherical angular vectors.

Sampling The 3-D Sphere: A t -Design is a sampling pattern used for generating sampled spherical bodies with limited resolution. Some of the widely-used sampling patterns are illustrated in Fig. 10. Their advantages and disadvantages are discussed in detail in [Zot09b, Zot14b].

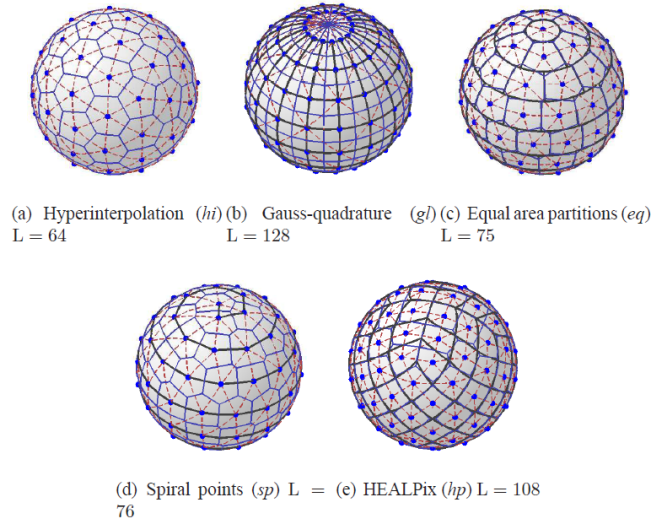


Figure 10: Examples of t -Designs with different values for L taken from [Zot14b].

The result of discretizing the sphere by means of a t -Design is an advantageous simplification of the integral given by Eq. 28 into a sum over a finite number L of spherical angles $\theta_l^T = [\cos \varphi_l \sin \vartheta_l, \sin \varphi_l \sin \vartheta_l, \cos \vartheta_l]^T$. The t -Design used in Section 4 can be found in Fig. 11. Its surfaces are defined by 180 Cartesian points in 3-D space.

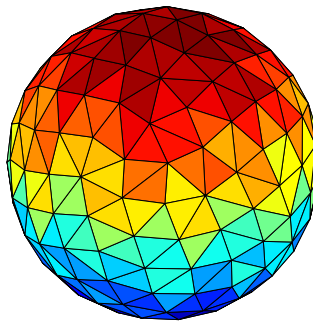


Figure 11: t -Design made out of 180 points in space.

By using one of the many t-Designs it becomes possible to compute the coefficients from their integral form in Eq. 28 into their finite resolution representation in Eq. 30. These coefficients hold the relationship between spherical harmonic and multipole functions and render a conversion between them possible. They will from now on be referred as the c – *coefficients* of the indices (n', m') and (l, m, n) . They are computed for L points in 3-D space as follows:

$$c_{n'm'}^{lmn} = \frac{4\pi}{L} \sum_{l=1}^L Y_{n'}^{m'}(\boldsymbol{\theta}_l) M_{lmn}(\boldsymbol{\theta}_l). \quad (30)$$

Thereby are $Y_{n'}^{m'}(\boldsymbol{\theta}_l)$ and $M_{lmn}(\boldsymbol{\theta}_l)$ the corresponding spherical harmonic and multipole coefficients at the l^{th} sample point in space. All the c -coefficients of predefined maximal orders N'_{SH} and N_{MP} can be computed and stored in a matrix enabling a one-to-one conversion between spherical-harmonic- and multipole-based room transfer function simulation with arbitrary directivities. How these coefficients are used in order to convert the simulations of room transfer functions with directivities on the basis of multipoles into their spherical-harmonic-based equivalents is described in Section 3.5.1.

Next the \mathbf{C} -matrix containing all c -coefficients is defined as:

$$\mathbf{C} = \mathbf{Y}(\boldsymbol{\theta})^T \cdot \mathbf{M}(\boldsymbol{\theta})$$

$$= \begin{bmatrix} c_{00}^{000} & c_{00}^{100} & c_{00}^{010} & c_{00}^{001} & \dots & c_{00}^{00N_{MP}} \\ c_{1-1}^{000} & c_{1-1}^{100} & c_{1-1}^{010} & c_{1-1}^{001} & \dots & c_{1-1}^{00N_{MP}} \\ c_{10}^{000} & c_{10}^{100} & c_{10}^{010} & c_{10}^{001} & \dots & c_{10}^{00N_{MP}} \\ c_{11}^{000} & c_{11}^{100} & c_{11}^{010} & c_{11}^{001} & \dots & c_{11}^{00N_{MP}} \\ \vdots & \vdots & \vdots & \vdots & \ddots & \vdots \\ c_{N_{SH}N_{SH}}^{000} & c_{N_{SH}N_{SH}}^{100} & c_{N_{SH}N_{SH}}^{010} & c_{N_{SH}N_{SH}}^{001} & \dots & c_{N_{SH}N_{SH}}^{00N_{MP}} \end{bmatrix}, \quad (31)$$

where $c_{n'm'}^{lmn}$ is the c -coefficient between a spherical harmonic of the order and degree (n', m') and a multipole created by means of (l, m, n) derivatives of the monopole with respect to the (x, y, z) axis. A \mathbf{C} -matrix featuring a colour bar representing its energy levels in dB is exemplarily illustrated in Fig. 12 by evaluating $20 \log_{10}(|\mathbf{C}|)$.

This non-square matrix will be $(N_{SH} + 1)^2$ times $\frac{(N_{MP} + 1)(N_{MP} + 2)(N_{MP} + 3)}{6}$. Its dimensions follow from two numbers, the first one represents the number of existing spherical harmonics up to the maximal order N_{max} . The second is the number of existing multipoles up to a maximal N_{MP} number of derivatives of the monopole. Both orders determine the maximal spatial resolution possible for that order.

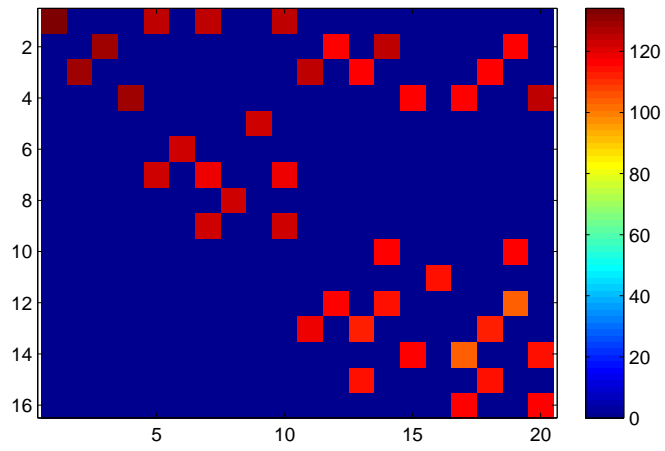


Figure 12: Colour plot of a \mathbf{C} -matrix for $N_{SH} = N_{MP} = 3$.

3 Shoebox Shaped Room With Rigid Walls

3.1 The Room Modes Method

3.1.1 Homogeneous Solution

Next, the wave equation is to be solved in rectangular enclosures, where rigid walls impose sound-hard boundary conditions. The goal is to find the functions that fulfill both the wave equation and the room's boundary conditions. Here, the procedure is carried out for the x -coordinate only. The desired solution for $p_n(r)$ in Eq.36 is obtained after applying the same procedure to the y - and z -coordinate. The approach for the 1-D problem consists of the superposition of two waves, which means that the sound pressure measured at a point x in space is the result of an in- and out-going wave. The relation reads as

$$p(x) = ae^{ik_x x} + be^{-ik_x x}.$$

As already mentioned before, totally reflecting and massive walls are assumed for the rectangular room. Six reflecting surfaces forming the shoebox shaped room are placed at

$$x = \{0, L_x\}, y = \{0, L_y\} \text{ and } z = \{0, L_z\}. \quad (32)$$

The boundary conditions impose that the normal components of the particle velocity $v_x(x=0) = 0$. The derivative of the pressure with respect to x must vanish at those points due to the 1-D Euler equation.

$$\dot{v}_x \propto \frac{\partial}{\partial x} p(x=0) = 0. \quad (33)$$

From Eq. 33 it follows that

$$\begin{aligned} \frac{\partial}{\partial x} p(x=0) &= (ik_x)ae^{ik_x x} + (-ik_x)be^{-ik_x x} \\ &= (ik_x)(ae^{ik_x x} - be^{-ik_x x}) = 0. \end{aligned}$$

The velocity at $x=0$ must be zero and thus $ae^0 - be^0 = 0$. This condition is fulfilled by $a = b$. The choice $a = b = \frac{1}{2}$ yields a compact expression for the boundary condition at $x=0$:

$$p(x) = \frac{e^{ik_x x} + e^{-ik_x x}}{2} = \cos(k_x x). \quad (34)$$

The other boundary condition located at $x = L_x$ requires that $v_x(x = L_x) = 0$ and hence

$$\frac{\partial}{\partial x} p(x = L_x) = \frac{\partial}{\partial x} \cos(k_x L_x) = -k_x \sin(k_x L_x) = 0.$$

This boundary condition can only be fulfilled by $k_x = \frac{\pi}{L_x} l_x$. Thus the solution for $p(x)$ fulfilling both boundary conditions is

$$p(x) = \cos\left(\frac{\pi}{L_x} l_x \cdot x\right), \quad \text{for all } l_x \in \mathbb{N}_0. \quad (35)$$

Doing this for each coordinate separately yields the solution for the 3-D problem:

$$\begin{aligned} p_n(\mathbf{r}) &= p(x) \cdot p(y) \cdot p(z) \\ &= \cos\left(\frac{\pi}{L_x} l_x x\right) \cdot \cos\left(\frac{\pi}{L_y} l_y y\right) \cdot \cos\left(\frac{\pi}{L_z} l_z z\right), \end{aligned} \quad (36)$$

where the subscript n stands for the *normal* modes that arise in rectangular rooms with rigid walls. The characteristic equation (Eq. 8) requires that

$$k^2 = \left(\frac{2\pi f}{c}\right)^2 = k_x^2 + k_y^2 + k_z^2, \quad (37)$$

allowing only discrete frequencies in the homogeneous solution. The so-called eigenfrequencies are obtained for $l_x, l_y, l_z \in \mathbb{N}_0$ when solving Eq. 37 for f .

$$f(l_x, l_y, l_z) = \frac{c}{2} \sqrt{\left(\frac{l_x}{L_x}\right)^2 + \left(\frac{l_y}{L_y}\right)^2 + \left(\frac{l_z}{L_z}\right)^2} \quad (38)$$

3.1.2 Non-Homogeneous Solution

The solution to Green's problem for the 3-D non-homogeneous wave equation¹⁶ can be solved by finding G through a combination of *Laplace* (with respect to time) and

16. Linear partial differential equation of 2^{nd} order used for describing waves.

Fourier (with respect to the spatial coordinates) transforms. The explicit approach for solving Green's problem for point sources under free-field conditions is found in Appendix A. Here, the solution to the non-homogeneous problem for enclosed spaces with parallel and rigid walls is presented. The general solution disregarding the boundary conditions at first reads as follows:

$$G(\mathbf{r}, t) = \frac{1}{2\pi i} \oint_c e^{st} \frac{1}{(2\pi)^d} \int_{\mathbb{R}^d} e^{i\mathbf{k}^T \mathbf{r}} g(\mathbf{k}, s) \, d\mathbf{k} \, ds. \quad (39)$$

The time-dependent solution in space is computed by means of inverse Fourier and Laplace transforms of $g(\mathbf{k}, s)$. The approach used here in order to find the non-homogeneous solution $G(\mathbf{r}, t)$ consists of time and local exponential functions weighted with a coefficient γ . $G(\mathbf{r}, t)$ can be computed with $s = i\omega$ as:

$$G(\mathbf{r}, t) = \int \int \gamma e^{i\mathbf{k}^T \mathbf{r}} e^{i\omega t} \, d\omega \, d\mathbf{k}, \quad (40)$$

where $\mathbf{k}^T = [k_x, k_y, k_z]^T$ and $\mathbf{r}^T = [x, y, z]^T$. Hereby defines \mathbf{k} the \mathbf{k} -space and must not be mistaken with the wavenumber k . As $e^{i\mathbf{k}^T \mathbf{r}}$ does not fulfill the boundary conditions, the solution is constructed with the homogeneous solution from Section 3.1.1 for point sources in enclosed spaces with parallel and rigid walls. The latter in its truncated form¹⁷ will be written as $\psi_l(\mathbf{r})$ where l represents a mode combination of the indices l_x, l_y and l_z . The orthonormal basis solution for $D = 3$ in the Fourier domain reads as:

$$\begin{aligned} \psi_l(\mathbf{r}) &= \prod_{d=0}^D \sqrt{\frac{2 - \delta_{l_d}}{L_d}} \cos\left(\frac{\pi l_d}{L_d} r_d\right) \\ &= \sqrt{\frac{(2 - \delta_{l_x})(2 - \delta_{l_y})(2 - \delta_{l_z})}{L_x L_y L_z}} \cos\left(\frac{\pi l_x}{L_x} x\right) \cos\left(\frac{\pi l_y}{L_y} y\right) \cos\left(\frac{\pi l_z}{L_z} z\right). \end{aligned} \quad (41)$$

An important consequence of Eq. 36 is the discretisation of the eigenvalues through the integer indices given that $\mathbf{k} = [k_x, k_y, k_z]^T = \left[\frac{\pi l_x}{L_x}, \frac{\pi l_y}{L_y}, \frac{\pi l_z}{L_z}\right]^T$. As a result, the integral over $d\mathbf{k}$ in Eq. 40 becomes a sum over $L = (l_{max} + 1)^D$ modal combinations of the discrete indices (l_x, l_y, l_z) to

$$G(\mathbf{r}, t) = \int_{-\infty}^{\infty} \sum_{l=1}^L \gamma \psi_l(\mathbf{r}) e^{i\omega t} \, d\omega. \quad (42)$$

17. This means that Eq. 36 will not be summed for infinitely many modes, but for a limited number L of modes combinations that are taken into consideration.

Inserting this result for the Green's function in the time-dependent wave equation $\left(\Delta - \frac{1}{c^2} \frac{\partial^2}{\partial t^2}\right) G = -\delta(t)$ yields

$$\begin{aligned} \int_{-\infty}^{\infty} \sum_l^L \gamma \left(\frac{-\omega_l^2}{c^2} - \frac{-\omega^2}{c^2} \right) \psi_l(\mathbf{r}) e^{i\omega t} d\omega &= -\delta(t)\delta(\mathbf{r} - \mathbf{r}_0) \\ \int_{-\infty}^{\infty} \sum_l^L \frac{\gamma}{c^2} (\omega^2 - \omega_l^2) \psi_l(\mathbf{r}) e^{i\omega t} d\omega &= -\delta(t)\delta(\mathbf{r} - \mathbf{r}_0). \end{aligned} \quad (43)$$

Eq. 43 is obtained given that $\frac{\partial^2}{\partial t^2} G(\mathbf{r}, t) = (i\omega)^2 G(\mathbf{r}, t) = -\omega^2 G(\mathbf{r}, t)$ and by applying the Laplacian to the homogeneous solution:

$$\begin{aligned} \Delta \psi_l(\mathbf{r}) &= \left[\frac{\partial^2}{\partial x^2} + \frac{\partial^2}{\partial y^2} + \frac{\partial^2}{\partial z^2} \right] \psi_l(\mathbf{r}) \\ &= \left[-\left(\frac{\pi l_x}{L_x} \right)^2 - \left(\frac{\pi l_y}{L_y} \right)^2 - \left(\frac{\pi l_z}{L_z} \right)^2 \right] \psi_l(\mathbf{r}) \\ &= -[k_x^2 + k_y^2 + k_z^2] \psi_l(\mathbf{r}) = -k_l^2 \psi_l(\mathbf{r}) \\ &= -\frac{\omega_l^2}{c^2} \psi_l(\mathbf{r}). \end{aligned}$$

The subscript refers here to the l^{th} index combination and corresponding discrete frequency ω_l . With these last results Eq. 43 is now transformed with $\int \int e^{-i\omega' t} \psi_{l'}(\mathbf{r}) d\mathbf{r} dt$ resulting in

$$\begin{aligned} \int_{-\infty}^{\infty} \sum_l^L \frac{\gamma}{c^2} (\omega^2 - \omega_l^2) \int_V \psi_l(\mathbf{r}) \psi_{l'}(\mathbf{r}) d\mathbf{r} \int_{-\infty}^{\infty} e^{i(\omega - \omega')t} dt d\omega &= - \int \delta(t) e^{-i\omega' t} \\ &\int \delta(\mathbf{r} - \mathbf{r}_0) \psi_{l'}(\mathbf{r}) d\mathbf{r}. \end{aligned}$$

The equation can be simplified since $\int_V \psi_l(\mathbf{r}) \psi_{l'}(\mathbf{r}) d\mathbf{r} = \delta_{ll'}$ for all limited volumes V , and by applying the Fourier identity of $\int e^{i(\omega - \omega')t} dt = 2\pi\delta(\omega - \omega')$ to

$$\int_{-\infty}^{\infty} \sum_l^L \frac{\gamma}{c^2} (\omega^2 - \omega_l^2) \delta_{ll'} 2\pi \delta(\omega - \omega') d\omega = -1 \cdot \psi_{l'}(\mathbf{r}_0). \quad (44)$$

Both sum and integral vanish because $\int f(\omega) \delta(\omega - \omega') d\omega = f(\omega')$ and $\sum_l \delta_{ll'} = \begin{cases} 1 & \text{if } l = l', \\ 0 & \text{else.} \end{cases}$.

Finally the coefficients γ remain:

$$\begin{aligned} \frac{\gamma}{c^2} (\omega^2 - \omega_l^2) 2\pi &= -\psi_l(\mathbf{r}_0) \\ \gamma &= -\frac{c^2}{2\pi} \frac{\psi_l(\mathbf{r}_0)}{(\omega^2 - \omega_l^2)}. \end{aligned} \quad (45)$$

γ will now be carefully transformed into the time-domain when inserting it into Eq. 43. First it has to be decomposed in its partial fractions $\frac{1}{\omega^2 - \omega_l^2} = \frac{A}{\omega - \omega_l} + \frac{B}{\omega + \omega_l}$ by finding the two constants A and B for the corresponding poles $\pm \omega_l$.

The partial fraction decomposition yields

$$\begin{aligned} \frac{1}{\omega^2 - \omega_l^2} &= \frac{A}{\omega - \omega_l} + \frac{B}{\omega + \omega_l} \\ &= \frac{A(\omega + \omega_l) + B(\omega - \omega_l)}{\omega^2 - \omega_l^2}. \end{aligned} \quad (46)$$

From Eq.46 it follows that $B = \frac{-1}{2\omega_l}$ and $A = -B$. Thus $A = \frac{1}{2\omega_l}$ and we get γ in partial fractions

$$\gamma = -\frac{c^2}{4\pi\omega_l} \psi_l(\mathbf{r}_0) \left[\frac{1}{\omega - \omega_l} - \frac{1}{\omega + \omega_l} \right]. \quad (47)$$

The Green's function that satisfies the wave equation can be computed from insertion of Eq. 47 into Eq. 42:

$$G(\mathbf{r}, t) = -\sum_l^L \frac{c^2}{4\pi\omega_l} \psi_l(\mathbf{r}_0) \psi_l(\mathbf{r}) \int_{-\infty}^{\infty} \left[\frac{e^{i\omega t}}{\omega - \omega_l} - \frac{e^{i\omega t}}{\omega + \omega_l} \right] d\omega. \quad (48)$$

The next step consists on transforming Eq. 48 back to a causal time-dependent solution. The improper integral can be solved with Jordan's lemma¹⁸ as a contour integral over

18. Tool used in complex analysis together with the residue theorem in order to compute integrals from real analysis. The function is integrated over a closed path C going from the negative to the positive real axis and in a semi-circle back to the starting point.

the closed path C in form of an infinitely big semi-circle in the imaginary plane ω as long as the integrand $e^{i\omega t}$ vanishes. This will be the case for $t > 0$ as long as C_+ passes the positive imaginary axis given that $\lim_{\omega \rightarrow i\infty} e^{i\omega t} = e^{-\infty t}$. For $t < 0$ on the other hand, the semi-circle C_- has to pass the negative imaginary axis in order for the integrand to vanish, thus $\lim_{\omega \rightarrow -i\infty} e^{-i\omega t} = e^{-\infty t}$.

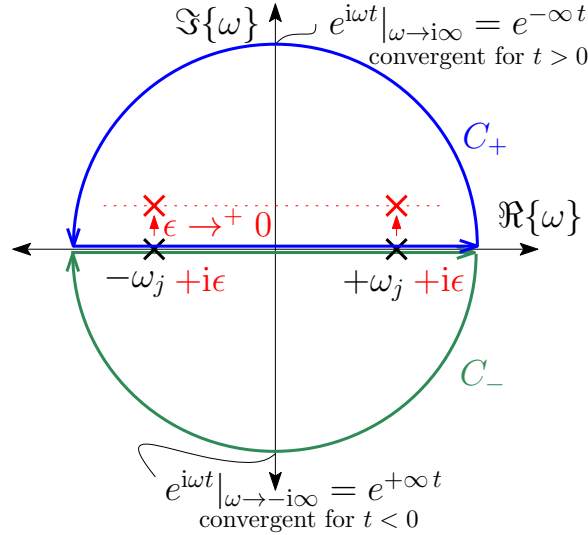


Figure 13: Regularization of the real poles $\pm \omega_l$ as illustrated by Zotter in [Zot14b].

Both integral paths pass, as illustrated in Fig. 13, over the real-valued poles $\pm \omega_l$. This represents a major problem because the integral in Eq. 48 cannot be evaluated at those angular frequencies. The solution proposed here is to apply an infinitesimal shift of the poles towards the interior of the curve C_+ . The contour integral is solved with the *Residue Theorem* presented in Appendix A for each of the terms separately as $\oint \frac{f(\omega)}{\omega - \omega_0} = 2\pi i f(\omega_0)$. In this way it becomes possible to integrate the analytical function $f(\omega) = e^{i\omega t}$ over the shifted poles $\pm \omega_l + i\epsilon$.

The residues of the new defined poles can be computed from Eq. 48. Note that the solution is zero at negative times $t < 0$ because C does not contain poles. For C_+ and positive times $t \geq 0$ we obtain a causal solution. The Green's function is computed with the sine exponential identity as:

$$\begin{aligned}
 G(\mathbf{r}, t) &= - \sum_l^L \frac{c^2}{4\pi\omega_l} \psi_l(\mathbf{r}_0) \psi_l(\mathbf{r}) 2\pi i \lim_{\epsilon \rightarrow 0^+} \left[f(\omega_l + i\epsilon) - f(-\omega_l + i\epsilon) \right] \\
 &= - \sum_l^L \frac{c^2}{2\omega_l} \psi_l(\mathbf{r}_0) \psi_l(\mathbf{r}) i \lim_{\epsilon \rightarrow 0^+} \left[e^{i(\omega_l + i\epsilon)t} - e^{i(-\omega_l + i\epsilon)t} \right]
 \end{aligned}$$

$$\begin{aligned}
&= - \sum_l^L \frac{c^2}{2\omega_l} \psi_l(\mathbf{r}_0) \psi_l(\mathbf{r}) i \lim_{\epsilon \rightarrow 0^+} \left[e^{(i\omega_l - \epsilon)t} - e^{(-i\omega_l - \epsilon)t} \right] \\
&= - \sum_l^L \frac{c^2}{2\omega_l} \psi_l(\mathbf{r}_0) \psi_l(\mathbf{r}) i 2i \sin(\omega_l t) \lim_{\epsilon \rightarrow 0^+} e^{-\epsilon t} \\
&= \sum_l^L \frac{c^2}{\omega_l} \psi_l(\mathbf{r}_0) \psi_l(\mathbf{r}) \sin(\omega_l t) \lim_{\epsilon \rightarrow 0^+} e^{-\epsilon t} \\
&= \sum_l^L c^2 \psi_l(\mathbf{r}_0) \psi_l(\mathbf{r}) \frac{\sin(\omega_l t)}{\omega_l} \cdot \frac{t}{t} \lim_{\epsilon \rightarrow 0^+} e^{-\epsilon t}.
\end{aligned}$$

The distinction between the cases $t \geq 0$ and $t < 0$ can be elegantly expressed by employing the unit step function $u(t)$ ¹⁹. The Green's function in rectangular room's with rigid walls is given with the sinc function $\text{sinc}(x) = \frac{\sin(x)}{x}$ by:

$$G(\mathbf{r}, t) = c^2 t \sum_l^L \psi_l(\mathbf{r}_0) \psi_l(\mathbf{r}) \text{sinc}(\omega_l t) u(t) \lim_{\epsilon \rightarrow 0^+} e^{-\epsilon t}. \quad (49)$$

This Green's function is valid in shoebox shaped rooms with perfectly reflecting walls for point sources and receivers, where the homogeneous solution has been found by means of the normal modes. How room responses are computed for sources and receivers of arbitrary directivities is discussed in Section 3.5.3. For now, the solution to the non-homogeneous problem has been found and is available in the form of Eq. 49 for rigid walls. The choice of ϵ and how to adjust it to simulate the quantity of energy absorbed by the walls is treated in Section 4.1.2.

3.1.3 Filters

The solution in form of Eq. 49 can be used in order to compute room impulse responses on the basis of modes. The truncation of the infinite sum to a finite number of modes constitutes the method's main problem. It will never deliver the perfect solution once the truncation has been introduced. This is the case for both the low and high frequency bands. The band limitation results in an abrupt truncation of the frequency response in the higher frequency range. Modes that are too close to this cut-off frequency would still have an influence in the computed transfer function. In the same way, the low frequency domain will not be correct either. The finite summation has also an influence for lower frequencies given the mode's influence between each other. Also, the 0^{th} mode, i.e. for $l_x = l_y = l_z = 0$, results in a corruption of the time domain signals. These two problems can be reduced to a certain extent by filtering the RIR with adequate filters. However,

19. Discontinuous function defined as $u(t) = \begin{cases} 0 & \text{if } t < 0, \\ 1 & \text{else.} \end{cases}$

without fully removing inaccuracy due to the truncation of the mode summation.

High-Pass Filter

The 0^{th} mode introduces a problem for the derivations used in Section 3.5.3 when dividing by zero. It is absolutely necessary to filter it with a high-pass filter. The choice fell here for a *Butterworth*²⁰ filter of 2^{nd} order, whose frequency response is steep enough in order to exclude the resonance frequency $0Hz$ of the 0^{th} mode. The next mode is found high enough in frequency in order for it to pass with little influence from the filter. Its magnitude response is exemplarily illustrated in Fig. 14, where the cut-off frequency f_{cut} has been chosen to be the first non-zero room mode. The latter is found for this case at around $38Hz$.

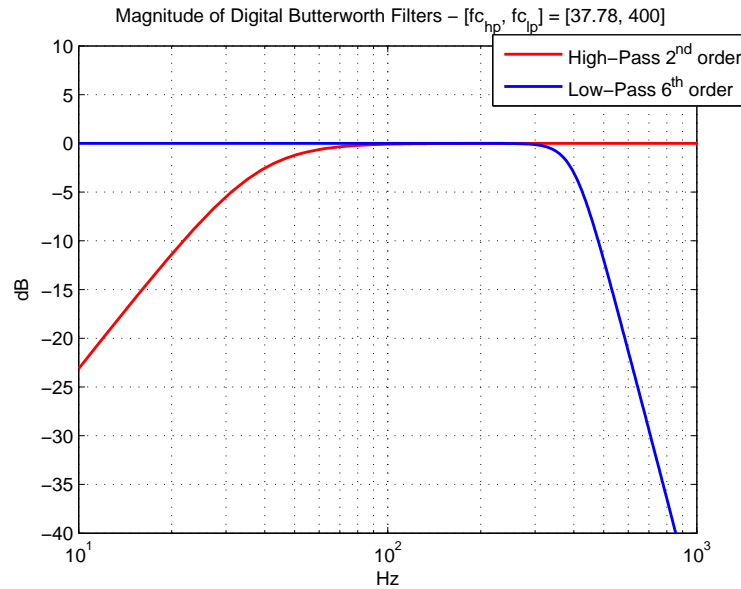


Figure 14: Low- and high-pass magnitude responses.

Low-Pass Filter

The influence of modes in the vicinity of the barrier frequency f_b is damped with a Butterworth low-pass filter of 6^{th} order. The barrier frequency defines here the highest frequency mode taken for the simulation. Thus the influence of an abrupt truncation can be minimized with the right choice for the filter's cut-off frequency. Illustrated in Fig. 14 is such a filter for $(f_b, f_{cut}) = (800, 400)$, meaning that the filter's cut-off frequency has

20. A Butterworth filter is a signal processing filter designed to have in the passband as flat a frequency response as possible. Its gain is defined in terms of its transfer function and order as $G^2(\omega) = |H(i\omega)|^2 = \frac{G_0}{1 + (\frac{\omega}{\omega_c})^{2n}}$.

been chosen to be half the barrier frequency. As seen for the blue curve, a maximum attenuation of $-36dB$ can be achieved at f_b . A higher attenuation is thinkable and adjustable via the filter's order.

The result of filtering the RIR with a low-pass filter of 6^{th} order is a phase shift of the time domain signal itself. The latter will grow with the filter's order, which is why another solution is necessary given that higher filter orders are necessary in order to filter modes in higher frequencies. It is important to remember the fact that modes will be closer to each other at high frequency ranges. The high frequency domain is thus densely filled with room modes. The influence of an abrupt truncation is therefore more significant when considering a great number of room modes.

A solution avoiding the group-delay of the low-pass is to use a zero-phase filter.²¹ With it, there is no additional group delay. Each of the filtering steps are visible in Fig. 15 and Fig. 16, respectively. The original RIR is depicted in black, where the influence of the 0^{th} mode becomes evident. Its rising tendency is repressed once the high-pass filter is applied. As seen for the red curve, the signal's ripple for the very first time instances is still present. This disturbing effect is removed by applying the low-pass filter resulting in the black curve in Fig. 16. The resulting phase shift is clearly given when comparing it to the blue curve, for which a zero-phase filter was used. The direct sound is plotted in form of the magenta line, which signalizes the accuracy of the achieved filtering process.

The last curves can be analyzed in the Fourier domain too. It is precisely in this domain where all modes are better indicated. The influence of each of the filters can be best appreciated, as seen in Fig. 16, in the frequency domain. The frequency dependent increase and decrease of the magnitude response is visible as well as the barrier frequency, which was set to be $f_b = 800Hz$. This means that only modes until f_b were considered. The simulations as presented in Section 4 correspond to the filtered signal represented by the blue curves of Fig. 15 and Fig. 16. These filters were also applied to the simulations done with the ISM in order to ensure a qualitative comparison between both methods.

3.2 Analogy Between The RMM And ISM

The solution to Eq. 48 when rigid walls are present reads in \mathbf{k} -space as:

$$P(k, \mathbf{r}, \mathbf{r}') = \frac{1}{V} \sum_{l=-\infty}^{\infty} \frac{\psi_l(\mathbf{r}) \psi_l(\mathbf{r}')}{k_l^2 - k^2}, \quad (50)$$

where l indicates, as defined in [Kut09], a 3-D sum over the modal indices l_x , l_y and l_z in

²¹. Filter considered to have a linear response. As a result, the influence on the signals phase is minimal.

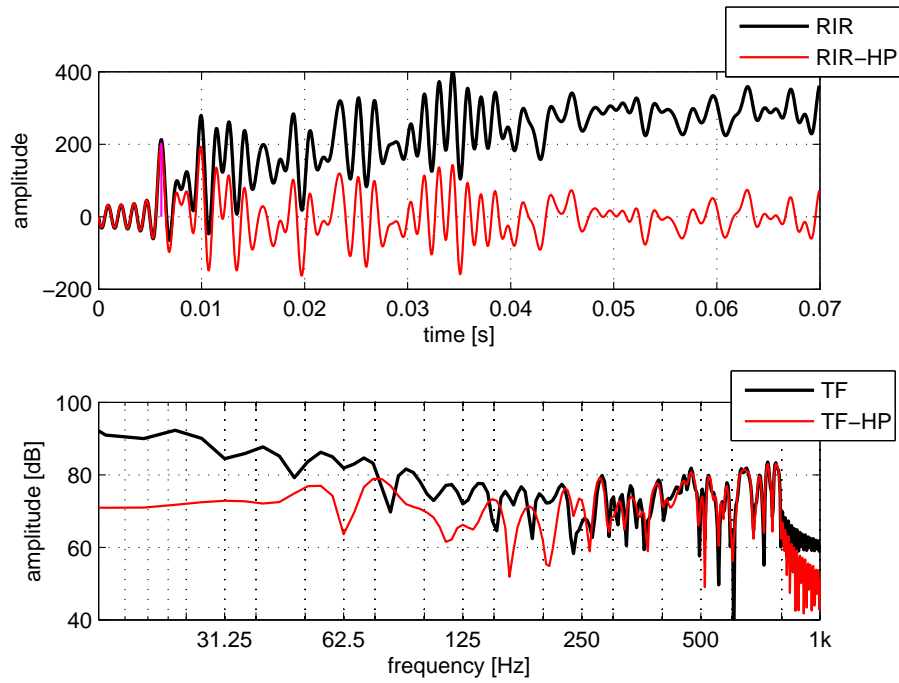


Figure 15: RIR and frequency domain representation of a signal filtered with a high-pass filter of 2^{nd} order.

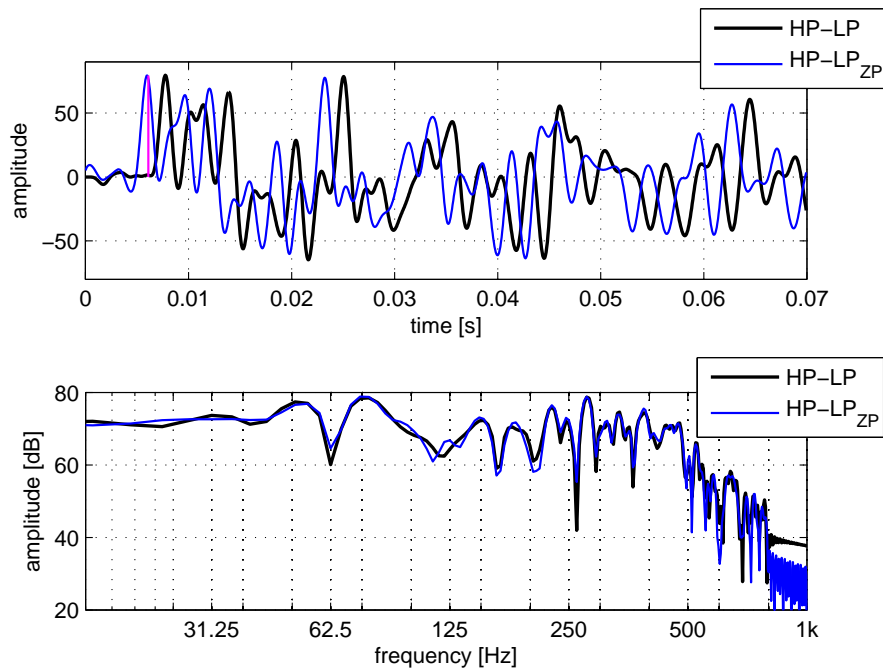


Figure 16: RIR and frequency domain representation of the signal in Fig. 15 filtered with a low-pass filter 6^{th} order and its zero-phase implementation.

the form of $\psi_l = \cos\left(\frac{\pi l_x}{L_x}x\right) \cos\left(\frac{\pi l_y}{L_y}y\right) \cos\left(\frac{\pi l_z}{L_z}z\right)$. At present the result obtained so far is valid for omni-directional characteristics only. The two cosine terms in Eq. 50 can be multiplied once they have been expanded with their exponential identity as proposed in [AB78]. The result summarized yields a compact notation for infinitely many point sources in free field as:

$$P(k, \mathbf{r}, \mathbf{r}') = \frac{1}{8V} \sum_{l=-\infty}^{\infty} \sum_{h=0}^7 \frac{e^{-i\mathbf{k}_l^T \mathbf{r}_h}}{k_l^2 - k^2}. \quad (51)$$

Thereby represents $\mathbf{r}_h = [x \pm x', y \pm y', z \pm z']$ the seven permutations of the primary source as illustrated in Fig. 17.

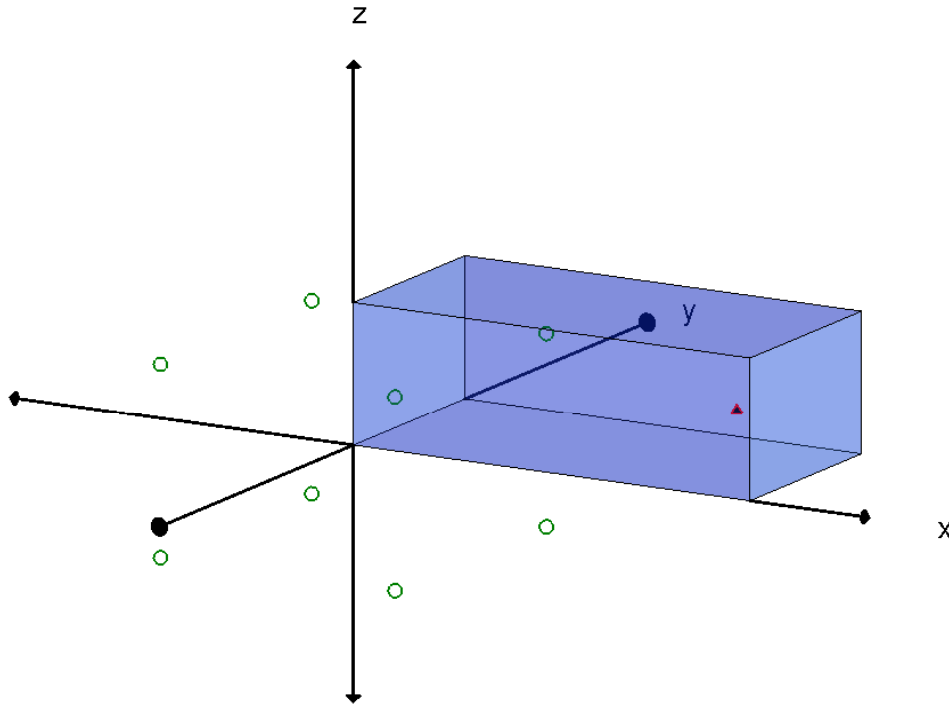


Figure 17: The main block is formed out of eight sources in green. Seven of them are images of the primary source placed in the blue rectangular room.

Although the ISM assumes free-field conditions, the delimiting surfaces are illustrated in order to get a good idea of the imaging process done for a shoebox shaped room. Thus the simulation of the RIR in an enclosed space is done in free field by adding the contribution of every image source at the receiver position. The reason why this concept is so prevalent lies in the fact that satisfactory results can be achieved through simple computational operations. The practical use of the ISM for the simulation of room impulse responses in rectangular rooms is treated and discussed in [AB78].

Following [AB78], Eq. 51 can be expanded with the integral property of the delta distribution from Section 3.1.2, with $\|\boldsymbol{\xi}\|^2 = |\xi_x|^2 + |\xi_y|^2 + |\xi_z|^2$, and $d^3\xi = d\xi_z d\xi_y d\xi_x$. It yields

$$\begin{aligned} P(k, \mathbf{r}, \mathbf{r}') &= \frac{1}{8V} \sum_{h=0}^7 \int \int \int_{-\infty}^{\infty} \frac{e^{-i\boldsymbol{\xi}^T \mathbf{r}_h}}{\|\boldsymbol{\xi}\|^2 - k^2} \sum_{l=-\infty}^{\infty} \delta(\boldsymbol{\xi} - \mathbf{k}_l) d^3\xi \\ &= \frac{1}{8V} \sum_{h=0}^7 \int \int \int_{-\infty}^{\infty} \frac{e^{-i\boldsymbol{\xi}^T \mathbf{r}_h}}{\|\boldsymbol{\xi}\|^2 - k^2} \\ &\quad \sum_{l=-\infty}^{\infty} \delta(\xi_x - k_x) \delta(\xi_y - k_y) \delta(\xi_z - k_z) d\xi_z d\xi_y d\xi_x. \end{aligned} \quad (52)$$

Further, when using the Fourier identity $\sum_{l_x=-\infty}^{\infty} \delta\left(\xi_x - \frac{\pi l_x}{L_x}\right) = \frac{L_x}{\pi} \sum_{l_x=-\infty}^{\infty} e^{i2L_x l_x \xi_x}$ for y and z too, it is possible to transform Eq. 52 into

$$\begin{aligned} P(k, \mathbf{r}, \mathbf{r}') &= \frac{1}{8V} \cdot \frac{L_x L_y L_z}{\pi^3} \sum_{h=0}^7 \int \int \int_{-\infty}^{\infty} \frac{e^{-i\boldsymbol{\xi}^T \mathbf{r}_h}}{\|\boldsymbol{\xi}\|^2 - k^2} \\ &\quad \sum_{l_x=-\infty}^{\infty} \sum_{l_y=-\infty}^{\infty} \sum_{l_z=-\infty}^{\infty} e^{i2L_x l_x \xi_x} e^{i2L_y l_y \xi_y} e^{i2L_z l_z \xi_z} d\xi_z d\xi_y d\xi_x \\ &= \frac{1}{8\pi^3} \sum_{h=0}^7 \int \int \int_{-\infty}^{\infty} \sum_{l=-\infty}^{\infty} \frac{e^{-i\boldsymbol{\xi}^T (\mathbf{r}_h - \mathbf{r}_l)}}{\|\boldsymbol{\xi}\|^2 - k^2} d^3\xi, \end{aligned} \quad (53)$$

where V represents the room's volume and the vector $\mathbf{r}_l^T = 2[L_x l_x, L_y l_y, L_z l_z]^T$ defines the l^{th} shift of the h^{th} source in space. Eq. 53 can be solved in an elegant manner with the result for the field of a point source under free-field conditions from Appendix A. As identified in [AB78], the triple integral is just a plane wave expansion for a point source in free field given that $\frac{e^{-ik\|\mathbf{r}\|}}{4\pi\|\mathbf{r}\|} = \frac{1}{8\pi^3} \int \int \int_{-\infty}^{\infty} \frac{e^{-i\boldsymbol{\xi}^T \mathbf{r}}}{\|\boldsymbol{\xi}\|^2 - k^2} d^3\xi$. The field of a point source driven by the angular frequency in $k = \frac{\omega}{c}$ in a rectangular room with rigid walls can ultimately be written as

$$P(k, \mathbf{r}, \mathbf{r}') = \sum_{h=0}^7 \sum_{l=-\infty}^{\infty} \frac{e^{-ik\|\mathbf{r}_h - \mathbf{r}_l\|}}{4\pi\|\mathbf{r}_h - \mathbf{r}_l\|}. \quad (54)$$

The last result corresponds, when inversely Fourier transformed, to the one obtained in the time domain. Hence the RMM method is directly related to the ISM. This means that both methods are equivalent and deliver the perfect solution when summed over

infinitely many modes and image sources, respectively. It is important to notice that both methods deliver the RIR for point sources and omni-directional receivers only. Their expansion with arbitrary directivities is presented in Section 3.5.

Moreover, the analogy between both methods becomes evident when analyzing Eq. 52 and thus the equivalence between Eq. 54 and Eq. 59 for the computation of RIR in rectangular rooms with rigid walls. This is done through a multiplication of the free-field solution of a point source with spaced delta distributions. The direct consequence is the periodicity in \mathbf{k} -space of the main block containing the seven permutations of the primary source, that answers to the periodicity found in the cosine functions from $\psi_l(\mathbf{r})$ and thus of $P(k, \mathbf{r}, \mathbf{r}')$ too.

This insight is not only enlightening but is also backed up by the convolution theorem²² when applied to Eq. 60. As seen in Section 3.3, the multiplications with the delta distributions in \mathbf{k} -space have become a convolution in three dimensional space between the free-field solution $G(\mathbf{r}, \mathbf{r}')$ and $\delta(r_i \pm 2l_i L_i)$.

3.3 The Image Source Method

The ISM can be explained by means of *geometrical room acoustics*. This domain of room acoustics describes sound propagation in terms of rays and concerns the frequency domain for which the wavelength of sound is small when compared to the room dimensions. It is not a matter of sound waves anymore but rather of sound rays²³ that arise as soon as $\lambda \ll (L_x, L_y, L_z)$. The latter define again the geometry of the room in the (x, y, z) coordinates. These rays travel in well-defined directions and follow the same propagation laws as light rays do. Their energy will remain constant provided the medium does not cause any energy losses. As for every spherical wave, their amplitude will fall directly proportional to $\frac{1}{r}$ where r denotes the distance to the ray's origin. It is precisely these kind of waves that are radiated and picked up and without any angle dependency by point sources and receivers. Therefore, the results obtained from the following considerations are valid for point sources and receivers only. For more information concerning room acoustics from a geometrical point of view refer to [Kut09, Goe06] et al.

The situation as it is in reality is exemplarily illustrated in Fig. 18. Here the sound rays and their paths towards the receiver position can be seen. A sound ray that is reflected once before arriving at the receiver position is called a reflection of 1st order. Thus the ray's order is defined as the number of reflections the ray undergoes before arriving at the receiver position. In this example only the direct sound and some reflections of 1st

22. The convolution theorem states that $\mathcal{F}(f * g) = \mathcal{F}(f) \cdot \mathcal{F}(g)$. This means that the Fourier transform of a convolution is the pointwise product of the Fourier transforms.

23. Small portion of a spherical wave with a vanishing aperture which originates from a certain point in space.

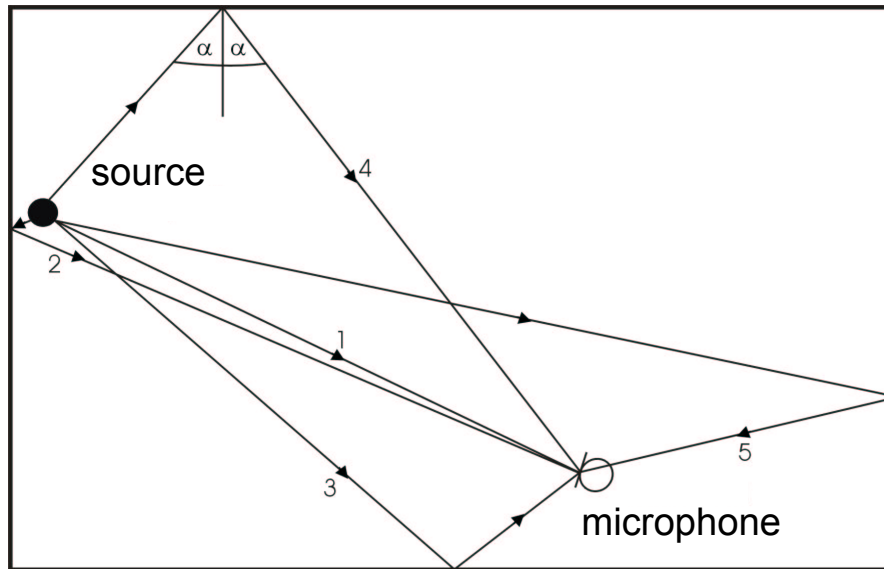


Figure 18: Direct sound (1) and 1st order reflections (2-5) of a point source in a rectangular room.

order are illustrated.

Concretely, the image process consists in mirroring the primary source with respect to the six delimiting surfaces forming the shoebox shaped room.²⁴ The image sources are identical to the primary source, meaning they radiate the same signal with the same intensity and phase. The next considerations are done for the 2-D case, that result in the 3-D solution when done considering the zenith angle as well.

Illustrated in Fig. 19 is the mirroring process in 2-D. Here, the first image source has been placed at the mirrored position of the primary source $[x_1, y_1]^T$ with respect to the first delimiting surface. If the latter is placed at $x_0 = 0$, then the first image source is found at $[-x_1, y_1]^T$ or twice the distance between primary source and first boundary condition. Both sources are identical to each other and as a result they must generate the same fields. Consequently the difference between them and thus the sound pressure's gradient must be null at the mirroring point x_0 precisely. This important conclusion can be seen as a direct relationship between the ISM and RMM as written in Eq. 33.

For rectangular rooms there is a pair of parallel surfaces in every dimension. This means that a second image source has to be mirrored with respect to the other delimiting surface at L_x . This would mean that the second image source is found at $[2L_x - x_0, y_1]^T$.

24. An enclosed space with non-parallel walls can also be simulated with the ISM. In this case the image sources can be overlapped within each other, which is why the simplified form of shoebox shaped or rectangular rooms with parallel walls is assumed.

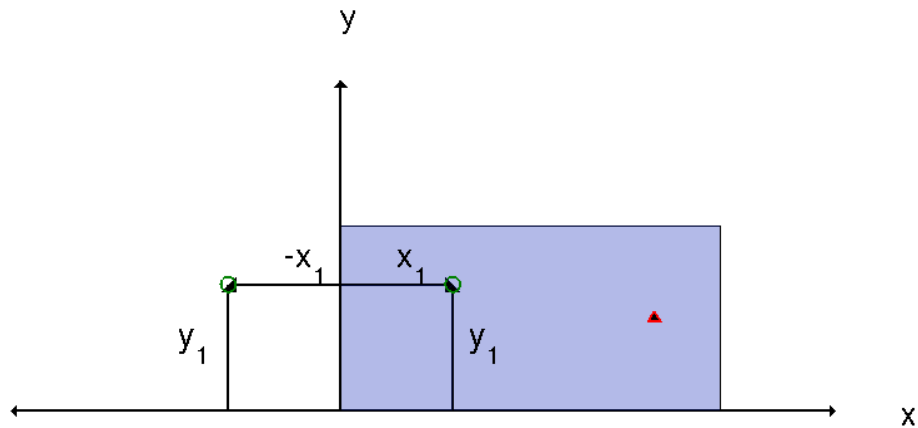


Figure 19: Principle of the ISM.

In doing so, the first condition has been disrupted by the second image source and to solve this problem the process has to be done again for both of them until infinitely many image sources are mirrored in free field. Strictly speaking, the ISM will only deliver the exact solution if the walls are completely rigid, meaning they reflect 100% of the incident wave's energy.²⁵ For all other cases the result will deviate because quantities such as the reflection coefficient or absorption parameter are defined for plane waves only, while the waves being radiated by the sources are assumed to be spherical. The good news is that the errors are negligible if $kr \gg 1$, which means that the distance between the receiver and all sources is large enough when compared to the wavelength λ . This condition is given in the far-field, which is why the directivities are normalized to their far-field approximation as presented in Section 3.5.2.

Once the image sources have been defined, their contribution at the receiver position can be computed without having to consider the original enclosure of the room anymore. The sound field at a point in space can be obtained by superposition of all contributions given that all sources radiate the same signal at the same time instant. Each contribution arrives at the receiver position with different amplitudes and delays. The latter depend on the reflection coefficient of the room's walls and on the direct path between them and the receiver position, respectively. The process concerning the weighting of the contributions can be written in a simplified form and when assuming that these are frequency independent as

$$h(t) = \sum_{l=1}^L a_l \delta(t - t_l). \quad (55)$$

²⁵ This is the case for a reflection coefficient $\Gamma = 1$. More information concerning this subject can be found in Section 4.1.

Eq. 55 can be understood as the sum of all reflexions generated by the primary source in a room, each of them with an individual amplitude a_l and an arrival time t_l . The continuous room impulse response can be won by filtering the coefficients with shifted sinc functions by t_l . The room impulse responses simulated with the ISM are illustrated in Section 4.2, while the discrete plot of Eq. 55 can be seen exemplarily in Fig. 22.

The ISM delivers a perfect solution, which answers at the same time to the modal solution, when summed over infinitely many image sources. In practice the infinite sum is approximated to a number of image sources $L \in \mathbb{N}^+$. For the RMM, only $(l_{max} + 1)^D$ modes are computed. As expected, the simulation will increase its accuracy in the frequency domain the more image sources are taken into consideration.

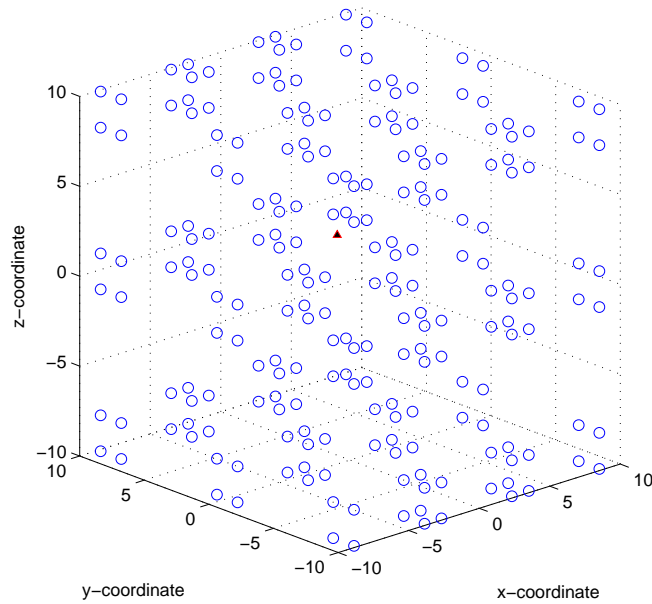


Figure 20: 3-D model of the ISM.

Fig. 20 illustrates the ISM with the receiver position represented as a red triangle and the image sources as blue circles. The number of image sources can be computed as $L = 8 \cdot b$. Here indicates b the number of blocks placed in each coordinate, where a block is defined as a periodic copy of the main block illustrated in Fig. 17. It contains a set of eight image sources in 3-D space. The main block with the receiver represents the starting point for the continuation process, from which blocks excluding the receiver can be layed around the main block at will. The advantage of this technique is the straightforward manner, in which the image model is built. Thus the number of blocks determines the number of room reflections considered. In this case, a total of 27 blocks were generated resulting in 216 image sources.

3.3.1 ISM In Its Time Domain Representation

The complete derivation of the image model can be found in [AB78]. Nevertheless, the fundamentals are presented here, with the intention of a better understanding of the method as well as of its equivalence to the RMM, see Section 3.2. The pressure wave of the image sources in free-field conditions is given, assuming they are point sources, by Eq. 15. Image sources are introduced in free field once the room's boundary conditions are taken into consideration. The image process, see Fig. 19, in which the first image source has been introduced, is formally written as:

$$P(\omega, \mathbf{r}, \mathbf{r}') = \left[\frac{e^{\frac{-i\omega}{c}r_0}}{4\pi r_0} + \frac{e^{\frac{-i\omega}{c}r_1}}{4\pi r_1} \right] e^{-i\omega t}. \quad (56)$$

Thereby is $\mathbf{r}^T = [x, y, z]^T$ the primary source and $\mathbf{r}'^T = [x', y', z']^T$ the receiver position. r_0 is the Euclidean distance between the receiver position and the primary source while r_1 is the one between the receiver and first image source.²⁶ Seven image sources can be defined out of the primary source in rectangular rooms delimited by six surfaces. Together they can be combined to form a block of eight sources like the one illustrated in Fig. 17, where the eight permutations become evident. They are defined as $\mathbf{r}_h = (x \pm x', y \pm y', z \pm z')$ and can be summarized into a matrix containing all of them as:

$$\mathbf{R}_h = \begin{bmatrix} \mathbf{r}_0 \\ \mathbf{r}_1 \\ \mathbf{r}_2 \\ \mathbf{r}_3 \\ \mathbf{r}_4 \\ \mathbf{r}_5 \\ \mathbf{r}_6 \\ \mathbf{r}_7 \end{bmatrix} = \begin{bmatrix} x - x' & y - y' & z - z' \\ x + x' & y - y' & z - z' \\ x - x' & y + y' & z - z' \\ x + x' & y + y' & z - z' \\ x - x' & y - y' & z + z' \\ x + x' & y - y' & z + z' \\ x - x' & y + y' & z + z' \\ x + x' & y + y' & z + z' \end{bmatrix}. \quad (57)$$

The sum over infinite many room modes $l = (l_x, l_y, l_z)$ and thus infinitely many periodic shifts of the primary source is given by

$$P(\omega, \mathbf{r}, \mathbf{r}') = \sum_{h=0}^7 \sum_{l=-\infty}^{\infty} \frac{e^{\frac{-i\omega}{c}\|\mathbf{r}_h - \mathbf{r}_l\|}}{4\pi \|\mathbf{r}_h - \mathbf{r}_l\|} e^{-i\omega t}, \quad (58)$$

where \mathbf{r}_l^T is again the spatial shift of the h^{th} source from the main block. The RIR or time-domain Green's function is obtained when applying a Fourier transform to the pressure frequency response. Hence Eq. 58 takes the following form:

²⁶ The Euclidean distance between two points in space is the length of the line segment connecting them. It is defined as $r_0 = \|\mathbf{r}_0\| = \|\mathbf{r} - \mathbf{r}'\| = \sqrt{(x - x')^2 + (y - y')^2 + (z - z')^2}$.

$$p(t, \mathbf{r}, \mathbf{r}') = \sum_{h=0}^{\infty} \sum_{l=-\infty}^{\infty} \frac{\delta(t - \frac{\|\mathbf{r}_h - \mathbf{r}_l\|}{c})}{4\pi \|\mathbf{r}_h - \mathbf{r}_l\|}. \quad (59)$$

Eq. 59 can be interpreted as a sum of infinitely many impulses arriving at the receiver position at all time instances $t = \frac{\|\mathbf{r}_h - \mathbf{r}_l\|}{c}$ with an amplitude which will fall relative to the distance $\|\mathbf{r}_h - \mathbf{r}_l\|$. The solution in this form yields the perfect solution when summed for $-\infty \rightarrow \infty$ many periodic blocks b in each dimension and thus infinitely many image sources. This result backs up the approach as introduced in Eq. 55, where the RIR was defined as a sum of impulses with different amplitudes a_l and arrival times t_l . An interpretation of Eq. 59 in space is also thinkable since there must be a point source radiating each of the impulses. Since all image sources are identical to each other, the primary source must merely be shifted in space in order to generate the desired sound field at the receiver position \mathbf{r}' . This can be written as a convolution of $G(\mathbf{r}, \mathbf{r}')$ with delta functions, i.e. a sum of shifted Green's functions, for $D = 3$ as:

$$\begin{aligned} G(\mathbf{r}, \mathbf{r}') &= G(\mathbf{r}, \mathbf{r}') \star \prod_{i=0}^{D-1} \sum_{l=-\infty}^{\infty} \frac{\delta(r_i \pm 2l_i L_i)}{2^D} \\ &= G(\mathbf{r}, \mathbf{r}') \star \sum_{l=-\infty}^{\infty} \frac{\delta(x \pm 2l_x L_x) \delta(y \pm 2l_y L_y) \delta(z \pm 2l_z L_z)}{8}, \end{aligned} \quad (60)$$

where (r_1, r_2, r_3) have been defined as (x, y, z) . Eq. 60 is equivalent to Eq. 54 from Section 3.2, where the analogy between both domains becomes evident. A multiplication in k-space with (k_x, k_y, k_z) is equivalent to a convolution in space by $(2l_x L_x, 2l_y L_y, 2l_z L_z)$.

3.4 Sparse Model Of A Room Response

As defined in [Org97], most acoustic measurements are carried out using omni-directional sound sources and microphones. The idea of measuring a directional sound source with a directional receiver is a very appealing idea since it represents reality in the sense of natural radiation and perception of sound waves as it actually happens. The way sound waves propagate away from a sound source will depend, in the general case, on the source's geometry, i.e. its corpus, its orientation and, most importantly, on the wavelength λ that determines the directionality of the radiated signal.²⁷ The same applies for the reception of sound, which is why the next step consists on computing room impulse responses with directivities.

²⁷ For a detailed review of the directionality of a sound source and its relationship between the signal's wavelength refer to [Goe06] or for the more general radiation patterns to [Wil99] et al.

This computation technique is taken from [MZR12], where a new approach is proposed in order to analyse spatial directions in room transfer functions with adjustable directivity patterns for both source and receiver. The advantage of such a measurement is the ability to excite a specific path of the room. These directional loudspeakers may have different characteristics while the focus here remains to stay with spherical loudspeaker arrays, which have been proven to be flexible in design, see [Zot09a].

The starting point for the next considerations is the representation of the room impulse response described by Eq. 55. As seen in Section 3.3, each reflection path is characterized by an amplitude a_l and an arrival time t_l . This representation is expanded by two Cartesian unit vectors $\boldsymbol{\theta}_{R_l}^T = [\cos \varphi_{R_l} \sin \vartheta_{R_l}, \sin \varphi_{R_l} \sin \vartheta_{R_l}, \cos \vartheta_{R_l}]^T$ and $\boldsymbol{\theta}_{S_l}^T = [\cos \varphi_{S_l} \sin \vartheta_{S_l}, \sin \varphi_{S_l} \sin \vartheta_{S_l}, \cos \vartheta_{S_l}]^T$ defined by the spherical angles. The idealized sparse model is composed of individual reflection paths. The directional impulse response from source to receiver is a sum over all these paths and can be written as

$$h(t, \boldsymbol{\theta}_{R_l}, \boldsymbol{\theta}_{S_l}) = \sum_l^L a_l \delta(t - t_l) \delta(\boldsymbol{\theta}_R - \boldsymbol{\theta}_{R_l}) \delta(\boldsymbol{\theta}_S - \boldsymbol{\theta}_{S_l}), \quad (61)$$

where the subscripts R_l and S_l describe the relative position between the l^{th} source and receiver position and vice versa.

3.4.1 Directivity Patterns For Source And Receiver

The directivities for source and receiver are defined by $g_R(\boldsymbol{\theta}_R)$ and $g_S(\boldsymbol{\theta}_S)$. These angular dependent functions are defined as

$$\begin{aligned} g_R(\boldsymbol{\theta}_R) &= \sum_{n'=0}^{N_R} \sum_{m'=-n'}^{n'} \gamma_{n'm'}^{(R)} Y_{n'}^{m'}(\boldsymbol{\theta}_R), \\ g_S(\boldsymbol{\theta}_S) &= \sum_{n=0}^{N_S} \sum_{m=-n}^n \gamma_{nm}^{(S)} Y_n^m(\boldsymbol{\theta}_S). \end{aligned} \quad (62)$$

where $Y_n^m(\boldsymbol{\theta})$ represent the spherical harmonics functions and (N_R, N_S) their maximal order. These orthonormal set of functions describe the spatial distribution of any function defined on a sphere and are favoured given their convenient transform identity $\int_{\mathbb{S}^2} Y_n^m(\boldsymbol{\theta}) \delta(\boldsymbol{\theta} - \boldsymbol{\theta}_n) d\boldsymbol{\theta} = Y_n^m(\boldsymbol{\theta}_n)$.

3.4.2 Directional Room Responses

In the beginning there is the room impulse response as function of time. The room impulse response $h(t)$ becomes also an angular-dependent function $h(\boldsymbol{\theta}_R, t, \boldsymbol{\theta}_S)$ as soon as a directivity is given to the source and to the receiver, respectively.

The room impulse response is obtained by means of integration over the spherical surface of the angular functions describing the directivities as:

$$h(t) = \int_{\mathbb{S}^2} \int_{\mathbb{S}^2} g_R(\boldsymbol{\theta}_R) h(\boldsymbol{\theta}_R, t, \boldsymbol{\theta}_S) g_S(\boldsymbol{\theta}_S) d\boldsymbol{\theta}_R d\boldsymbol{\theta}_S. \quad (63)$$

The directional RIR of the orders N_R and N_S is obtained when inserting Eq. 62.

$$\begin{aligned} h(t) &= \int_{\mathbb{S}^2} \int_{\mathbb{S}^2} \sum_{n',m'} \gamma_{n'm'}^{(R)} Y_{n'}^{m'}(\boldsymbol{\theta}_R) h(\boldsymbol{\theta}_R, t, \boldsymbol{\theta}_S) \sum_{n,m} \gamma_{nm}^{(S)} Y_n^m(\boldsymbol{\theta}_S) d\boldsymbol{\theta}_R d\boldsymbol{\theta}_S \\ &= \sum_{n,m,n',m'} \gamma_{n'm'}^{(R)} \left[\int_{\mathbb{S}^2} \int_{\mathbb{S}^2} Y_{n'}^{m'}(\boldsymbol{\theta}_R) \sum_l^L a_l \delta(t - t_l) \delta(\boldsymbol{\theta}_R - \boldsymbol{\theta}_{R_l}) \delta(\boldsymbol{\theta}_S - \boldsymbol{\theta}_{S_l}) \right. \\ &\quad \left. Y_{n'}^{m'}(\boldsymbol{\theta}_S) d\boldsymbol{\theta}_R d\boldsymbol{\theta}_S \right] \gamma_{nm}^{(S)} \\ &= \sum_{n,m,n',m'} \gamma_{n'm'}^{(R)} \sum_l^L a_l \delta(t - t_l) \left[\int_{\mathbb{S}^2} \int_{\mathbb{S}^2} Y_{n'}^{m'}(\boldsymbol{\theta}_R) \delta(\boldsymbol{\theta}_R - \boldsymbol{\theta}_{R_l}) \delta(\boldsymbol{\theta}_S - \boldsymbol{\theta}_{S_l}) \right. \\ &\quad \left. Y_{n'}^{m'}(\boldsymbol{\theta}_S) d\boldsymbol{\theta}_R d\boldsymbol{\theta}_S \right] \gamma_{nm}^{(S)} \end{aligned}$$

Making use of the transform identity of the spherical harmonics presented in Section 3.4.1 yields

$$\begin{aligned} h(t) &= \sum_{n,m,n',m'} \gamma_{n'm'}^{(R)} \sum_l^L a_l \delta(t - t_l) Y_{n'}^{m'}(\boldsymbol{\theta}_{R_l}) Y_n^m(\boldsymbol{\theta}_{S_l}) \gamma_{nm}^{(S)} \\ &= \sum_{n,m,n',m'} \gamma_{n'm'}^{(R)} h_{nm}^{n'm'}(t) \gamma_{nm}^{(S)}. \end{aligned} \quad (64)$$

The vectorized form of Eq. 64 with a sum over both pairs of indices reads as follows

$$\begin{aligned}
h(t) &= \left[\gamma_{n'm'}^{(R)} \right]_{n'm'}^T \left[h_{nm}^{n'm'}(t) \right]_{nm}^{n'm'} \left[\gamma_{nm}^{(S)} \right]_{nm} \\
&= \gamma_R^T \mathbf{H}(t) \gamma_S.
\end{aligned} \tag{65}$$

Thereby contains γ the directivity function describing the radiation and sensitivity patterns found at source and receiver positions, respectively.

3.5 Arbitrary Directivities

3.5.1 Spherical Harmonic Characteristics Employed For The ISM

The ISM can be used, as described in Section 3.3, for the simulation of room impulse responses or transfer functions between sources and receivers with an omni-directional directivity pattern. The principle remains the same when adding an angular dependent sound radiation and reception of sound. The L number of image sources will produce the sound field of a source with the directivity pattern of a spherical harmonic of the order and degree (n, m) when applying an individual angular dependency or spatial weight to all of them. The new source's field is simulated by evaluating the chosen radiation pattern at all relative angles between image source and receiver. Similarly, a receiver with a certain sensitivity pattern (n', m') can be simulated by evaluating the sensitivity function at all inverse angles. The latter are measured for all image sources from the receiver's point of view.

It is enough to mirror the source adequately, i.e., by taking into consideration its orientation and angle dependency, in order to compute the RIR for a source with directivity pattern. Contrarily, the receiver does not have to be mirrored. For instance a receiver with the directivity pattern of a cardioid microphone can be simulated by applying a directivity pattern like the one depicted in Fig. 9. The result is an additional weight to the contribution of each source depending on the incident angle at the receiver position. This is done by means of superposition as $h_{n'm'}^{nm}(t) = h_{00}^{00}(t) + h_{11}^{00}(t)$ if the source features no angle dependency.

The notation as presented in Section 2.3.4 was used for the implementation of all simulations of room responses done with the ISM. Thereby L represents the number of sources considered, see Eq. 55, and θ_l the spherical coordinate vector of the l^{th} source. The directivities describing the receiver's sensitivity are stored in $\mathbf{Y}(\theta_R)$ and the ones describing the radiation pattern of the source in $\mathbf{Y}(\theta_S)$.

The latter are described by the Y_n^m and $Y_{n'}^{m'}$ spherical harmonic coefficients for source

and receiver, respectively. The result is a $(N_R + 1)^2$ by $(N_S + 1)^2$ by length t of the signal matrix $\mathbf{H}_Y(t)$:

$$\mathbf{H}_Y(t) = \begin{bmatrix} h_{0,0}^{0,0}(t) & h_{0,0}^{1,-1}(t) & h_{0,0}^{1,0}(t) & h_{0,0}^{1,1}(t) & \dots & h_{0,0}^{N_S,N_S}(t) \\ h_{1,-1}^{0,0}(t) & h_{1,-1}^{1,-1}(t) & h_{1,-1}^{1,0}(t) & h_{1,-1}^{1,1}(t) & \dots & h_{1,-1}^{N_S,N_S}(t) \\ h_{1,0}^{0,0}(t) & h_{1,0}^{1,-1}(t) & h_{1,0}^{1,0}(t) & h_{1,0}^{1,1}(t) & \dots & h_{1,0}^{N_S,N_S}(t) \\ h_{1,1}^{0,0}(t) & h_{1,1}^{1,-1}(t) & h_{1,1}^{1,0}(t) & h_{1,1}^{1,1}(t) & \dots & h_{1,1}^{N_S,N_S}(t) \\ \vdots & \vdots & \vdots & \vdots & \ddots & \vdots \\ h_{N_R,N_R}^{0,0}(t) & h_{N_R,N_R}^{1,-1}(t) & h_{N_R,N_R}^{1,0}(t) & h_{N_R,N_R}^{1,1}(t) & \dots & h_{N_R,N_R}^{N_S,N_S}(t) \end{bmatrix}, \quad (66)$$

where N_R represents the maximal order of spherical harmonics coefficients for the receiver and N_S for the source accordingly. Eq. 66 represents a finite resolution MIMO-matrix²⁸. The advantage of the spherical decomposition representation of $h_{n'm'}^{nm}(t)$ lies in the fact that it can easily be modeled as well as measured by means of spherical loudspeaker and microphone arrays. The room response in its $\mathbf{H}_Y(t)$ form is a matrix that contains individual room responses between sources and receivers with directivity patterns described by spherical harmonics of the orders (n, n') and degree (m, m') . These can be superimposed at will in order to simulate room responses of arbitrary directivities.

3.5.2 Spherical Harmonics In The Far-Field

The far-field approximation of a point source's field on the basis of its spherical harmonics coefficients reads as

$$\lim_{r \rightarrow \infty} p(r, \varphi, \vartheta) = \frac{e^{-ikr}}{r} D(\varphi, \vartheta). \quad (67)$$

Thereby represents $D(\varphi, \vartheta)$ the far-field directivity pattern. The latter is obtained from Eq. 67 and the far-field approximation of the the *Hankel* functions $h_n(kr)$ the n^{th} order. They constitute the radius-dependent solution to the 3-D wave equation. The Hankel functions of the 1st and 2nd kind are computed via the *spherical Bessel* functions $j_n(x)$ and $y_n(x)$ as follows:

28. Multiple-input and multiple-output matrix containing the room responses between all radiation patterns $(N_S + 1)^2$ and all sensitivity patterns $(N_R + 1)^2$.

$$\begin{aligned}
h_n^{(1)} &= j_n(x) + iy_n(x), \\
h_n^{(2)} &= j_n(x) - iy_n(x).
\end{aligned} \tag{68}$$

Further, the useful relationship $h_n^{(2)} = [h_n^{(1)}]^*$ is derived from these identities. For a detailed description of the angular- and radius-dependent solution of the wave equation in the spherical coordinate system refer to [Wil99] et al. The expressions in terms of trigonometric functions for the spherical Bessel functions are given by

$$\begin{aligned}
j_n(x) &= (-x)^n \left(\frac{1}{x} \frac{d}{dx} \right)^n \frac{\sin(x)}{x} \quad \text{and} \\
y_n(x) &= -(-x)^n \left(\frac{1}{x} \frac{d}{dx} \right)^n \frac{\cos(x)}{x}.
\end{aligned} \tag{69}$$

The far-field directivity pattern of the spherical harmonics can be found with the far-field approximation of the Hankel functions given by

$$\lim_{r \rightarrow \infty} h_n^{(2)}(kr) = \lim_{r \rightarrow \infty} [h_n^{(1)}(kr)]^* = (-i)^{n+1} \frac{e^{-ikr}}{kr}. \tag{70}$$

The far-field directivity corresponding to the spherical basis solution $h_n^{(2)}(kr)Y_n^m(\varphi, \vartheta)$ hereby yields:

$$\begin{aligned}
\tilde{D}(\varphi, \vartheta) &= \lim_{r \rightarrow \infty} \left[r e^{ikr} h_n^{(2)}(kr) \right] Y_n^m(\varphi, \vartheta) \\
&= \frac{(-i)^{n+1}}{k} \cdot Y_n^m(\varphi, \vartheta).
\end{aligned} \tag{71}$$

Obviously, except for the normalization term $\frac{(-i)^{n+1}}{k}$, the physical solution $h_n^{(2)}(kr)Y_n^m(\varphi, \vartheta)$ yields the same angular pattern as Eq. 67. To simplify things, near fields were neglected and this work only employs Eq. 67 with the ISM.

3.5.3 Multipole Characteristics For The RMM

The room reponse in shoebox shaped rooms with rigid walls can be computed with the RMM via Eq. 49. This solution is valid for sources and receivers with omni-directional

directivities only. The next step consists in upgrading the RMM in order to simulate room responses of arbitrary directivities. These will be generated by means of the multipole characteristics presented in Section 2.3.1. This choice is backed up given the form of the Green's function and its relationship with the monopole characteristic, from which is possible to derive higher order multipole characteristics offering a higher spatial resolution.

As a result, the simulated sound field will feature an angle-dependent distribution in 3-D space. Multipole characteristics will be computed by derivating $G(\mathbf{r}, t)$ and thus $\psi_l(\mathbf{r})$ and $\psi_l(\mathbf{r}_0)$ with respect to the coordinate axes. Once the derivatives have been made available, they can be superimposed resulting in direction-dependent radiation and pickup patterns. The room responses can, if desired, undergo a conversion into the spherical harmonic domain by means of the \mathbf{C} -matrix in order to better evaluate the results at a later stage.²⁹ The conversion procedure is treated in Section 4.3.1 as well as the analysis method used for the room reflections.

Formal Calculation Of Room Responses

The objective is to compute and store room responses between sources and receivers with as many different directivity patterns, i.e. for high order multipole characteristics, in order to facilitate a great flexibility when designing room responses of arbitrary directivities by means of superposition. The multipole directivities shown in Fig. 4 can be applied to a source by deriving $\psi_l(\mathbf{r}_0)$ (l, m, n) times with respect to the (x, y, z) coordinate axes. This also applies for the receiver, whose directivities are produced by deriving $\psi_l(\mathbf{r})$, respectively.

Formally, the Green's function for rectangular rooms consists of the space-coordinate- and the time-coordinate-dependent parts. As a result, the expressions in the sum can be derivated individually. It can be written as:

$$G(\mathbf{r}, \mathbf{r}_0, t) = \sum^L \psi(\mathbf{r})\psi(\mathbf{r}_0) \cdot g(t). \quad (72)$$

The derivatives of Eq. 72 with respect to the coordinate axes are carried out in a straightforward manner. The next considerations are done for the x-axis only. The goal is thus to present the derivation process, that when done for the y- and z-axis too, result in higher order multipole characteristics. These can be freely applied to the point-to-point solution. l derivatives of $\psi(\mathbf{r}) = \psi(x, y, z)$ with respect to the x-coordinate are carried out as:

²⁹ The conversion takes place with the c -coefficients as discussed in Section 2.3.5.

$$\begin{aligned}
\frac{\partial^l \psi(\mathbf{r})}{\partial x^l} &= \frac{\partial^l}{\partial x^l} \cos(k_x x) \cos(k_y y) \cos(k_z z) \\
&= (k_x)^l \left[\cos(k_x x) \cos\left(\frac{\pi}{2} l\right) + \sin(k_x x) \sin\left(\frac{\pi}{2} l\right) (-1)^l \right] \cdot \cos(k_y y) \cos(k_z z).
\end{aligned} \tag{73}$$

The derivatives are done (l, m, n) times with respect to (x, y, z) and result in a multipole characteristic of the order $l + m + n$. The latter is obtained when evaluating Eq. 73 for each of the cosine terms separately and thus for each of the derivative orders. The multiple derivatives of $\psi(\mathbf{r})$ are summarized as

$$\frac{\partial^l}{\partial x^l} \frac{\partial^m}{\partial y^m} \frac{\partial^n}{\partial z^n} G(\mathbf{r}, t) = \sum^L \psi(x, y, z) \psi(x_0, y_0, z_0) g(t), \tag{74}$$

with the multipole-based directivity defined as $\psi(x, y, z) = \psi_x(x)\psi_y(y)\psi_z(z)$ and $\psi_x(x) = (k_x)^l \left[\cos(k_x x) \cos\left(\frac{\pi}{2} l\right) + \sin(k_x x) \sin\left(\frac{\pi}{2} l\right) (-1)^l \right]$. Multipole characteristics as written in Eq. 74, are still frequency-dependent in the far-field, proportionally to $\frac{1}{(i\omega)^{l+m+n}}$. Normalization in order to obtain frequency-independent multipole characteristics is discussed in the next section.

3.5.4 Far-Field Normalization Of The Multipole Characteristics

The derivatives of the multipole characteristics as done in Section 3.5.3 result in a frequency dependent weighting of the Green's function. This effect has to be compensated in order to remove unwanted effects concerning the multipole's order $l + m + n$ and thus the number of derivatives. The relationship between higher order multipoles and the monopole characteristic is known from Section 2.3.1, where the advantage of the representation in Eq. 2.3.1 becomes clear.

This frequency weighting takes place when the Green's function is derivated and as a consequence, multiplied with a factor proportional to k . With the purpose of analyzing the weighting, a source is assumed to be along the z-axis meaning that $x = y = 0$. The Green's function can be written as

$$G(\mathbf{r}) = \frac{e^{-ik \cos(\vartheta)z}}{z}. \tag{75}$$

Now a dipole can be created by deriving Eq. 75 with respect to the z-axis. The result is, from a proportional point of view, $\frac{\partial}{\partial z} G(\mathbf{r}) \propto -ik \cos \vartheta G(\mathbf{r})$. The angular portion

$\cos \vartheta$ constitutes the angular dependency of the function while the factor $-ik$ represents the unwanted weighting, which is stands in direct relationship to the derivatives. This can be understood to be, based on Eq. 49, the number of derivatives $l + m + n$. The normalization of the unwanted factor $(-ik)^{l+m+n}$ is removed, as an enhancement of Eq. 2.3.1, by a multiplication with the factor $\frac{1}{(-ik)^{l+m+n}}$. This constitutes the far-field normalization of the multipoles obtained by means of spatial derivatives.

$$M_{lmn}(\mathbf{r}) = \frac{1}{(-ik)^{l+m+n}} \frac{\partial^l}{\partial x^l} \frac{\partial^m}{\partial y^m} \frac{\partial^n}{\partial z^n} G(\mathbf{r}, t). \quad (76)$$

The normalization factor can be decomposed in an analytical manner and written with the wavenumber's identity as $\frac{1}{-ik} = \frac{-c}{i\omega}$. The normalization in this form enables a practical representation given the known relationship between derivatives and the Fourier transform.³⁰ Therefrom it can be concluded that a multiplication with $\frac{1}{-i\omega}$ is equal to an integration of the Green's function as $(-c) \int dt$.

The Green's function as written in Eq. 72 has been decomposed in a sum over the modes indices (l_x, l_y, l_z) and a time-dependent part. The advantage of this representation can be explained by the normalization factor in form of an integral of $G(\mathbf{r}, t)$, which is applied to $g(t)$ only. The free-field solution given by Eq. 76 takes the following form

$$M_{lmn}(\mathbf{r}, t) = (-c)^{l+m+n} \frac{\partial^l}{\partial x^l} \frac{\partial^m}{\partial y^m} \frac{\partial^n}{\partial z^n} \underbrace{\int \cdots \int}_{l+m+n} G(\mathbf{r}, t) (dt)^{l+m+n} \quad (77)$$

and is understood to be the normalized solution under free-field conditions. The Green's function as computed for rectangular rooms and thus a finite number of modes L reads as:

$$M_{lmn}(\mathbf{r}, t) = (-c)^{l+m+n} \frac{\partial^l}{\partial x^l} \frac{\partial^m}{\partial y^m} \frac{\partial^n}{\partial z^n} \sum^L g(\mathbf{r}) \underbrace{\int \cdots \int}_{l+m+n} g(t) (dt)^{l+m+n} \quad (78)$$

Eq. 78 is the multipole's identity as used for the simulations done in Section 4. The integral with respect to time is carried out assuring causality as follows:

$$\underbrace{\int \cdots \int}_{l+m+n} g(t) (dt)^{l+m+n} = \underbrace{\int \cdots \int}_{l+m+n} \frac{\sin(\omega_l t)}{\omega_l} (dt)^{l+m+n} =$$

30. The Fourier identity of a derivative is given by $(i\omega)^n \iff \frac{\partial^n x(t)}{\partial t^n}$.

$$= u(t) \frac{\left[\cos(\omega t) \sin\left(\frac{\pi(l+m+n)}{2}\right) (-1)^{l+m+n} + \sin(\omega t) \cos\left(\frac{\pi(l+m+n)}{2}\right) \right]}{\omega^{l+m+n+1}}. \quad (79)$$

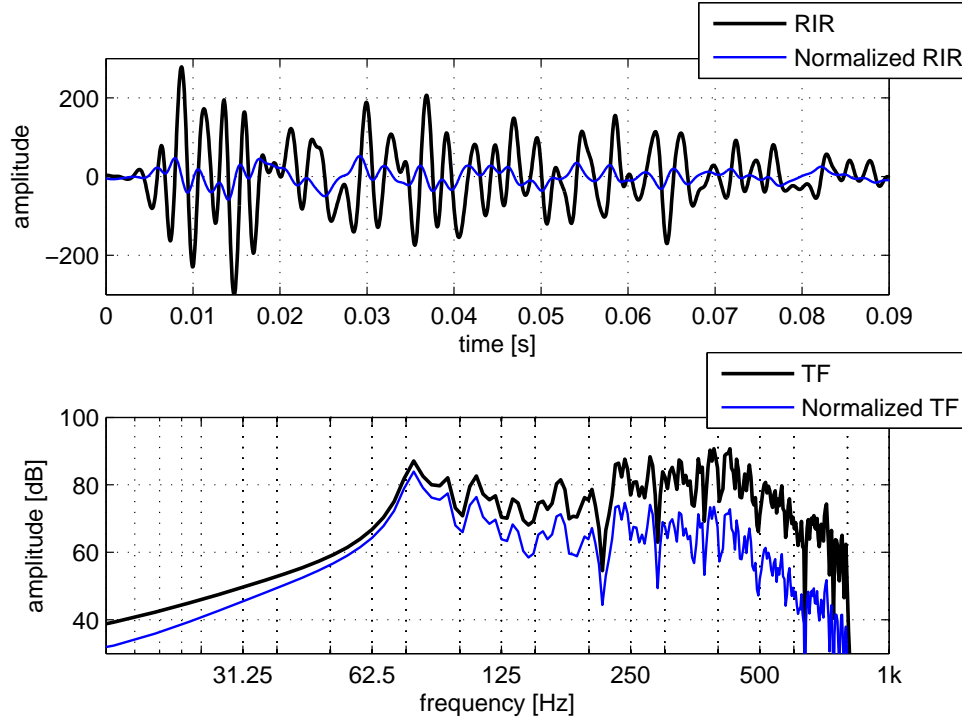


Figure 21: Far-field normalization of the multipole derivatives.

The effect of the far-field normalization is illustrated in Fig. 21. Here the room impulse response has been computed for a monopole receiver and a dipole source oriented in the z direction. The black curves in Fig. 21 are the time domain signal and its Fourier domain representation. The simulation was done with a frequency barrier of 800 Hz and a total of 1957 modes.

The wrongly normalized time domain signal of the dipole is considerably louder when comparing it to the blue curve (monopole). The latter is the normalized version, for which the frequency-proportional term has been compensated. The term is proportional to the number of derivatives as $\frac{1}{(-ik)^{l+m+n}}$ and thus to ω . The accentuation of the higher frequency band can be clearly identified in the frequency response diagram as a high-pass characteristic. Therefore, the far-field normalization is absolutely necessary when computing larger number of room modes and especially when directivities are applied through high order derivatives. This effect is also discussed in Section 4, where the direct influence of the modal frequencies is studied.

3.5.5 Matrix Notation Of The RMM With Multipole Characteristics

Now it has become possible to simulate room impulse responses with directivity on the basis of modes outlined by $h_{l'm'n'}^{lmn}(t)$, where the indices (l, m, n) give the multipole characteristic of the source and (l', m', n') the one from the receiver. From Section 2.3.3 it is known that a defined number of multipole characteristics will arise for a maximal multipole order N_{MP} . The computation of the room responses is carried out for all radiating patterns applied to the source and all pickup patterns applied to the receiver. Thus all possible combinations are computed and stored in the 3-D matrix

$$\mathbf{H}_M(t) = \begin{bmatrix} h_{000}^{000}(t) & h_{000}^{100}(t) & h_{000}^{010}(t) & h_{000}^{001}(t) & \dots & h_{000}^{333}(t) \\ h_{100}^{000}(t) & h_{100}^{100}(t) & h_{100}^{010}(t) & h_{100}^{001}(t) & \dots & h_{100}^{333}(t) \\ h_{010}^{000}(t) & h_{010}^{100}(t) & h_{010}^{010}(t) & h_{010}^{001}(t) & \dots & h_{010}^{333}(t) \\ h_{001}^{000}(t) & h_{001}^{100}(t) & h_{001}^{010}(t) & h_{001}^{001}(t) & \dots & h_{001}^{333}(t) \\ \vdots & \vdots & \vdots & \vdots & \ddots & \vdots \\ h_{333}^{000}(t) & h_{333}^{100}(t) & h_{333}^{010}(t) & h_{333}^{001}(t) & \dots & h_{333}^{333}(t) \end{bmatrix}. \quad (80)$$

In Eq. 80 the maximal multipole order for the source $N_{MP}^{(S)}$ and for the receiver $N_{MP}^{(R)}$ were exemplarily set to be 3. The higher the order, the more derivatives are needed and thus the more computation capacity is necessary. The fact that multipoles form an over-determined basis points out the redundancy of the directivities in this form and thus from the data itself. Therefore another representation of $\mathbf{H}_M(t)$ is desired.

$\mathbf{H}_M(t)$ does not profit from the benefits of the spherical harmonic representation as $\mathbf{H}_Y(t)$ does. Therefore a conversion by means of the \mathbf{C} -matrix from a multipole- into a spherical-harmonic based representation is advantageous. Each of the directional room responses $h_{l'm'n'}^{lmn}(t)$ ³¹ with multipole characteristics can be transformed into its spherical-harmonic based equivalent $h_{n'm'}^{nm}(t)$. The orders $N_{SH}^{(S)}$ and $N_{SH}^{(R)}$ can be determined freely because the \mathbf{C} -matrix is computed precisely with the dimensions corresponding to the maximal orders. The latter will also determine the size of $\mathbf{H}_Y(t)$, which is a $(N_{SH}^{(R)} + 1)^2$ times $(N_{SH}^{(S)} + 1)^2$ matrix. The different dimensions can be explained by the fact that multipoles are not orthogonal to each other and as a consequence form an overdetermined set of functions. This becomes evident through analysis of the 2nd order multipoles or quadrupoles, which when combined produce the monopole characteristic.³²

31. As discussed in Section 3.4.2, the five dimensions refer to the fact that h is a function of θ_R , t and θ_S referred as a directional room impulse response.

32. $Mp_{2,0,0} + Mp_{0,2,0} + Mp_{0,0,2} = Mp_{0,0,0}$. More to this subject can be found in [Zot14b].

The transformation of the $\frac{(N_{MP}^{(R)}+1)(N_{MP}^{(R)}+2)(N_{MP}^{(R)}+3)}{6}$ times $\frac{(N_{MP}^{(S)}+1)(N_{MP}^{(S)}+2)(N_{MP}^{(S)}+3)}{6}$ matrix $\mathbf{H}_M(t)$ is done for all source radiation patterns being received with all pickup patterns. The conversion reads in its matrix notation as:

$$\mathbf{H}_Y(t) = \mathbf{C}_{(R)} \mathbf{H}_M(t) \mathbf{C}_{(S)}^T, \quad (81)$$

where $\mathbf{C}_{(R)}$ is the conversion matrix from the receiver side and $\mathbf{C}_{(S)}$ the one from the source side, respectively. In the same way as before, the subscript groups (l, m, n) and (l', m', n') refer to the derivatives in (x, y, z) while (n, n') and (m, m') indicate the spherical harmonic order and degree, respectively.

It is important to remember that the solutions obtained with the RMM will ultimately be transformed to a spherical-harmonic based representation in order to analyze its spatial properties in a more practical manner. Therefore, the conversion by means of the \mathbf{C} - matrix of the far-field multipole solution will correlate to the far-field solution obtained on the basis of spherical harmonics in Section 3.5.2. The whole approach and the benefits of this conversion is treated in Section 4.3.1.

4 Room Response Simulations With Directivities And Comparison

4.1 Absorbing Walls

As already stated throughout Section 3, the results are valid under the assumption of totally reflecting walls and that no energy is lost in the propagation fluid. In order to obtain results that are valid in an environment where a heat exchange takes place and absorbing materials are present, the reflection coefficient has to be taken into account. The latter is widely used when considering wave propagation in a medium containing discontinuities. Such a discontinuity is for a example a variation of the medium's density, e.g. the transition of a wave propagating in air which impacts at a wall's surface.

4.1.1 Reflection Coefficient

The RIR can be expanded by introducing the reflection coefficient for the delimiting surfaces of the room. This coefficient indicates in which manner the medium reacts to the incident wave and is defined as follows

$$\Gamma = \frac{Z_2 - Z_1}{Z_2 + Z_1}, \quad (82)$$

where Z stands for the characteristic acoustic impedance³³ of a medium. In other words, it is the ratio of the amplitude of the reflected wave to the amplitude of the incident wave. Its value range is $\Gamma \in (-1, 1)$, with three extreme cases. These are

$$\rho = \begin{cases} 1 & \rightarrow \text{the wave is totally reflected and no phase shift takes place,} \\ 0 & \rightarrow \text{the wave is completely asborbed,} \\ -1 & \rightarrow \text{the wave is totally reflecedtd and receives a } 180^\circ \text{ phase shift.} \end{cases}$$

For more information concerning the reflection coefficient and the acoutic impedance as well as other acoustic factors and parameters refer to [KFCS00, Goe06].

Realistic results can be obtained by chosing a reflection coefficient for all six surfaces of the rectangular room under consideration. For the ISM it means that each contribution will be weighted in an individual manner, depending on the path between image source and receiver. Thus the weighting factor is determined by the *image walls*³⁴ the sound

33. The acoustic impedance of a medium is defined as $Z_0 = \rho_0 c_0$, where the density ρ_0 and acoustic velocity c_0 are speciefic for that medium precisely.

34. The image walls are used for the image process of the primary source. They can be seen in Fig. 6, where they have been ploted to better illstrute the method's notion.

ray crosses before arriving at the receiver position. The ray's amplitude is being weighted as the ray travels in space and through the image walls. Thereby represents the path between image source and receiver a real reflection of the ray in the room's surfaces.

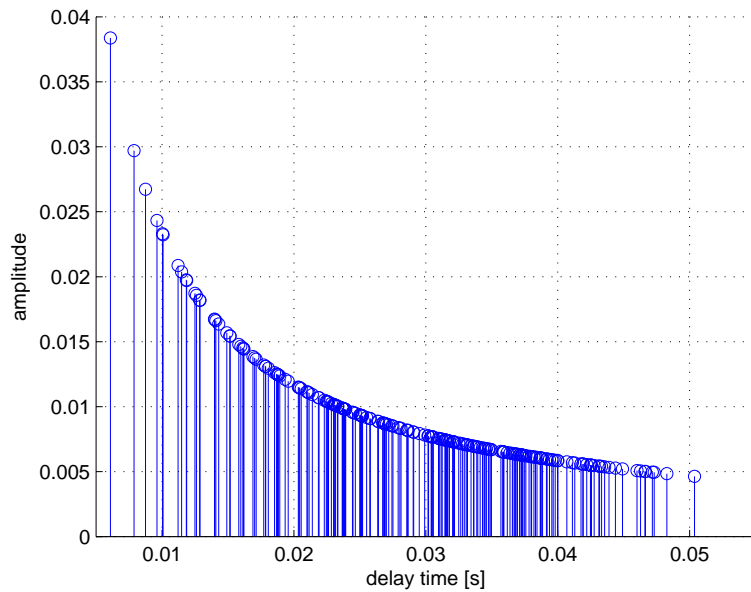


Figure 22: Contributions of the image sources for totally reflecting walls.

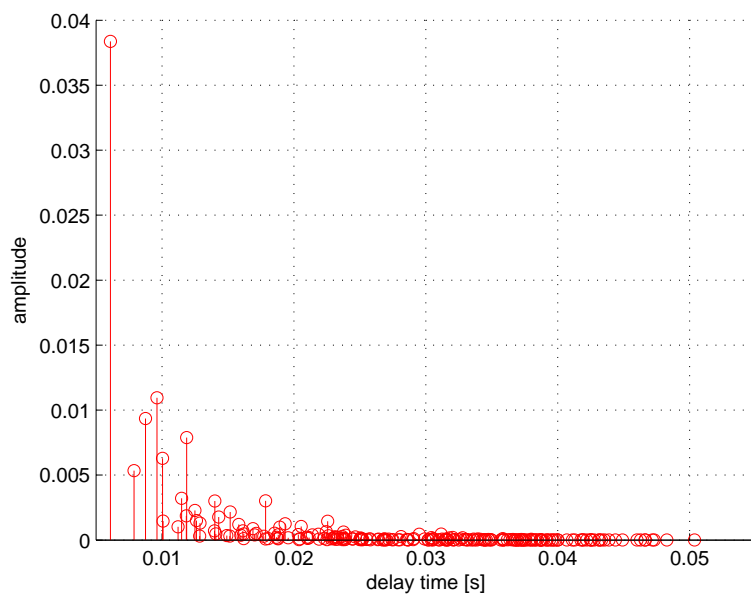


Figure 23: Contributions of the image sources for a set of reflection coefficients.

The result of applying reflection coefficients to the ISM is exemplarily illustrated in Fig. 22 and Fig. 23. The first RIR was computed for totally reflecting walls, meaning no weighting was applied to the individual contributions. The influence absorptive materials have, can be seen in Fig. 23, where non-zero positive values smaller than one were chosen for the reflection coefficient vector. The latter is defined as $\boldsymbol{\rho}^T = [\rho_{x1}, \rho_{x2}, \rho_{y1}, \rho_{y2}, \rho_{z1}, \rho_{z2}]^T$ and constitutes the weights applied to each of the six surfaces forming the rectangular room.

4.1.2 Auralization Of Room Modifications

An auralization algorithm enables the simulation and adjustment of the room's reverberation time for the simulated room transfer function. The goal of such algorithms is to simulate different reverberation times by modifying the early reflections of a room impulse response. These reflections can be seen exemplarily in Fig. 18, where the vicinity to the receiver position can be appreciated. They typically have a delay of about $5 - 100ms$ after the direct sound has arrived at the receiver position. More information concerning the importance of the early reflections of room impulse responses and their modification can be found in [JW03, EWL05, SM07] et al.

The concept of auralization of room modifications is inspired from [PSJ13] and consists on applying an exponential attenuation to the room impulse response simulated with the RMM. In this article the envelope of a RIR is applied to other transfer functions. Consequently, the room impulse response's reverberation time T_{60} ³⁵ and decay can be modified. This method has been evaluated and is supported by a series of psychoacoustical experiments from which was concluded that the algorithm delivers realistic results. It has been conceived with the goal of auralization of room modifications in order to evaluate them before actually executing them.

The method is carried out first by determining the arrival time of the direct sound t_{dir} . Every reflection that arrives after $t_{dir} + 5ms$ will be used to form the RIR's envelope. This signal is then decomposed in several frequency bands where typically, a *constant - Q* filterbank like the $\frac{1}{3}$ - *octave* filterbank is employed. This can be explained by the auditory filterbanks³⁶ which also possess a *constant Q - factor*. The latter is defined for typical auditory filterbanks as

$$Q = \frac{f_c}{\Delta f} \stackrel{!}{=} \text{const.} \quad (83)$$

Hereby denotes f_c the centre frequency at which the band-pass filter is placed and Δf

35. Time required for average sound in a room to decrease by $-60dB$ after the source has stopped radiating sound.

36. Non-uniform filterbanks designed to imitate the frequency resolution of human hearing.

its bandwidth. Once the reference RIR has been decomposed in frequency bands, the multiple envelopes can be computed and applied in order to change the desired signal. This corresponds to a modification of the RIR's energy in each frequency band separately. The new signal is obtained by adding all modified frequency bands. The classical structure of a RIR is illustrated in Fig. 24, where the direct sound, early reflections and diffuse field are clearly identified.

The result are two room impulse responses computed differently with the same acoustical properties, i.e. with the same reflection coefficients and thus the same reverberation time T_{60} . The latter in its form after Sabine is defined as

$$T_{60} = 0.163 \frac{s}{m} \cdot \frac{V}{\alpha A}, \quad (84)$$

where V is the room's volume, A is the area of all surfaces enclosing the volume and α is the total absorption parameter found in the room. For other definitions of the reverberation time refer to [Goe06, KFCS00].

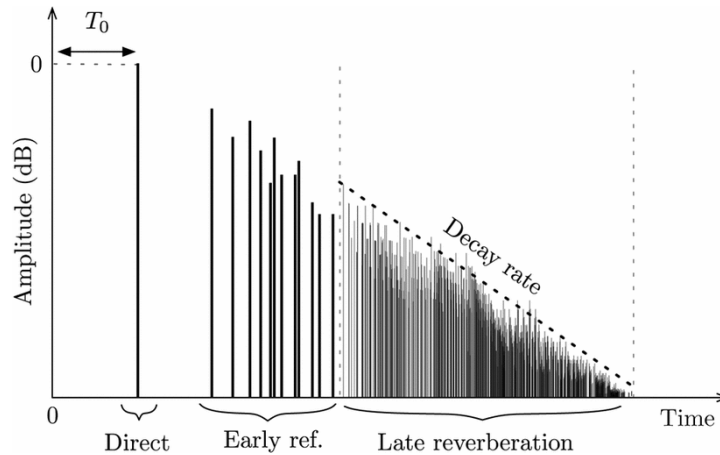


Figure 24: Structure of a room impulse response.

The goal for this study would be to adapt the room impulse response valid for totally reflecting walls obtained by means of the RMM in order to meet the characteristics of room transfer functions simulated with reflection coefficients $\rho \neq \pm 1$. Some of the advantages of this method are the ability of reshaping the RIR's envelope while maintaining its fine structure as well as its simple implementation. The main reason why a change in the signal's envelope is favoured are the good results that are backed up by Pörschmann in [PSJ13].

The implementation of the attenuation is done in form of an exponential function as:

$$d(\epsilon, t) = e^{-\epsilon t}. \quad (85)$$

Eq. 85 can be solved in this form with the definition of the reverberation time. The attenuation ϵ can be found for the corresponding T_{60} by comparison of the amplitude decrease of $10^{-3 \frac{t}{T_{60}}} \stackrel{!}{=} d(\epsilon, t)$. Expanding this equation with e^{\ln} yields

$$\begin{aligned} e^{\ln(10)^{-3 \frac{t}{T_{60}}}} &= e^{\ln(e^{-\epsilon t})} \\ e^{-\ln(10) \cdot 3 \frac{t}{T_{60}}} &= e^{-\epsilon t} \\ -\ln(10) \cdot 3 \frac{t}{T_{60}} &= -\epsilon t \\ \epsilon &= \frac{3 \ln(10)}{T_{60}}. \end{aligned} \quad (86)$$

By choosing a value for T_{60} it becomes possible to solve for an attenuation factor. This one was chosen to be $400ms$ for the simulations presented in Section 4.2. From this choice it follows that $\epsilon \approx 14$. With this factor well-defined, it became possible to simulate room impulse responses with the RMM.

An equal attenuation was achieved for the ISM by finding the corresponding reflection coefficients. For this, the attenuation was chosen to be equal in every coordinate. This means that both boundary conditions in (x, y, z) feature a reflection coefficient (ρ_x, ρ_y, ρ_z) . This approach supposes an attenuation proportional to the distance covered by each reflection and thus to the number of times the sound ray crosses the image walls. The next considerations are done for the x-coordinate. The number of times a sound ray is reflected can be determined with room dimensions and speed of sound. The contribution from the l^{th} image source will be weighted l times. The reflection coefficient reads $\rho_x^l = \rho_x^{\frac{x}{L_x}}$. Given that the distance $x = c \cdot t$, the exponential weighting can be written as $\rho_x^{\frac{ct}{L_x}} \stackrel{!}{=} e^{-\epsilon t}$. The latter equation can be solved to find the individual reflection coefficient of every room dimension as:

$$\begin{aligned} e^{\ln(\rho_x)^{\frac{ct}{L_x}}} &= e^{\ln(e^{-\epsilon t})} \\ e^{\frac{ct}{L_x} \cdot \ln(\rho_x)} &= e^{-\epsilon t} \\ \frac{ct}{L_x} \cdot \ln(\rho_x) &= -\epsilon t \\ \rho_x &= e^{\frac{-\epsilon L_x}{c}}. \end{aligned} \quad (87)$$

4.2 Room Impulse Responses And Room Transfer Functions

Next, the results of both methods are presented. The values obtained for $\epsilon = 14$ follow from Eq. 86 and from the choice for the room dimensions $(L_x, L_y, L_z) = (4.5, 3.1, 2.2)$. As a result the reflection coefficients are $\boldsymbol{\rho}^T = [0.81, 0.81, 0.87, 0.87, 0.9, 0.9]^T$. Such reflections coefficients represent very little absorption by the room walls and therefore a long reverberation time $T_{60} \approx 400ms$ for a rather small environment.

4.2.1 Simulations With The ISM

The next simulations were done using the ISM and by varying the number of image sources. The number of these is determined by the number of periodic blocks placed around the receiver position. Greater delays are visible in Fig. 26, where number of image sources has been increased considerably. In their time-domain representation there are no further effects worth mentioning. The Fourier representations reveal a finer structure given for the transfer functions computed with a greater number of image sources. This seems to be the case for both the simulations done without directivity patterns, as for the case where both source and receiver feature a directional radiation and sensitivity pattern.

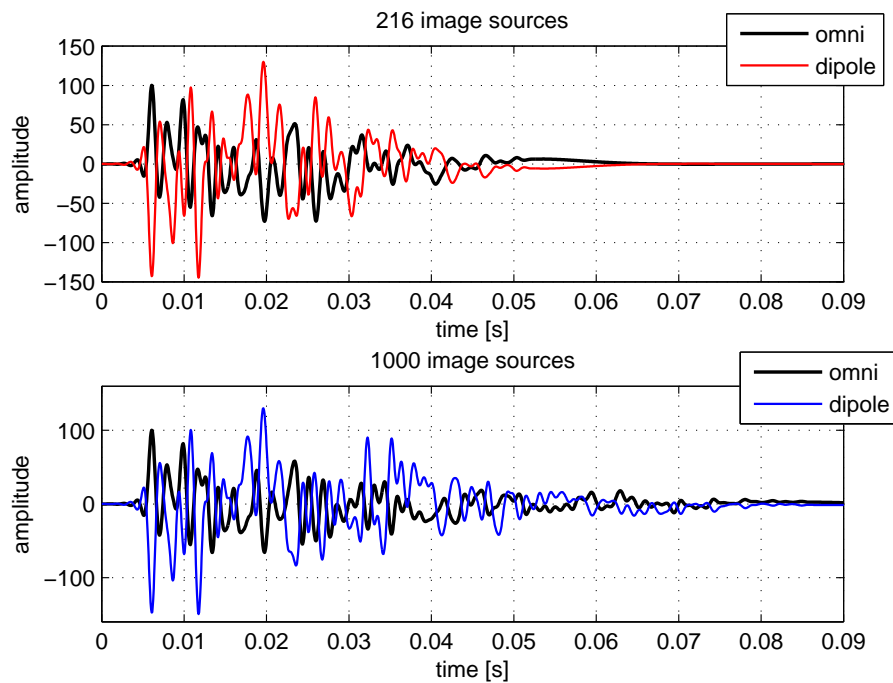


Figure 25: RIR computed with 216 (above) and 1000 (bellow) image sources.

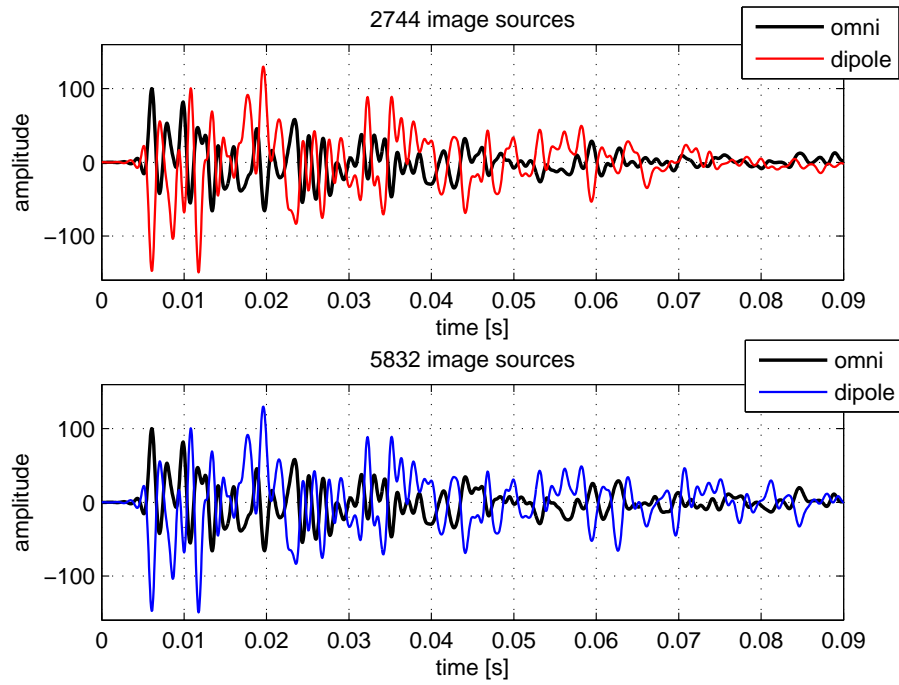


Figure 26: RIR computed with 2744 (above) and 5832 (bellow) image sources.

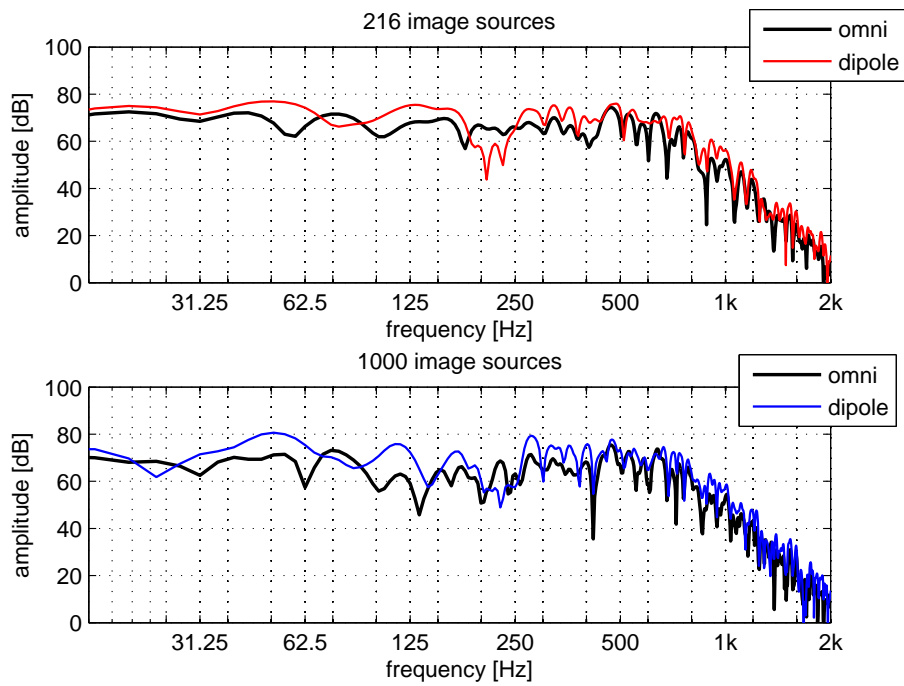


Figure 27: Fourier representation of the curves in Fig. 25.

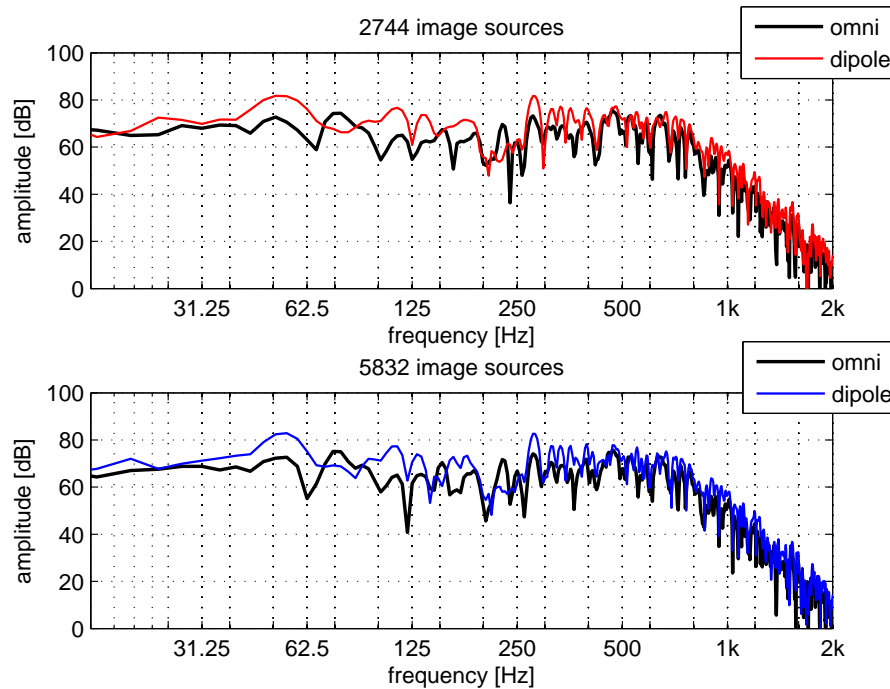


Figure 28: Fourier representation of the curves in Fig. 26.

4.2.2 Simulations With The RMM

The RMM on the other hand seems to be more dependent on the sum's truncation. At first, simulations with greater barrier frequencies were planned. The personal computer used for the simulations was not able to conduct compute transfer functions for more than 5000 room modes. This is partly due to its limitations but also in the programming itself. A maximal computation of 7000 room modes was possible using a more powerful computer and by storing the contents in a separate variable of a about 1GB.

The time domain signals feature a great waviness for higher barrier frequencies. This can be explained by the density of the room modes, which will increase for higher frequencies. The influence of the truncation in the modal domain is clearly visible in the time-domain representations. The bandwidth covered increases with the number of room modes considered but there is no clear benefit from the computations done with more room modes. A further analysis with a considerably increase of the barrier frequency is needed in order to fully understand the influence of the room modes. There is no great difference between the upper curves in Fig. 31 and the lower curves in Fig. 32 other than the frequency up to which the room modes are considered. Some of the notches vary but in an undefined manner and most likely because of the influence the room modes have on each other. The lower they are, the greater they are likely to have an influence given their greater magnitude and spectral distance from each other. The greatest differences are found between 1000 and 3000 modes. An increase of the barrier

frequency does not seem to have a great influence, at least not for this configuration.

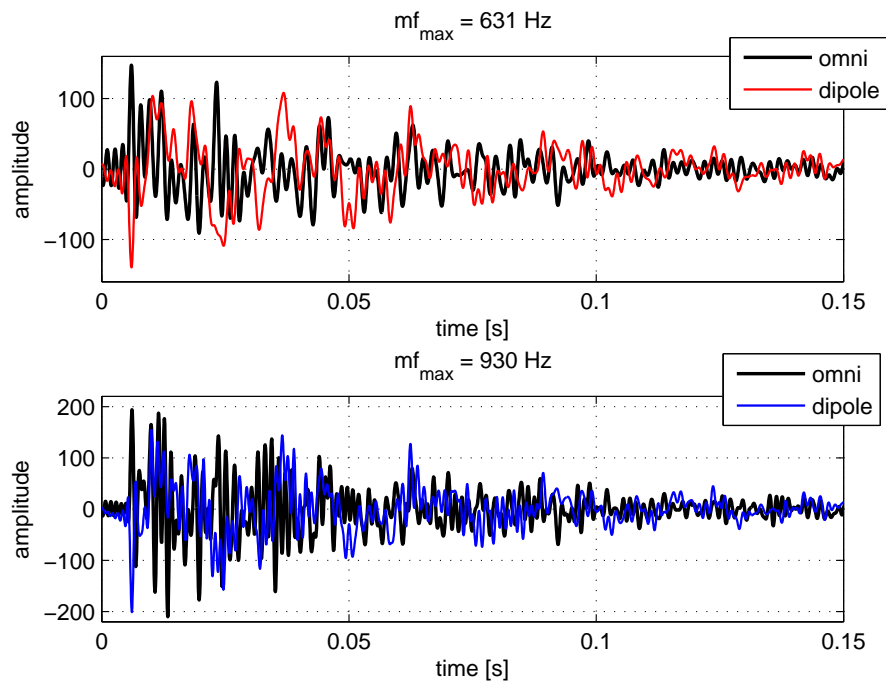


Figure 29: RIR computed with 1000 (above) and 3000 (bellow) modes.

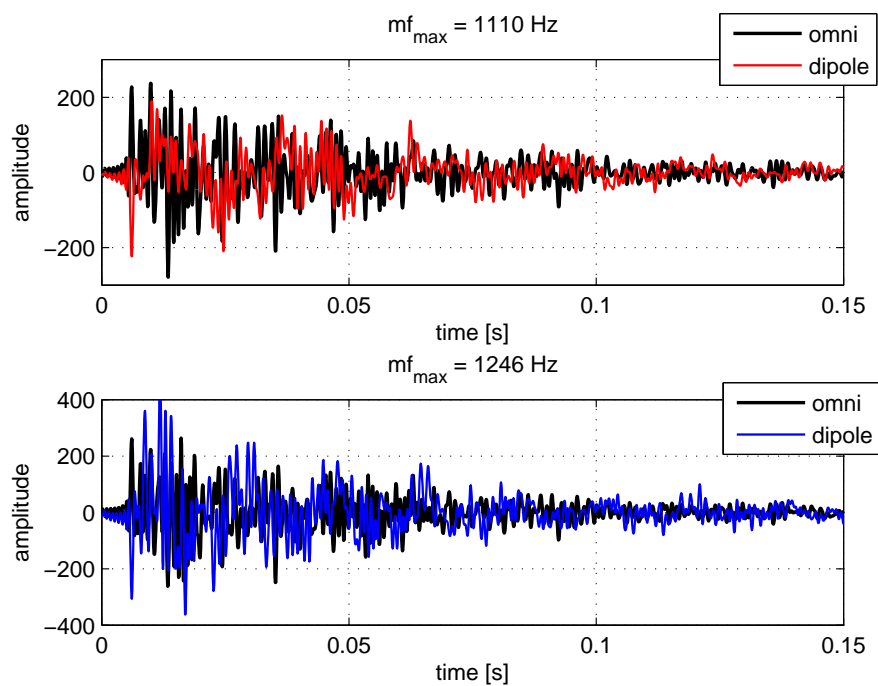


Figure 30: RIR computed with 5000 (above) and 7000 (bellow) modes.

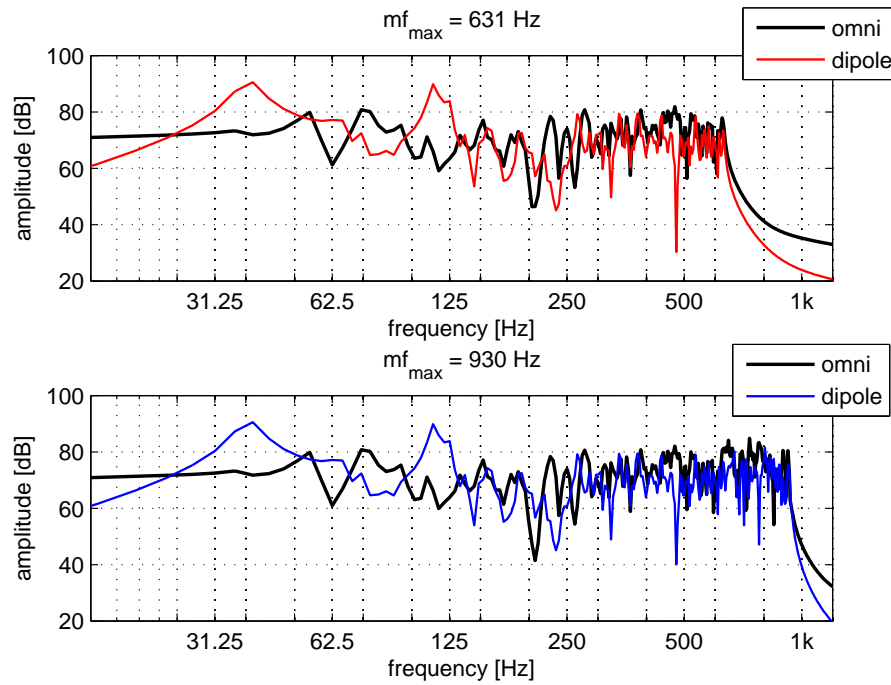


Figure 31: Fourier representation of the curves in Fig. 29.

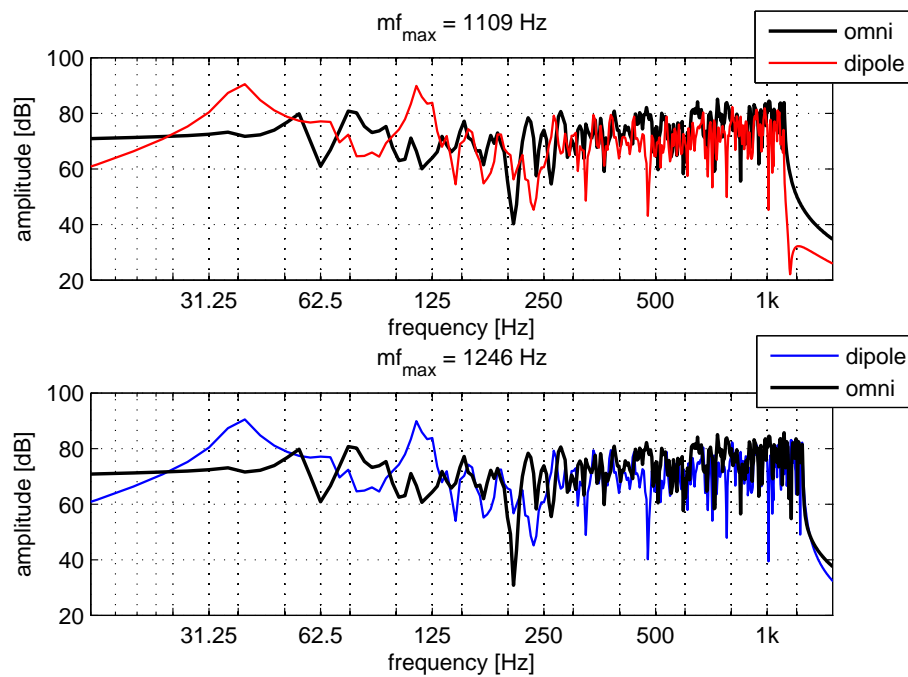


Figure 32: Fourier representation of the curves in Fig. 30.

4.2.3 Direct Comparison Between The RMM And The ISM

The direct comparison of both methods seems to provide more information concerning their accuracy. This section shows the previous results contrasting both methods. As expected, the accuracy of the ISM increases with the number of image sources. As seen in Fig. 34, it approximates the RMM with 7000 room modes pretty well and still remains a rather easy task for the computer. Also, it maintains its energy levels for more complex simulations as one can appreciate in the time domain signals.

In contrast, the RMM seems to produce the same results while keeping its frequency bandwidth limited. Also, the time domain signals become louder the more room modes are taken into consideration. This unwanted effect constitutes a drawback to this method as well as the fact that it represents a greater challenge for the computer. Concerning the direct sound one can say that both methods are able to model the direct sound with a certain accuracy. This is true for both the omni-directional case as well as for the simulations done with directivities. Both the spherical harmonics as well as the multipole characteristics seem to yield similar results for their 1st order directivities.

The filtering effects introduced in Section 3.1.3 are still noticeable, especially for the ISM, where the cut-off frequency is set at half the barrier frequency.

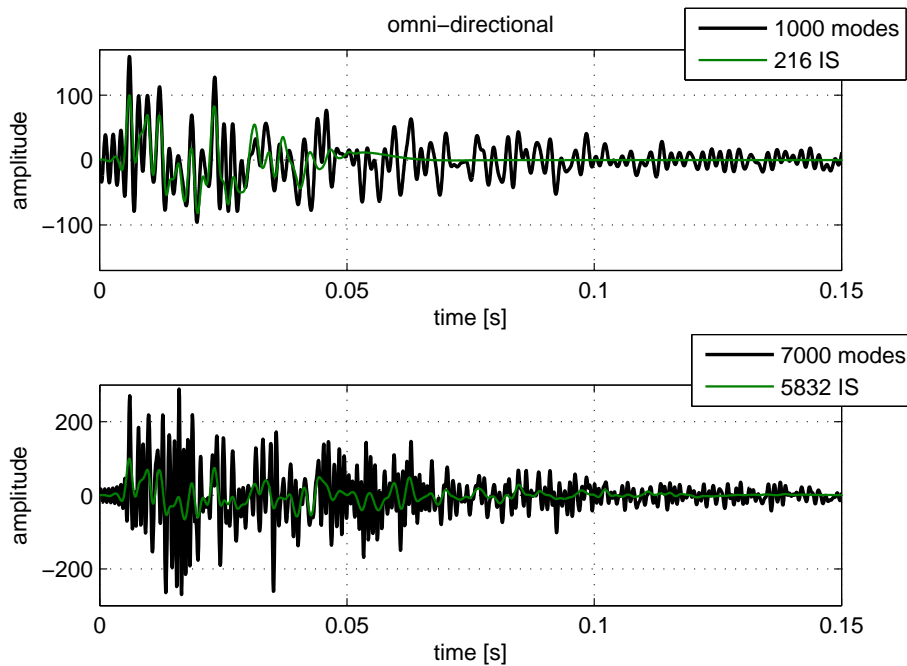


Figure 33: Omni-directional room impulse responses.

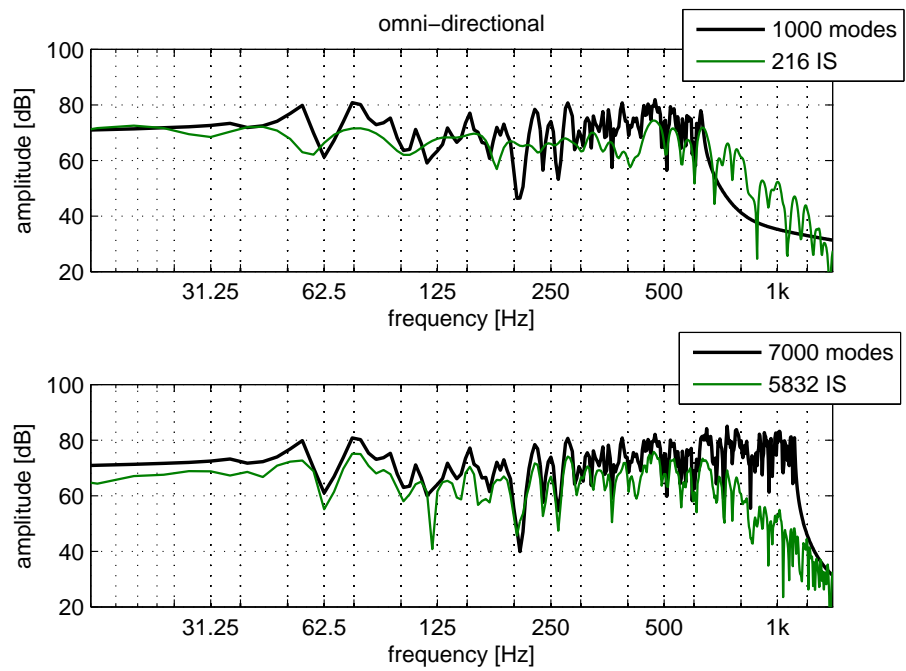


Figure 34: Fourier representation of the curves in Fig. 33.

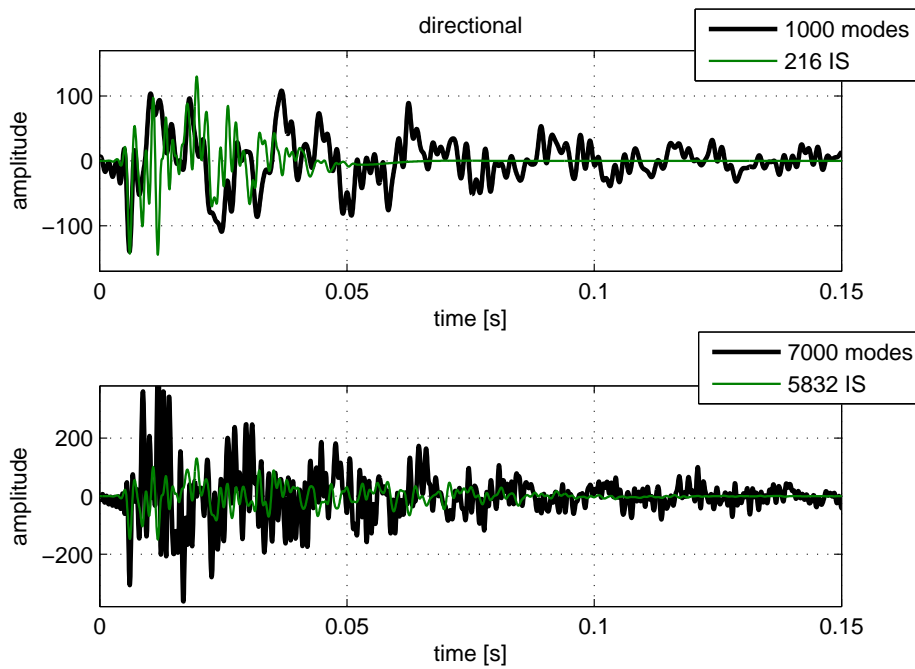


Figure 35: Directional room impulse responses.

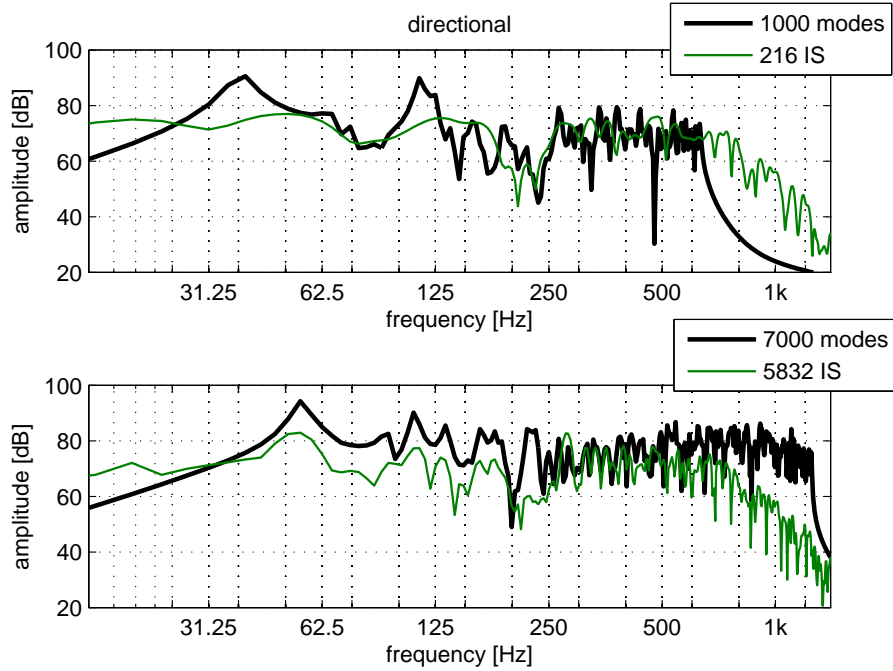


Figure 36: Fourier representation of the curves in Fig. 35.

4.3 Analysis Of The RIR In The SH-Domain

From Eq. 65 it becomes clear that directional room response can be analyzed at source and receiver position for every time instant t . The advantage of such a representation is that the room response can be analyzed in space with beam directions of finite-order. These beam directions $\boldsymbol{\theta}_{BR}$ and $\boldsymbol{\theta}_{BS}$ are described using the spherical harmonic functions of the orders (n, n') and degrees (m, m') as follows

$$\begin{aligned}\gamma_{n'm'}^{(R)} &= Y_{n'}^{m'}(\boldsymbol{\theta}_{BR}) \\ \gamma_{nm}^{(S)} &= Y_n^m(\boldsymbol{\theta}_{BS}).\end{aligned}\tag{88}$$

The directional room impulse response will be maximal if the chosen time t corresponds to an arrival time t_l and both beam directions $\boldsymbol{\theta}_{BR}$ and $\boldsymbol{\theta}_{BS}$ are equal to the l^{th} radiation incident angle $\boldsymbol{\theta}_{R_l}$ and to the receiving angle $\boldsymbol{\theta}_{S_l}$.

4.3.1 Energy Histogram

The idea behind the analysis of room transfer functions by means of an energy histogram consists in representing all squared contributions and reception of directional sound at the source and receiver positions, respectively. This is done by integrating the squared directional room response $h^2(\boldsymbol{\theta}_R, t, \boldsymbol{\theta}_S)$ over the spherical surface. The so-called energy histogram is defined for the receiver side

$$h^2(\boldsymbol{\theta}_R, t) = \int_{\mathbb{S}^2} h^2(\boldsymbol{\theta}_R, t, \boldsymbol{\theta}_S) d\boldsymbol{\theta}_S \quad \text{and from the source side as} \quad (89)$$

$$h^2(\boldsymbol{\theta}_S, t) = \int_{\mathbb{S}^2} h^2(\boldsymbol{\theta}_R, t, \boldsymbol{\theta}_S) d\boldsymbol{\theta}_R. \quad (90)$$

Eq. 89 describes all squared contributions of directional sound which are received at $\boldsymbol{\theta}_R$. On the other hand Eq. 90 indicates all contributions of directional sound being radiated at $\boldsymbol{\theta}_S$ and that will be picked up at the receiver position by a directional receiver.

The energy histograms are obtained with Eq. 88 and by exploiting the orthonormality property of the spherical harmonics $\int_{\mathbb{S}^2} Y_n^m(\boldsymbol{\theta}) Y_{n'}^{m'}(\boldsymbol{\theta}) d\boldsymbol{\theta} = \delta_{nn'}^{mm'}$ to

$$\begin{aligned} h^2(\boldsymbol{\theta}_R, t) &= Y_{n'}^{m'}(\boldsymbol{\theta}_R) \sum_{nm} h_{nm}^{n'm'}(t) h_{nm}^{n''m''}(t) Y_{n''}^{m''}(\boldsymbol{\theta}_R) \\ h^2(\boldsymbol{\theta}_S, t) &= Y_{n'}^{m'}(\boldsymbol{\theta}_S) \sum_{n''m''} h_{nm}^{n'm'}(t) h_{n''m''}^{n'm'}(t) Y_{n''}^{m''}(\boldsymbol{\theta}_S), \end{aligned} \quad (91)$$

where $\delta_{nn'}^{mm'}$ is a double *Kronecker* delta function³⁷. Eq. 91 can be written in a vectorized form as:

$$h^2(\boldsymbol{\theta}_R, t) = \mathbf{y}^T(\boldsymbol{\theta}_R) \mathbf{H}(t) \mathbf{H}(t)^T \mathbf{y}(\boldsymbol{\theta}_R) \quad (92)$$

$$h^2(\boldsymbol{\theta}_S, t) = \mathbf{y}^T(\boldsymbol{\theta}_S) \mathbf{H}(t)^T \mathbf{H}(t) \mathbf{y}(\boldsymbol{\theta}_S). \quad (93)$$

The whole derivation of the results obtained above can be found in Appendix B. Both equations can be understood to be the squared contributions of directional sound at from the source and receiver point of view.

37. Function named after the German mathematician Leopold Kronecker. It is defined as $\delta_{nn'}^{mm'} = \delta_{nn'} \cdot \delta_{mm'}$ and $\delta_{nn'} = \begin{cases} 0 & \text{if } n \neq n', \\ 1 & \text{if } n = n'. \end{cases}$

EH For The ISM

Illustrated in Table. 1 and Table. 2 are some of the early reflections as well as the direct path between the source and receiver position. The reflecting surface is painted with a pale blue color in the left column. The corresponding energy histograms can be found to the right, where the first one indicates the orientation of directional sound received at the time of energy contributions. Likewise, the histogram to the right indicates the energy quantity and its orientation from the source point of view. One can see the great accuracy given for the ISM, for which all of the reflections are clearly identified.

Here, the room impulse responses are illustrated without the filtering introduced in Section 3.1.3. This is the case in order to render possible an unaltered comparison with the RMM.

EH For The RMM

The RMM lacks accuracy in the time domain given the modal truncation of the sum. Thus a worse identification of the early reflections can be expected for low barrier frequencies such as $f_g \approx 1250\text{Hz}$. Illustrated in Table. 3 and Table. 4 are the same scenarios as before. This time the directional transfer functions obtained with the RMM have been converted with the **C**-matrix into their spherical harmonic representation. The same analysis introduced in Section 4.3.1 is hence possible.

Both methods can be compared now with respect to their spatial resolution for simulations with sources and receivers of arbitrary directivities. When analysing the results it becomes clear that a truncation in the frequency domain results in an aggravation of the spatial capacities of the RMM. The tendency is a mismatch concerning the accurate localization of the energy's orientation with respect to the source. The receiver side is not completely wrong, but is not as accurate as the energy histograms obtained with the ISM.

	Path	$h^2(\theta_R, t)$	$h^2(\theta_S, t)$
1			
2			
3			

Table 1: Energy histograms of the ISM.

	Path	$h^2(\theta_R, t)$	$h^2(\theta_S, t)$
4			
5			
6			

Table 2: Energy histograms of the ISM.

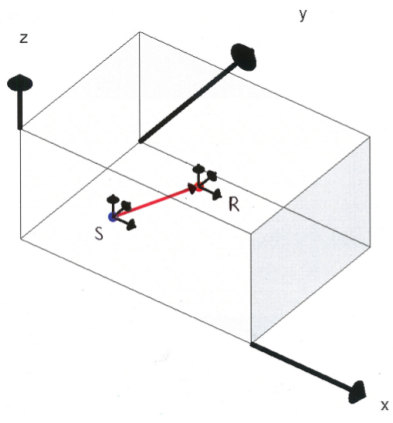
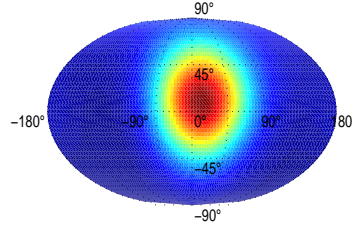
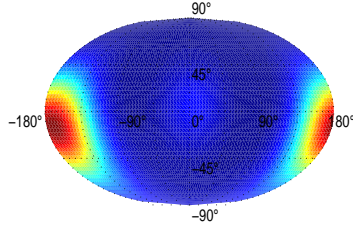
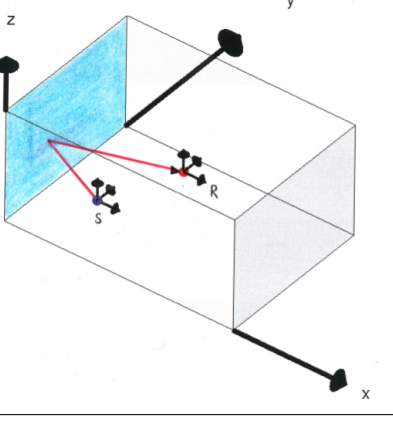
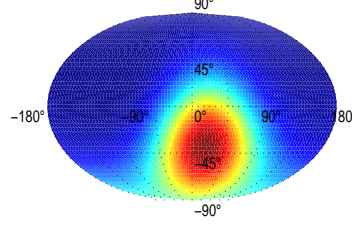
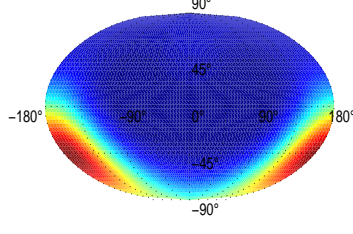
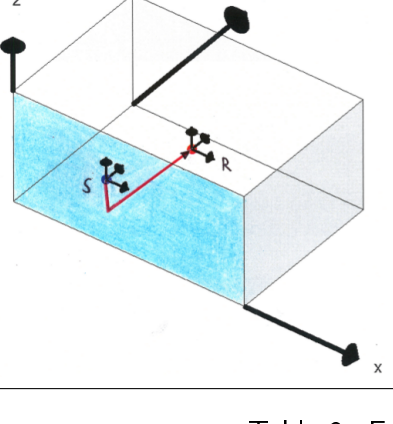
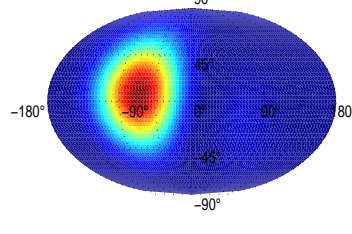
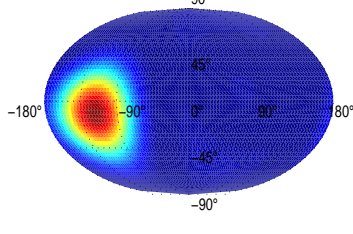
	Path	$h^2(\theta_R, t)$	$h^2(\theta_S, t)$
1			
2			
3			

Table 3: Energy histograms of the RMM.

	Path	$h^2(\theta_R, t)$	$h^2(\theta_S, t)$
4			
5			
6			

Table 4: Energy histograms of the RMM.

5 Resume And Outlook

Room impulse responses with and without directivities were simulated using both methods discussed throughout this work. No convergence problems were encountered for either method although important differences were found by means of their frequency and time domain representations. According to the results presented in Section 4, the ISM is able to produce a high accuracy concerning the early reflections of room impulse responses. This is also true for sources and receivers of arbitrary directivities. The accuracy with respect to the room resonances will increase as soon as the number of image sources becomes greater. Apparently it is enough to consider about 2000 image sources in order to match the frequency resolution of the RMM.

Problems with respect to the convergent nature of the method were not found. An increase of the number of image sources only implies an extension of the reverberation time. This last parameter depends again on the reflection coefficients themselves. The values that result from Section 4.1.2 correspond to a room with reverberant characteristics.

The simulation of room transfer functions with directivities on the basis of modes were done with the RMM. The results were also converted into the spherical harmonic domain, where the analysis and direct comparison of both methods' capacities is possible. The results of the simulations done in Section 4.2 reveal a limitation concerning the spatial resolution and simulation of the early reflections for low frequency barriers. The RMM lacks of resolution in the time domain as a result of this band limitation. Also, no clear amelioration comes from an extension of the frequency band and thus of the number of room modes considered. An increase of the barrier frequency represents a suppression of errors in the lower frequency band by $3dB$. A significant improvement is for this reason difficult to achieve.

At this point, little can be said regarding the number of room modes necessary in order to achieve a certain accuracy. The simulations were carried out with up to 7000 room modes, still achieving great results compared to the ISM. The choice of room resonances other than the natural sequence that arises from the room geometry is not a possibility. The balance between them given by their correlation, would be disrupted and thus the one governing the acoustic characteristics of the given situation. The question concerning the convergence behavior remains open and could be extended with far more complex simulations and studies.

References

- [AB78] J. B. Allen and D. A. Berkley, "Image method for efficiently simulating small-room acoustics," 1978.
- [ASV06] T. Ajdler, L. Sbaiz, and M. Vetterli, "Room impulse responses measurement using a moving microphone," *Journal of the Acoustical Society of America*, 2006.
- [AW05] G. Arfken and H. Weber, *Mathematical Methods for Physicists*, 6th ed. Elsevier Academic, 2005.
- [EWL05] J.-J. Embrechts, N. Werner, and S. Lesoinne, "Computation of directional impulse responses in rooms for better auralization," *Journal of the Acoustical Society of America*, 2005.
- [Goe06] T. Goerne, *Tontechnik*. Fachbuchverlag Leipzig, 2006.
- [Heu13] R. Heusdens, "Acoustical wave motion," Delft, NL, 2013.
- [JW03] R. E. Jensen and T. S. Welti, "The importance of reflections in a binaural room impulse response," *Journal of the Acoustical Society of America*, 2003.
- [KFCS00] L. E. Kinsler, A. R. Frey, A. B. Coppens, and J. V. Sanders, *Fundamentals of Acoustics*, 4th ed. John Wiley and Soncs, Inc., 2000.
- [Kut09] H. Kuttruff, *Fourier Acoustics*, 5th ed. Spon Press, 2009.
- [MBS⁺08] D. Murphy, M. Beeson, S. Shelley, A. Southern, and A. Moore, "Renderair - room acoustics simulation using a hybrid digital waveguide mesh approach," *Journal of the Acoustical Society of America*, 2008.
- [MF53] P. M. Morse and H. Feshbach, *Methods of Theoretical Physics*. McGraw Hill, 1953.
- [MZR12] H. Morgenstern, F. Zotter, and B. Rafaely, "Joint spherical beam forming for directional analysis of reflections in rooms," *Acoustics 2012 Hong Kong*, 2012.
- [Org97] I. S. Organization, "nr.3382, acoustics-measurement of the reverberation time in roomms with reference to other acoustical parameters," 1997.
- [PDV13] M. Pollow, P. Dietrich, and M. Vorländer, "Room impulse responses of rectangular rooms for sources and receivers of arbitrary directivity," 2013.
- [PSJ13] C. Pörschmann, S. Schmitter, and A. Jaritz, "Predictive auralization of room modifications by the adaptation of measured room impulse responses," 2013.
- [RTB98] D. A. Russel, J. P. Titlow, and Y.-J. Bemmen, "Acoustic monopoles, dipoles and quadrupoles: An experiment revisited," 1998.
- [SM07] R. Stewart and D. Murphy, "A hybrid artificial reverberation algorithm," *Journal of the Acoustical Society of America*, 2007.
- [Som92] A. Sommerfeld, "Die green'sche funktion der schwingungsgleichung," Leipzig, DE, 1892.

- [SSS11] A. Southern, S. Siltanen, and L. Savioja, "Spatial room impulse responses with a hybrid modelling method," *Journal of the Acoustical Society of America*, 2011.
- [TPKL13] S. Tervo, J. Pätynen, A. Kuusinen, and T. Lokki, "Spatial decomposition method for room impulse responses," *Journal of the Acoustical Society of America*, vol. 61, no. 1/2, 2013.
- [Wil99] E. G. Williams, *Fourier Acoustics*. Academic Press, 1999.
- [WW96] E. T. Whittaker and G. N. Watson, *A Course of Modern Analysis*, forth ed. Cambridge University Press, 1996.
- [Zot09a] F. Zotter, "Analysis and synthesis of sound-radiation with spherical arrays," PhD Thesis, University Music and Performing Arts, 2009.
- [Zot09b] —, "Sampling strategies for acoustic holografy/holophony on the sphere," *NAG-DAGA, Rotterdam*, 2009.
- [Zot14a] —, "Working with 5d point-to-point room impulse responses," 2014.
- [Zot14b] —, "Lecture notes to acoustic holography and holophony, vo, ws2014," Graz, AT, Issue 2014.

Appendix

A Green's Function Of A Point Source In Free Field

The whole idea behind Eq. 39 is to obtain the Green's function $G(\mathbf{r}, t)$ by means of integration. What is done really is an inverse Laplace and inverse Fourier transforms of $g(\mathbf{k}, s)$. The latter is obtained by Laplace and Fourier transforms of the general equation given by Eq. 10. The following two transform properties

$$\frac{d^n f(t)}{dt^n} \iff (s)^n \cdot F(s) - f(0) \quad \text{and} \quad (94)$$

$$\frac{\partial f(\mathbf{r})}{\partial x} \iff (ik_x) \cdot F(\mathbf{k}) \quad (95)$$

can be applied in Eq. 11 to $L = \frac{\partial^2}{\partial t^2} - c^2 \Delta$ resulting in

$$\begin{aligned} s^2 g(\mathbf{k}, s) - c^2 (i\kappa)^2 g(\mathbf{k}, s) &= 1 \\ g(\mathbf{k}, s) [s^2 + c^2 \kappa^2] &= 1 \\ g(\mathbf{k}, s) &= \frac{1}{s^2 + c^2 \kappa^2}, \end{aligned} \quad (96)$$

where $\kappa \equiv \|\mathbf{k}\| = \sqrt{k_x^2 + k_y^2 + k_z^2}$. The poles of the Green's function can be computed once $g(\mathbf{k}, s)$ has been made available in this form. By doing so an easier calculus of Eq. 39 becomes possible.

$$s^2 + c^2 \kappa^2 \stackrel{!}{=} 0 \iff s_{1,2} = \pm \sqrt{-c^2 \kappa^2} = \pm ic\kappa$$

The first part of the integral corresponds to the inverse Laplace transform and reads as follows

$$\frac{1}{2\pi i} \int_{-\infty}^{\infty} e^{st} g(\mathbf{k}, s) ds = \frac{1}{2\pi i} \int_{-\infty}^{\infty} \frac{e^{st}}{(s - ic\kappa)(s + ic\kappa)} ds. \quad (97)$$

Solving Eq. 97 becomes possible by using the *Residue Theorem*. The latter says that a function resisting the techniques of elementary calculus can be evaluated by expressing it as a limit of contour integrals. The theorem is put down in a mathematical way in Eq. 98

$$\oint_{\gamma} f(z) dz = 2\pi i \sum_{k=1}^n \text{Res} \{f(z), z_k\}, \quad (98)$$

with $f(z) = \frac{e^{zt}}{(z-ic\kappa)(z+ic\kappa)}$. The residues for both poles can now be computed.

$$\text{Res} \{f(z = ic\kappa)\} = \lim_{z \rightarrow ic\kappa} (z - ic\kappa) \cdot f(z) = \lim_{z \rightarrow ic\kappa} \frac{e^{zt}}{z + ic\kappa} = \frac{e^{ic\kappa t}}{2ic\kappa}$$

$$\text{Res} \{f(z = -ic\kappa)\} = \lim_{z \rightarrow -ic\kappa} (z + ic\kappa) \cdot f(z) = \lim_{z \rightarrow -ic\kappa} \frac{e^{zt}}{z - ic\kappa} = -\frac{e^{-ic\kappa t}}{2ic\kappa}$$

These results are inserted the line integral of $f(z)$ over the closed curve γ from Eq. 98 as follows

$$\begin{aligned} \oint_{\gamma} f(z) dz &= 2\pi i \left(\frac{e^{ic\kappa t}}{2ic\kappa} - \frac{e^{-ic\kappa t}}{2ic\kappa} \right) \\ &= \frac{2\pi i}{c\kappa} \sin(c\kappa t). \end{aligned}$$

The first part of the integral $g(\mathbf{k}, t)$ is solved with the last result and Eq. 97

$$\frac{1}{2\pi i} \oint_{\gamma} f(z) dz = \frac{\sin(c\kappa t)}{c\kappa}. \quad (99)$$

The next step is solving the inverse Fourier Transform with respect to the coordinate system. Interesting for the considerations made in this study is the three dimensional case. The result from the first part of the integral inserted in Eq. 39 yields

$$G(\mathbf{r}, t) = \frac{1}{(2\pi)^d} \int_{\mathbb{R}^d} e^{i\mathbf{k}^T \mathbf{r}} \frac{\sin(c\kappa t)}{c\kappa} d\mathbf{k}. \quad (100)$$

Applying the derterminant of the *Jacobian* matrix from Appendix B to Eq. 100 results in

$$G(\mathbf{r}, t) = \frac{1}{(2\pi)^3} \int_0^\pi \int_0^{2\pi} \int_0^\infty e^{i\mathbf{k}^T \mathbf{r}} \frac{\sin(c\kappa t)}{c\kappa} \kappa^2 d\kappa d\varphi \sin \vartheta d\vartheta. \quad (101)$$

The integral depending on the azimuth angle φ is solved here by chosing \mathbf{r} along the z-axis, thus $\mathbf{r}^T = [0, 0, r \cos \vartheta]^T$.

$$G(\mathbf{r}, t) = \frac{1}{(2\pi)^2 c} \int_0^\pi \int_0^\infty \kappa e^{i\kappa r \cos \vartheta} \sin(c\kappa t) d\kappa \sin \vartheta d\vartheta$$

Next the integral with respect to the zenith angle ϑ can be solved given the previous choice of \mathbf{r} . This angle can henceforth take only two values, i.e. 0 or π . This fact together with $z = \cos \vartheta$ and thus $\frac{dz}{d\vartheta} = -\sin \vartheta$ results in

$$\begin{aligned} G(\mathbf{r}, t) &= \frac{-1}{(2\pi)^2 c} \int_0^\infty \int_{-1}^1 \mathcal{K} e^{i\mathcal{K} \cdot \mathbf{r} \cdot \mathbf{z}} \sin(c\mathcal{K}t) dz d\mathcal{K} \\ &= \frac{-1}{(2\pi)^2 c} \int_0^\infty \left[\frac{\mathcal{K} e^{i\mathcal{K} \cdot \mathbf{r} \cdot \mathbf{z}}}{i\mathcal{K}r} \right]_1^{-1} \sin(c\mathcal{K}t) d\mathcal{K} \\ &= \frac{1}{(2\pi)^2 c} \int_0^\infty \left[\frac{e^{i\mathcal{K} \cdot \mathbf{r}} - e^{-i\mathcal{K} \cdot \mathbf{r}}}{ir} \right] \sin(c\mathcal{K}t) d\mathcal{K}. \end{aligned}$$

Using the Euler identity $\sin(a) = \frac{e^{ia} - e^{-ia}}{2i}$ in the last equation results in

$$G(\mathbf{r}, t) = \frac{1}{2\pi^2 cr} \int_0^\infty \sin(\mathcal{K}r) \sin(c\mathcal{K}t) d\mathcal{K},$$

and with the trigonometric relationship $\sin(\alpha) \sin(\beta) = \frac{\cos(\alpha-\beta) - \cos(\alpha+\beta)}{2}$ it is possible to write

$$\begin{aligned} G(\mathbf{r}, t) &= \frac{1}{4\pi^2 cr} \int_0^\infty \left[\cos(\mathcal{K}(r-ct)) - \cos(\mathcal{K}(r+ct)) \right] d\mathcal{K} \\ &= \frac{1}{4\pi^2 cr} \pi \left[\delta(r-ct) - \delta(r+ct) \right]. \end{aligned}$$

The next relation is the regularized solution of the integral in form of a distribution. It reads as $\int_0^\infty \cos(\mathcal{K}\gamma) d\mathcal{K} = \pi \delta(\gamma)$. The previous result for the Green's function can be simplified by its causality property³⁸ and since this solution is valid for $r > 0$ only, the second term can be omitted. The solution for the Green's function of a point source in free-field reads as follows

$$G(\mathbf{r}, t) = \frac{1}{4\pi cr} \delta(r-ct). \quad (102)$$

38. Causality states that $G(\mathbf{r}, t) \stackrel{!}{=} 0$ for all $t < 0$.

B Jacobian Matrix

The Cartesian coordinate system is directly related to the Spherical coordinate system via Eqs. 103

$$\begin{aligned}x &= r \sin \vartheta \cos \varphi, \\y &= r \sin \vartheta \sin \varphi \quad \text{and} \\z &= r \cos \vartheta.\end{aligned}\tag{103}$$

Thereby denotes φ the azimuth and ϑ the zenith angle. The Jacobian matrix $J_F(r, \varphi, \vartheta)$ of a function F defined in \mathbb{R}^3 is given by

$$\begin{aligned}J_F(r, \varphi, \vartheta) &= \begin{bmatrix} \frac{\partial x}{\partial r} & \frac{\partial x}{\partial \vartheta} & \frac{\partial x}{\partial \varphi} \\ \frac{\partial y}{\partial r} & \frac{\partial y}{\partial \vartheta} & \frac{\partial y}{\partial \varphi} \\ \frac{\partial z}{\partial r} & \frac{\partial z}{\partial \vartheta} & \frac{\partial z}{\partial \varphi} \end{bmatrix} \\ &= \begin{bmatrix} \sin \vartheta \cos \varphi & r \cos \vartheta \cos \varphi & -r \sin \vartheta \sin \varphi \\ \sin \vartheta \sin \varphi & r \cos \vartheta \sin \varphi & r \sin \vartheta \cos \varphi \\ \cos \vartheta & -r \sin \vartheta & 0 \end{bmatrix}.\end{aligned}\tag{104}$$

Its determinant as used in Eq. 101 is computed as follows

$$\begin{aligned}\det|J_F(r, \varphi, \vartheta)| &= r^2 \cos^2 \vartheta \cos^2 \varphi \sin \vartheta + r^2 \sin^3 \vartheta \sin^2 \varphi \\ &\quad - (-r^2 \sin \vartheta \cos^2 \vartheta \sin^2 \varphi - r^2 \sin^3 \vartheta \cos^2 \varphi) \\ &= r^2 \sin^3 \vartheta (\sin^2 \varphi + \cos^2 \varphi) + r^2 \cos^2 \vartheta \sin \vartheta (\cos^2 \varphi + \sin^2 \varphi) \\ &= r^2 \sin \vartheta (\sin^2 \vartheta + \cos^2 \vartheta) \\ &= r^2 \sin \vartheta.\end{aligned}\tag{105}$$

The volume element in 3-D space is an expression of the form

$$dV = dx dy dz,\tag{106}$$

and in its spherical form

$$\begin{aligned}dV &= \det|J_F(r, \varphi, \vartheta)| dr d\vartheta d\varphi \\ &= r^2 \sin \vartheta dr d\vartheta d\varphi.\end{aligned}\tag{107}$$

C Energy Histogram

The notation in a vectorized form of $h(\boldsymbol{\theta}_R, t, \boldsymbol{\theta}_S) = \boldsymbol{\gamma}_R^T \mathbf{H}(t) \boldsymbol{\gamma}_S$ remains as presented in Section 3.4.2 the same. The squared contribution of directional sound being radiated by a directional source and measured by a directional receiver are obtained at the receiver position by means of integration as follows:

$$\begin{aligned} h^2(\boldsymbol{\theta}_R, t) &= \int_{\mathbb{S}^2} h^2(\boldsymbol{\theta}_R, t, \boldsymbol{\theta}_S) \, d\boldsymbol{\theta}_S \\ &= \int_{\mathbb{S}^2} \boldsymbol{\gamma}_R^T \mathbf{H}(t) \boldsymbol{\gamma}_S \cdot \boldsymbol{\gamma}_S^T \mathbf{H}(t)^T \boldsymbol{\gamma}_R \, d\boldsymbol{\theta}_S \\ &= \boldsymbol{\gamma}_R^T \mathbf{H}(t) \int_{\mathbb{S}^2} \boldsymbol{\gamma}_S \boldsymbol{\gamma}_S^T \, d\boldsymbol{\theta}_S \mathbf{H}(t)^T \boldsymbol{\gamma}_R. \end{aligned}$$

The last integral is solved with the choice of spherical harmonics for the computation of the room impulse response with directivities. This is written in a vectorized form as $\boldsymbol{\gamma} = \mathbf{y}$ and by making use of the orthonormality property of the spherical harmonics it yields

$$\begin{aligned} h^2(\boldsymbol{\theta}_R, t) &= \mathbf{y}_R^T \mathbf{H}(t) \int_{\mathbb{S}^2} \mathbf{y}_S \mathbf{y}_S^T \, d\boldsymbol{\theta}_S \mathbf{H}(t)^T \mathbf{y}_R \\ &= \mathbf{y}_R^T \mathbf{H}(t) \mathbf{H}(t)^T \mathbf{y}_R. \end{aligned} \tag{108}$$

In the same manner, the contribution of directional sound at the source position is calculated:

$$\begin{aligned} h^2(\boldsymbol{\theta}_S, t) &= \int_{\mathbb{S}^2} h^2(\boldsymbol{\theta}_R, t, \boldsymbol{\theta}_S) \, d\boldsymbol{\theta}_R \\ &= \int_{\mathbb{S}^2} \boldsymbol{\gamma}_R^T \mathbf{H}(t) \boldsymbol{\gamma}_S \cdot \boldsymbol{\gamma}_S^T \mathbf{H}(t)^T \boldsymbol{\gamma}_R \, d\boldsymbol{\theta}_R \\ &= \mathbf{y}_S^T \mathbf{H}(t)^T \int_{\mathbb{S}^2} \mathbf{y}_R \mathbf{y}_R^T \, d\boldsymbol{\theta}_R \mathbf{H}(t) \mathbf{y}_S \\ &= \mathbf{y}_S^T \mathbf{H}(t)^T \mathbf{H}(t) \mathbf{y}_S. \end{aligned}$$

The last result constitutes one of the tools used for analyzing the reflection paths of the ISM as used in Section 4.3.1.